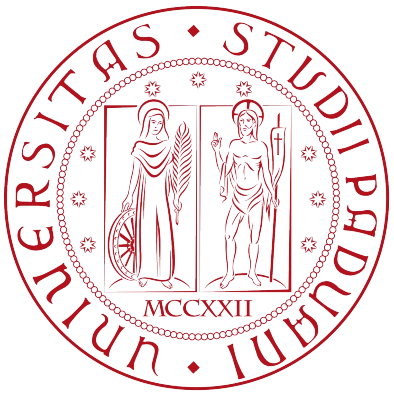

UNIVERSITÀ DEGLI STUDI DI PADOVA

Dipartimento di Fisica e Astronomia "Galileo Galilei"

Master Degree in Astrophysics and Cosmology

Final Dissertation

THE FORMATION OF MEGA HALOS IN NUMERICAL SIMULATIONS

Thesis supervisor

Prof. Enrico Maria Corsini

Thesis co-supervisor

Prof. Franco Vazza

Candidate

Luca Beduzzi

Academic Year 2022/2023

Contents

Abstract

Galaxy cluster are the largest virialised structure in the Universe. The medium that fills the space between galaxies in the cluster has been observed both in X-ray and radio bands, meaning that we can observe both thermal and non-thermal processes. The non thermal processes are mostly dominated by inverse Compton scattering and synchrotron emission. The latter is particularly well observed as it produces halos that extent for not more than ~ 1 Mpc, in diameter, detected in the majority of massive clusters with ongoing merging activity. In the recent work of Cuciti et al. (2022), the discovery of a new family of halos was reported: the mega radio halos (MHs) that can fill a volume 30 times larger than the classical radio halo regions known so far. This emission is thought to be generated from relativistic electrons through Fermi II turbulent re-acceleration processes. In this Thesis, I present the results of the first dedicated analysis of this process with new cosmological simulations, as a way of testing the turbulent re-acceleration scenario for mega radio halos.

I analyse the data acquired from a cosmological, adaptive mesh refinement, *ENZO* simulation (Bryan et al. 2014) where the gas evolution has been studied with Crater (Wittor et al. 2016), a Lagrangian code that evolve gas tracers injected, in post-process, in the simulation. The final cluster of galaxies has a mass of $M_{100} = 3.8 \cdot 10^{14}$ $M_{\odot}$ and a virial radius of $R_{100} = 1.52$ Mpc at $z = 0$. This is a low mass cluster and it undergoes a few mergers during its evolution. This system allowed me to test the possible formation scenario of mega radio halos in a typical clusters of galaxies.

After a spatial evolution examination, I find that the electrons which end up in the MH region have spent a part of their evolution in the center of the cluster and shared similar physical conditions of the gas that finally fills the volume of classical radio halos. I measure that continuous accretions of massive satellites re-ignites the turbulent process maintaining the electrons at very high energy. A conspicuous fraction of the cosmic rays has been re-accelerated to reach a large enough energy to be radio emitting for synchrotron radiation. Moreover, the shape of the radial distribution of the fraction of radio emitting electrons seems to reproduce the one retrieved from the observations, indicating a plateau, in the last half Gyr of the simulation, for the whole MH region. Very interestingly, my analysis shows that the median values for the energy of populations of electrons injected at energies of GeV can be maintained at this level by the prolonged effect of turbulent re-acceleration, for over ~ 5 Gyr, i.e. much beyond the classical view in which turbulent re-acceleration in the ICM can only act intermittently, and boost the energy of radio emitting electrons for less than ~ 1 Gyr.

Although preliminary and limited to a single simulation for the moment, these results are promising and have been presented in a letter to Astronomy & Astrophysics (Beduzzi et al., 2023, arXiv:2306.03764).

Chapter 1

Galaxy clusters and non-thermal radiation

In this chapter I will briefly introduce the history of the observations of the galaxy clusters and on their role in the development of the modern theoretical picture of the cosmological model. The introduction will also provide a description of the observational properties, ranging from X-rays, optical and radio wavelength. Finally it will be given an overview of the latest discoveries that motivates my thesis work.

1.1 Introduction

Galaxy clusters are the most massive virialized structures in the Universe, and they are still accreting matter from the cosmic web in the present epoch. They are the perfect crossroad between astrophysics and cosmology, providing the opportunity to test models of galaxy formation and evolution, the dynamics of the intra-cluster medium (ICM), and plasma physics in very large systems, as well as dark matter and the cosmological model. Galaxy clusters were the first cosmic objects where the dynamical determination of gravitational mass allowed astrophysicists to infer the presence of dark matter on Mpc scales. The works by Zwicky (1933) and Smith (1936) highlighted that the number of stars present in those clusters was unable to explain the mass necessary to account for the observed velocity dispersion. Zwicky referred to the missing matter as dark matter (DM), introducing the term for the first time. Subsequent studies revealed that the issue was caused by a miscalculation of the number of stars, but the problem of the missing matter from the observations still holds true today.
During the seventies, the discovery of X-ray emission from the extended sources allowed to determine a significant portion of the missing matter, providing also evidence for the existence of a diffuse plasma filling the space between the systems of virialised galaxies, namely the ICM (Cavaliere et al. 1971; Meekins et al. 1971; Forman et al. 1972). Its presence, along with the measurements of its velocity dispersion, add further proof to the lack of matter. Additionally, the presence of the ICM explained variation of the spectrum of Cosmic Microwave Background (CMB) photons due to scattering process, via Inverse Compoton (IC). This effect is better known as the Sunyaev-Zel'dovich effect (SZE, Sunyaev & Zeldovich, 1970, 1972a, 1980). Clusters of galaxies provided evidence for the gravitational collapse of matter from small fluctuation of density, produced in the early phases of the Universe. Relatively simple analytical models were able to well

explain the X-ray emission of the Coma cluster and of similar objects (van Albada 1960; van Albada 1961; Peebles 1970; Gott & Gunn 1971; Sunyaev & Zeldovich 1972b; White 1976). Furthermore, subsequent studies (Press & Schechter, 1974; Gott & Rees, 1975; White & Rees, 1978) highlighted the hierarchical nature of cluster formation, which was then associated with the first models of cold dark matter (CDM) cosmological scenario. Nowadays is widely believed that clusters are formed by hierarchical structure formation processes. In this scenario, smaller units (galaxies, groups and small clusters) formed first and merged under gravitational pull to larger and larger units in the course of time. Mergers between clusters are the main mechanism by which several clusters of galaxies are formed, while a continuous accretion of "smooth" gas and DM components, or accretion by smaller sub-units, is always present. The history and the studies of such structures have played a crucial role in testing and validating cosmological models making them the most reliable test bench for simulations and to proof the validity of cosmological scenarios (Allen et al., 2011).

The astrophysical processes relevant for galaxy clusters span from cosmology to astrophysics particles, covering a multitude of topics. In the first part of this work, I will investigate the different kind of emissions associated with clusters of galaxies, starting from the study of the bremsstrahlung processes in order to understand the structure of the thermal plasma within the cluster. Moreover, I will explore the most elusive processes of the non-thermal component of the relativistic electrons that populate the ICM, filling the virial radius of the clusters and the structures beyond such as the radio relic. Then, I will focus on the re-acceleration mechanisms that allow radio emitting electrons to reach energies of a few giga electronvolts, and on the different emission processes in which they are involved, such as IC and synchrotron.

1.2 Galaxy cluster formation model

I will briefly introduce the formation scenario of galaxy clusters before discussing their observational and physical properties. The formation scenario of clusters of galaxies follows the hierarchical formation model scenario, where the most most massive objects form via gravitational collapse of small fluctuation of the primordial density field, which has a non-homogeneous characterisation. The existence of such density perturbations can be inferred from the temperature fluctuation of the cosmic microwave background (CMB) as firstly observed with the Cosmic Background Explorer (COBE) mission (Bennett et al., 1996). The non-homogeneity is described through the density contrast field, or overdensity, given by: $\delta = (\rho - \bar{\rho}_{\rm m})/\bar{\rho}_{\rm m}$, where $\bar{\rho}_{\rm m}$ is the mean mass density of the Universe. Once the gravitational collapse has begun, matter accumulates and its mass increases via hierarchical sequence of accretion. The growth regime can vary as function of the overdensity field, if the value is $\delta \ll 1$ the growth can be described through linear approximations. However, when $\delta \gg 1$ the growth regime is non-linear and its description generally requires approximated methods, or direct numerical simulations.

Numerical N-body simulations make it possible the study and the evolution of the clusters and their formation processes. By providing realistic initial conditions for the pattern of linear density fluctuations derived from the CMB, it is possible to accurately track the growth of structures in the fully non-linear regime. These simulations can also be combined with other relevant astrophysical processes, such as galaxy formation and radiative processes, to obtain a comprehensive understanding of cluster evolution.

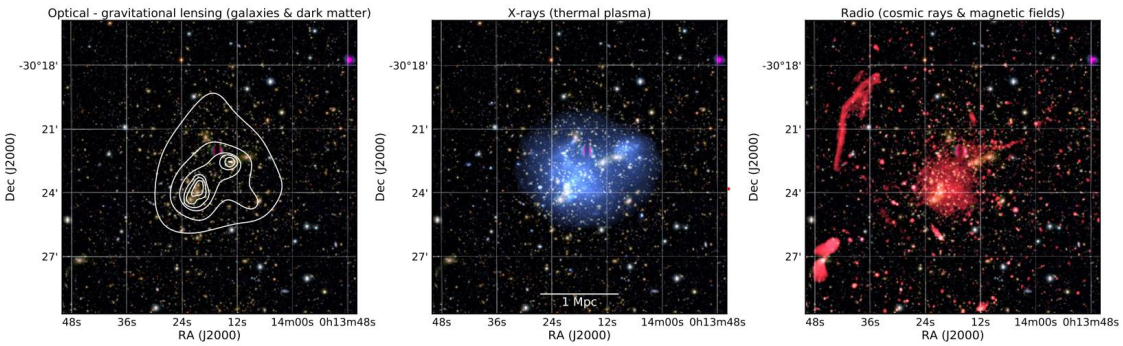

Figure 1.1: The galaxy cluster Abell 2744 in three different optical bands. *Left panel*: Optical (Subaru BRz; Medezinski et al., 2016) view of the cluster. White linearly spaced contours represent the mass surface density derived from a weak lensing study from Merten et al. (2011) and Lotz et al. (2017). *Central panel*: X-ray emission from the thermal ICM plasma (Chandra 0.5–2.0 keV band). *Right panel*: 1–4 GHz Very Large Array (VLA), tracing cosmic rays and magnetic fields. Credits: van Weeren et al. (2019), but see also Pearce et al. (2017) for more details.

1.3 Galaxy clusters observational properties

Galaxy clusters observations span the whole range of the spectrum, from the X-ray band to radio frequencies (Figure 1.1). In the most energetic part of the spectrum, the presence of very hot medium, the ICM, can be detected. It is composed of plasma that can reach a temperature of 10^8 K. The line and continuum emission visible in the X-ray comes from bremsstrahlung. Also, IC processes of CMB photons involving high energy electrons can produce emission in the hard X. In the visible band we observe the emission coming from the galaxies, dominated by the stars light, diffuse dust, and HII regions emission. The bluer part of the visible spectrum is produced mostly from late-type galaxies. These galaxies are typically located in the outer region of the clusters and their emissions are dominated by younger stellar populations. On the other hand, the reddest part of the spectrum is dominated by old elliptical galaxies that have already depleted a significant portion of their hydrogen content, making the formation of young and massive stars more challenging. In the microwaves, one can expect to observe the CMB radiation passing through the cluster. Instead, the observed will see a decrease in the background intensity, which is caused by the interaction of CMB photons with the free electrons of the ICM. This is observed as a spectrum shift toward higher frequencies in all the regions of the cluster within the virial radius, which I will define later. The radio emission comes from non-thermal processes, specifically the synchrotron mechanism resulting from the presence of magnetic field diffused in plasma. The radiation can be observed with both with low or high polarisation. In the inner region, also known as radio halo, the light exhibits low polarisation due to the morphology of the magnetic field which does not show preferential spatial orientation. On the other hand, highly polarised sources are usually associated with radio relics, which are observed in the outskirt. Finally, approximately the 80% of the cluster mass is in form of DM, which cannot be directly observed. However, its presence can be inferred through the weak gravitation lensing effect or by measuring the velocity dispersion of the baryonic matter within the cluster using the virial theorem.

1.3.1 X-ray observations

Extended X-ray emission from clusters of galaxies was attributed to bremsstrahlung processes by Felten et al. (1966) and, after a spurious X-ray detection of the Coma cluster, it was observed after few years (Cavaliere et al. 1971; Forman et al. 1972; Kellogg et al. 1972). Plasma contributes $\sim 80-90\%$ of the baryonic matter in clusters, and its temperature can range from $\sim 10^7$ to 10^8 K. As result, it can be observed in the X ray and it is assumed to represent the broadest part of the thermal emission. The plasma is not associated with the single galaxies within the cluster but correlations can be observed between the two components. This correlations arises because both the components are in approximate (thermo)dynamical equilibrium with the cluster potential well. The first X ray observations during the seventies revealed that the ICM in the centers of many clusters was dense enough to cool down in time lower then the Hubble time (see Hudson et al. 2010 for a complete review), via bremsstrahlung processes. These observations contribute to develop the cooling flow (CF) model. According to this model, the ICM at the centers of the clusters with dense cores hydrostatically cools through radiation emission. As result, the cool gas is compressed by the weight of the overlying gas and hot gas from the outer regions of the ICM flows in to replace the compressed one, generating a CF. The early X-ray observations seemed to validate this model and provided some evidence of expected Hα and UV emission. However, optical observations failed to detect the expected star formation rates, as well as CO and molecular gas. The expected star formation rate should have been of hundred of $M_\odot$ s^{-1}, while observations exhibit a wide range, from some $M_\odot$ s^{-1} to one per thousand (McNamara & O'Connell, 1989; O'Connell & McNamara, 1989). This discrepancy was attributed to the lack of heating mechanism in the model, such as active galactic nuclei (AGN) heating via direct cosmic ray-ICM interaction and conduction, or through shockwaves and turbulence. The failure of the classical CF model has changed the nomenclature and the improvement of the thermodynamical classification of such systems, based on their observed X-ray properties. Nowadays, X-ray emitting clusters of galaxies can be classified into cool-core (CC) clusters and non-cool core clusters (NCC), depending on the presence of a dense X-ray emission core (Molendi & Pizzolato, 2001). In the central region of CC, we can observe a strong X-ray emission that remarks the presence of ionisation and gas cooling. The presence of a CC is reflected in the temperature profiles, which exhibit a decrease in temperature with decreasing radius in the innermost region of CC clusters, down to a minimum temperature of ~ 0.1 keV.
The ICM temperature is consistent with the galaxy velocity dispersion, indicating that both are in equilibrium with the same potential well. The abundance of elements in the intracluster plasma is cosmological, meaning that it follows from the abundances of elements produced by cosmic baryogeneis, with the additional presence of heavier by-products of star formation. The fraction of metals observed in the ICM is smaller than the solar abundance, close to 1/3 or 1/2 of the solar abundances (Werner et al., 2008). The radial distribution of metallicity exhibits a peak in the central region of the CC, whereas in NCC, it shows a flat distribution in the central region (see Vikhlinin et al., 2006; Pratt et al., 2007; Leccardi & Molendi, 2008).

A large number of properties can be inferred through empirical relations. These relationships can provide valuable information for describing theoretical models and constrain fundamental properties of galaxy clusters. One strong correlation is observed between the mass of the X-ray emitting gas, within R_{500}, and the stellar mass within the same radius.

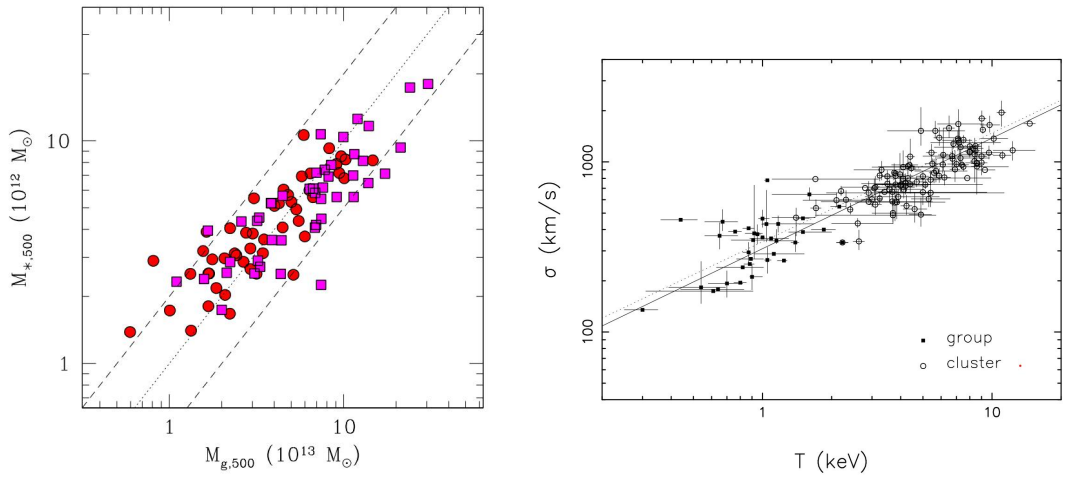

Figure 1.2: *Left panel*: Mass in stars vs. mass of hot, X-ray emitting gas. Both masses are measured within R_{500}. Red circles show local clusters ($z < 0.1$), while magenta squares show higher-redshift clusters ($0.1 < z < 0.6$). Credit: Kravtsov & Borgani (2012). *Right panel*: σ vs. temperature relation between the emitting gas velocity dispersion and its temperature for galaxy clusters (circles) and galaxy groups (square). The dotted and solid lines show the best power-law fits for groups and clusters, respectively. Credit: Voit (2005).

R_{500} represents the virial radius that contain 500 times the critical density, $\rho_{\rm crit}$, of the Universe. The density $\rho_{\rm crit}$ is defined as $\rho_{\rm crit}(z) = 3H(z)^2/8\pi G$ where $H(z)$ is the Hubble parameter as a function of redshift. The relationship, between gas and stellar mass, can be seen in Figure 1.2, where it can be noticed that the gas mass in clusters is about, on average, ten times larger than the mass in stars. The result presented in this paper was fundamental to confirm the self-similar model of clusters, which implies that different clusteres exhibit the same properties at a certain characteristic radius.
A strong correlation also exists between the bolometric luminosity of the thermal components of the ICM, within R_{500}, and the product between the mass of the gas within R_{500} and the ICM temperature derived from the X-ray spectra computed between $0.15R_{500} - R_{500}$ (Figure 1.3, V. et al. (2006)), called "pseudo-pressure".
As one can expect, the X-ray luminosity of clusters well correlate with their velocity dispersion (Figure 1.2). This scaling relation can be very useful to infer the mass of clusters too distant to have a reliable estimate of the velocity dispersion of galaxies, but for which integrated X-ray observables can be obtained.

1.3.2 Optical observations

Optical discoveries of clusters culminate with the large catalog of clusters by George Abell and collaborators (Abell, 1958; Abell et al., 1989). Abell's catalog includes most of the known nearby galaxy clusters, and it represents the foundation for much of our modern understanding of these objects. Given the intricate nature of cluster cataloging from galaxy surveys, which is influenced by the inclination of galaxies along the line of sight, Abell adopted a method of constructing his catalog by counting the number of galaxies present in each cluster. Specifically, he considered galaxies within two magnitudes

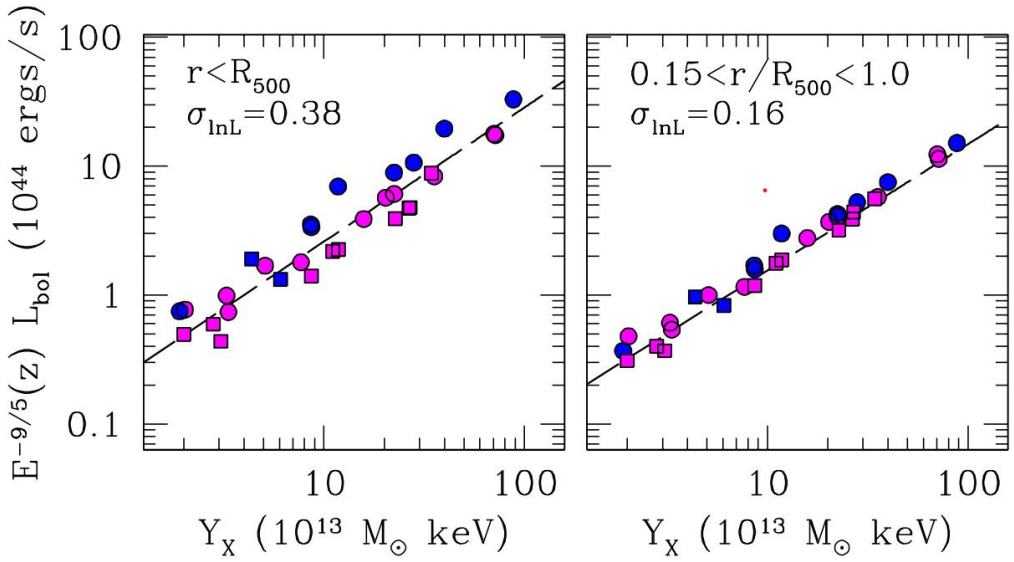

Figure 1.3: Correlation of bolometric luminosity of intracluster gas and $Y_X \equiv M_{gas} Y_X$, where M_{gas} is the mass of the gas within R_{500} and Y_X is temperature derived from the fit to gas spectrum accounting only for emission from radial range $0.15R_{500} - R_{500}$. Results are shown for the local clusters from the Representative XMM–Newton Cluster Structure Survey sample of Pratt et al. (2009). *Left panel*: total luminosity integrated within radius R_{500}. *Right panel*: it shows the bolometric luminosity calculated with the central $0.15R_{500}$ of the cluster. Labels in the top left corner of both diagrams indicate the radial range used in computing the luminosity and logarithmic scatter of luminosity at fixed Y_X. The blue points show CCs, while magenta points are NCC. Clusters classified as relaxed and disturbed are shown by circles and squares, respectively. Note that exclusion of the cluster cores reduces the scatter between luminosity and Y_X by more than a factor of two. Credit: Kravtsov & Borgani (2012).

of the tenth brightest galaxy in the cluster. Moreover, Abell defined a fixed bounding radius of ∼2 Mpc for all clusters. Additionally, to compensate for projection effects, he subtracted a background level from his galaxy counts. Abell introduced a classification based on the "richness" of the cluster, which correspond to the number of galaxies within them. Clusters with more than 30 and less than 50 galaxies are classified as Class 0, while those with more than 300 galaxies are Class 5.

A key feature of galaxy clusters is their ability to act as powerful cosmic magnification lenses, producing a variety of detectable lensing effects, from strong to weak lensing (Kneib & Natarajan, 2011). The phenomenon of gravitational lensing (albeit from the sun) which was first observed in 1919 (Eddington, 1919) during a solar eclipse, demonstrate that the gravitational mass can induce a curvature in spacetime able to bend the path of light rays. The propagation of light from a distant source to an observer is influenced by, besides the gravitational field of local inhomogeneities, the global geometry of the Universe (Schneider et al., 1992). Gravitational lensing observations provides a means to study the mass distribution of massive objects, dominated by DM. In this case, the presence of massive DM component can be detected through the deflection, shearing or magnification of the background sources. Weak lensing, characterised by small deformation of the background

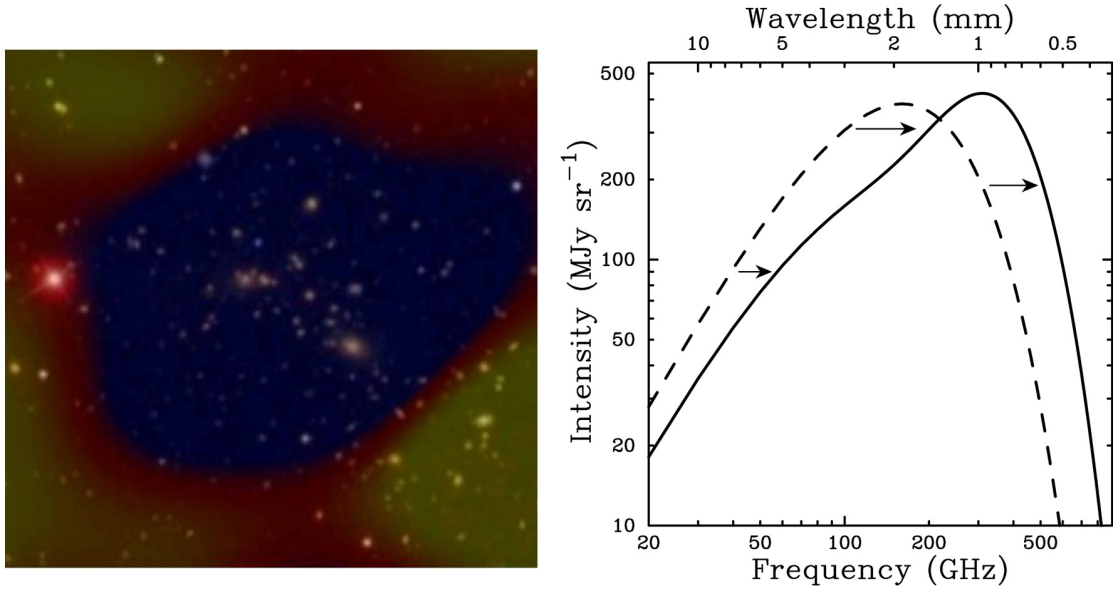

Figure 1.4: *Upper panel*: composite image of Abell 1914 in optical and microwave bands. It is visible the effect of scattering that makes the cluster looking colder than the background. Credit: Borgani & Kravtsov (2011). *Lower panel*: CMB spectrum undistorted (dashed line) and distorted (solid line). In order to clearly show the effect, the SZE distortion shown is for a fictional cluster 1000 times more massive than a typical massive galaxy cluster. The SZE causes a decrease in the CMB intensity at frequencies < 218 GHz and an increase at higher frequencies. Credit: Carlstrom et al. (2002).

objects, is the responsible for all this effects. Other two lensing effect exists, namely strong and micro lensing, the former produces the Einstein rings or strong deflection of the back transiting source, while the latter is observed through increase of flux of small mass objects, without an observable deflection effect.
Weak shear lensing, by clusters of galaxies, leads to the elliptical distortion observed in the shape of background galaxies. The distortion can provide a direct measure of radial mass distribution of the observed cluster (e.g. Kaiser & Squires, 1993; Fahlman et al., 1994) assuming a regular shape of the background galaxies. Finally, weak lensing magnification concentrates the flux from background sources, resulting in an increased source count (Kaiser et al., 1995). However, it also decreases the number of observable galaxies due to the magnification effect.

1.3.3 Microwave observations

The first computation of the distortion of the CMB spectrum through IC scattering was done by Weymann (1965, 1966). As previously mentioned, Section 1.1, the SZE effect can be detected in the microwaves as a decrease of photon from the CMB background, Figure 1.4. This effect results in a distortion in the black body shape of the CMB and has become one of the most effective tools for searching galaxy clusters. Unlike X-ray observations, the SZE is independent by the redshift of the source responsible for the up-scattering of the CMB photons, making it detectable in maps such as the one from Planck Collaboration et al. (2011), enabling the detection of clusters at very high redshift. The SZE causes a decrease in the CMB intensity at frequencies < 218 GHz (Carlstrom et al.,

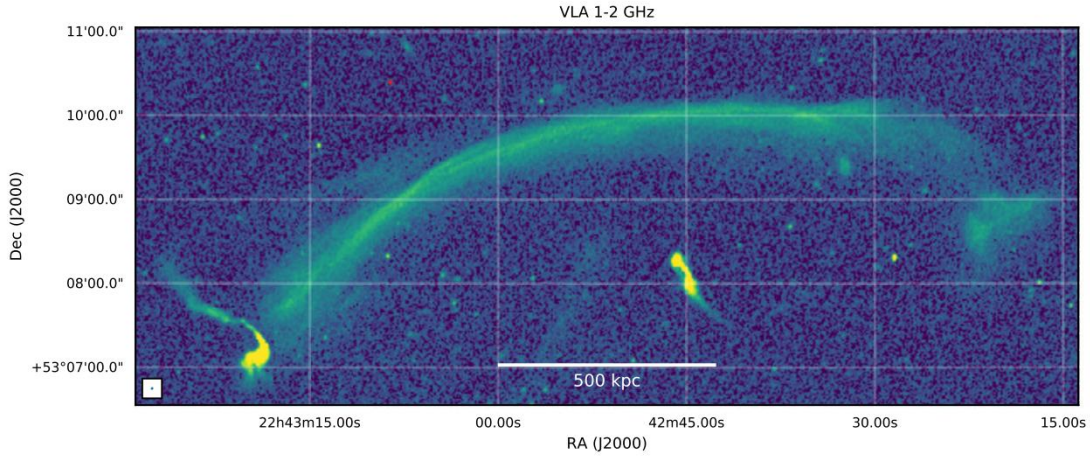

Figure 1.5: VLA 1–2 GHz high-resolution ($\sim 2\sigma$) and Sausage Cluster radio shocks. Credit: Di Gennaro et al. (2018)

2002), as well as an increase at higher frequencies, which allows a detection of the hot gas in clusters. Figure 1.4 shows the frequency shift of the CMB and the intensity computed for a massive cluster using the full calculation provided by Sunyaev & Zeldovich (1980).

1.3.4 Radio observations of non-thermal component emission

Galaxy clusters are rich of relativistic electrons, or cosmic ray electrons (CRe), which will be discussed later in Chapter 2. Together with magnetic field, residual turbulent motions and, potentially, cosmi ray protons (yet to be detected in the ICM), the non-thermal component of the ICM.
The first observation of radio emission from the galaxy cluster was attributed to Large et al. (1959), which discovered the presence of a diffuse radio emission coming from the Coma cluster, using the radio telescope at Jodrell Bank (working at at 408 MHz). Years later, this detection was confirmed through interferometric data from the Cambridge One-Mile telescope by Willson (1970). Jaffe & Rudnick (1979), in their search for radio halos, identified an extended emission region in the periphery region of the Coma cluster, near the strong radio source Coma A, that in the following work by Ballarati et al. (1981) was classified as a relic. The presence of extended synchrotron emission indicates the existence of large-scale ICM magnetic fields with a strength of the order of $\sim \mu$G, along with the presence of CRe.

Radio halos (e.g. van Weeren et al., 2019) are diffuse emitting regions with more or less a regular morphology, located in the inner region of clusters and extending over $\sim$1 Mpc. The observed radio emission from these halos is unpolarised and exhibits a power-law spectrum, which is indicative of a non-thermal source. The large observed volume of the radio halos cannot be motivated uniquely by the CRe injected by radio galaxies, as their radiative losses have to small timescales to sustain radio emission beyond a few 100 kpc from their injection point. Therefore, they must undergo in situ re-acceleration, with an efficiency comparable to the energy loss processes or, otherwise, be continuously injected in the ICM, by AGN processes or supernovae. the second order Fermi mechanism, or Fermi II is the process able to keep the CRe at such high energy after their injection.

In this scenario turbulence, together with a population of fossil electrons, plays a critical role in the emission process (see Section 2.5). In the rest of the thesis, we will refer to this class of sources as to "classical radio halos" (RH).

Radio relics, on the other hand, are structures found in the peripheral regions of the cluster and they have an extension of $\sim$ 1 Mpc (Bonafede et al., 2014). Their radio emission is strongly polarised and their spectrum is less steeper than the radio classical halos one. Observations of relics (Figure 1.5) provide a strong evidence for the presence of μG level magnetic fields and relativistic particles in cluster outskirts. They offer insights for the acceleration of relativistic particles at shock fronts at large distance, $\leq$ 3 Mpc, from the cluster centers (e.g. Bonafede et al., 2014; Vazza et al., 2012). In this case, the often observed spatial association with X-ray detected of shock waves suggests that these spectrum can be powered by Fermi I re-acceleration by merger shock waves, with typical Mach numbers ranging from 2 to 5. The steep spectrum observed in relics can be attributed to first order Fermi processes, or Fermi I.

More recently the work by Cuciti et al. (2022) has reported the discovery of a new family of halos that extend over the Mpc scale and fill all the volume within R_{500}. Those "mega radio halos" prove that the magnetic field extend over the radio halo limit and also open new questions about the processes involved in making such region observable. This is the more relevant class of halo regarding this Thesis work.

1.4 Mega radio halos

Mega radio halos (MH) are the faintest and most extended radio sources observed so far in clusters of galaxies. They have been discovered in 2022 using LOFAR, and my Thesis is devoted to test their formation mechanism. The intensity of their emission was found to be 20 times lower than the RH intensity, which makes these structures very challenging to detect and explains why they remained unobserved for so long. So far, the observations have been conducted only on four clusters (Figure 1.6): ZwCl 0634.1+4750, Abell 665, Abell 697 and Abell 2218. The detection was made possible only with the high sensitive instrumentation of Low Frequency Array (LOFAR van Haarlem et al., 2013). These targets were selected from the Planck Sunyaev-Zel'dovich catalog (Ade et al., 2016) of clusters, and were matched with sources present in the LOFAR Two Meter Sky Survey (LoTSS; Shimwell et al., 2019, 2022). Only Abell 697 was found at a slightly higher redshift than the others, $z = 0.28$ respect to the others at $z \approx 0.17$. It is also the most massive one with $M_{500} = 10.99 \times 10^{14}$ M$_\odot$, where M_{500} is the mass within R_{500}. Regarding the other three targets, we can see that the mass is slightly lower ZwCl 0634.1+4750 has $M_{500} = 6.65 \times 10^{14}$ M$_\odot$, Abell 665 has $M_{500} = 8.86 \times 10^{14}$ M$_\odot$ and Abell 2218 $M_{500} = 5.58 \times 10^{14}$ M$_\odot$. All these clusters have undergone dynamical interactions with sub-clusters and were already known to host RH (Giovannini & Feretti, 2000; Cuciti et al., 2018, 2021).

The radial profiles of surface brightness (Figure 1.7) clearly show the difference between the two components, i.e. the RH and MH. The former is characterised by a sharp radial decline that stops at $\sim 0.4R_{500}$, Abell 697 shows only a slight slope variation and the RH brightness profile shows a different slope with respect to the other three. The radio profile in the MH region, between $0.4R_{500}$ and R_{500}, shows that the surface brightness tends to remain quite constant, and that it steepens again at about R_{500}. The surface brightness of the MH is approximately a factor 10 lower than the surface brightness of

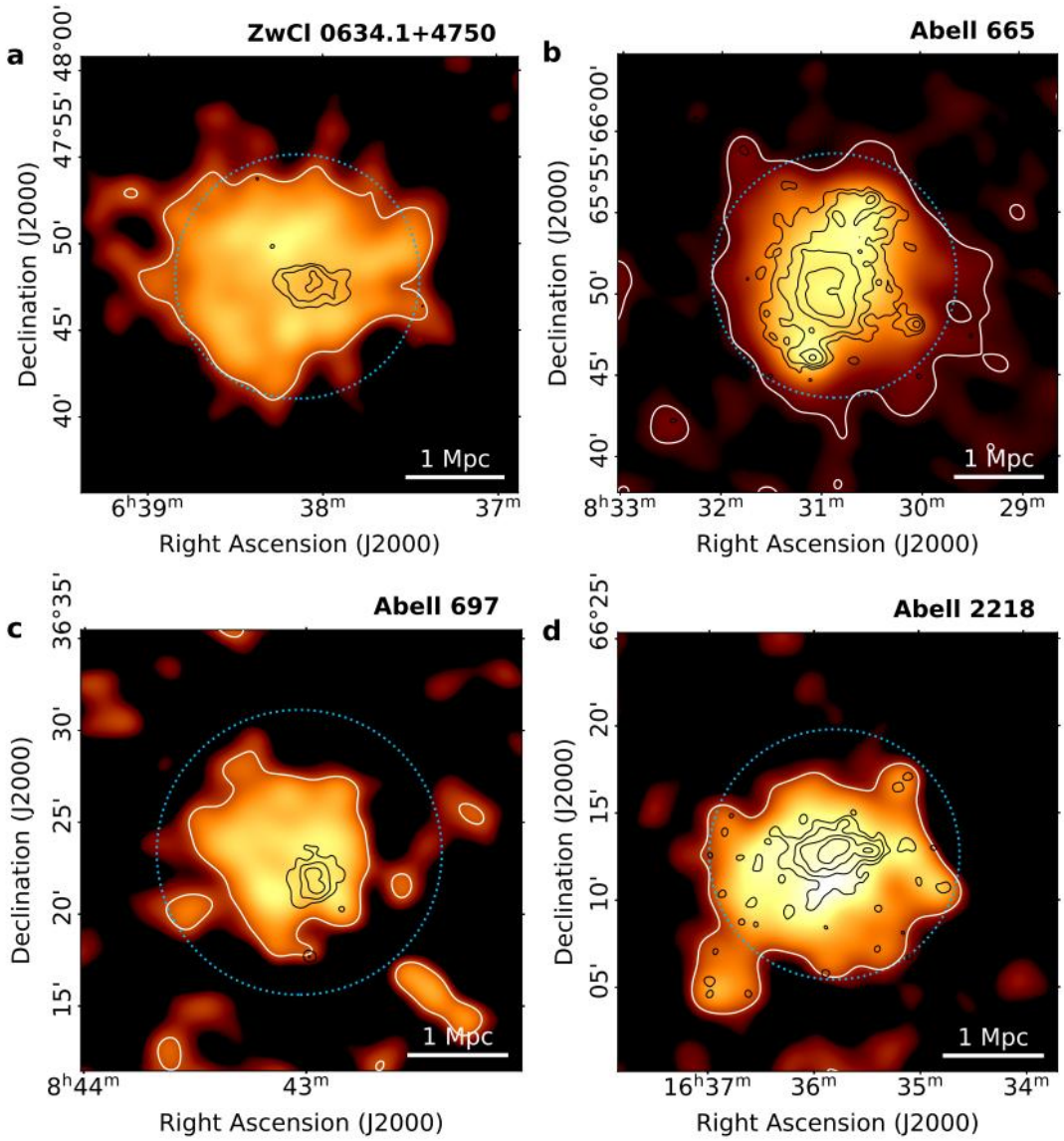

Figure 1.6: LOFAR 144 GHz radio images of ZwCl 0634.1+4750 (a), Abell 665 (b), Abell 697 (c) and Abell 2218 (d). The dotted circles represent R_{500}. Black contours: LOFAR 144 MHz at 30" resolution, showing the location of the radio halos. Orange image and white contours: LOFAR 144 MHz image at 2" resolution. Credit: Cuciti et al. (2022)

the central region, with the average emissivity $\sim 20 - 25$ times lower than the emissivity of radio halos. It was also possible, by adding one additional observation at even lower frequency ~ 50 MHz, to retrieve the spectral index, which was defined as $S(\nu) \propto \nu^{\alpha}$. That was possible only in the case of two clusters, ZwCl 0634.1+4750 with $\alpha = -1.62 \pm 0.22$ and Abell 665 which has a spectral index of $\alpha = -1.64 \pm 0.13$. In both cases, the MH spectrum results steeper than the one of the inner radio halo, thus highlighting the evidence of a different class of halo and the existence of different mechanisms. The properties of the ICM that can be inferred from these observations are very interesting. While the intensity remains approximately constant in such an extended region, the medium den-

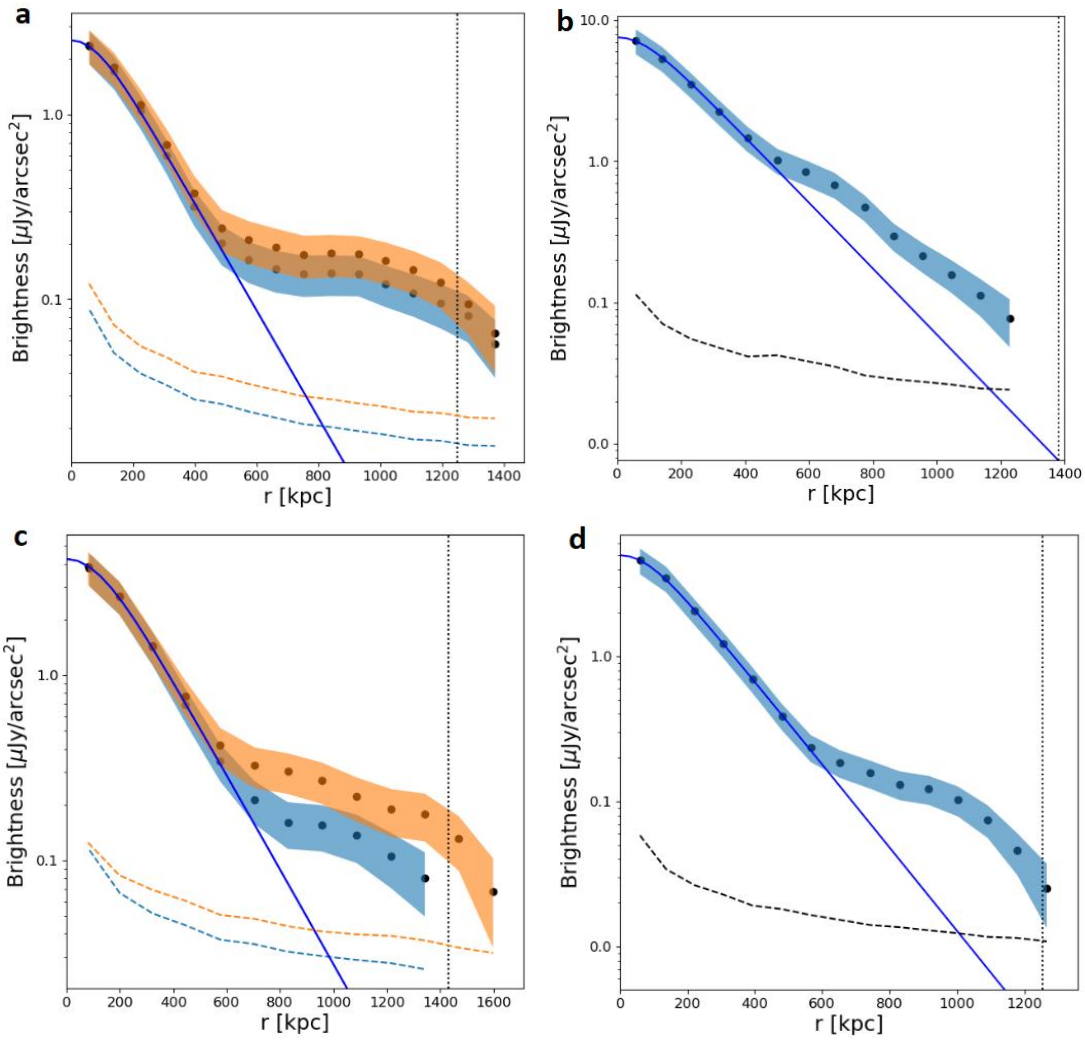

Figure 1.7: Surface brightness profiles of ZwCl 0634.1+4750 (a), Abell 665 (b), Abell 697 (c) and Abell 2218 (d). For ZwCl 0634.1+4750 and Abell 697, the profiles were derived within the entire virial radius (blue shaded region, panels b and d) and semi-annuli of the cluster (orange shaded region, panels a and c). The vertical line represents R_{500} while the shaded region represents 1σ uncertainty. Credit: Cuciti et al. (2022)

sity decreases by a factor 5 (Cuciti et al., 2022). This implies that the energy of the non-thermal component must become higher than the gas thermal energy, which, as the X-ray observations proved, tends to decrease with the distance from the center following a isothermal β-model. Therefore, to explain these trends it is necessary that the energy of the CRe remains constant at each radius, which also means that the energy losses should not exceed the amount of energy gained from re-acceleration.
This class of clusters has been only observed in merging clusters, as mentioned before, which suggest that turbulence and, consequently, the Fermi II processes have high efficiency. Turbulence can be the main mechanism capable of sustaining CRe at such high energy in a region of 10 Mpc^3. Moreover, the existence of such emission in a volume 30 times larger the RH one, is a strong proof of the existence of an extended magnetic field

that fills all the volume within, and probably beyond, R_{500}.

1.5 Aim and outline of the thesis

This thesis work aims to study the turbulence re-acceleration scenario in the region of MHs within the galaxy cluster. My analysis will infer whether the combination of the gas thermodynamic properties and turbulence is sufficient to explain the observed radiation. The re-acceleration model adopted in this Thesis, as described by Brunetti & Vazza (2020), assumes the prevalence of solenoidal and strong super-Alfvénic turbulence.
The thesis is organised as follows. In Chapter 1, I introduce the history of observations of galaxy clusters and their role in developing the modern theoretical understanding of the cosmological model. The introduction also provides a description of the observational properties, including X-rays, optical, and radio wavelengths. Finally, it gives an overview of the latest discoveries that motivate my thesis work. In Chapter 2, I focus on the key physical properties of the ICM. I explore the fundamental laws governing plasma behavior, including both shock and turbulent re-acceleration mechanisms, as well as the various loss mechanisms experienced by cosmic rays (CR). In Chapter 3, I provide information on both the simulations and the scripts that I implemented to analyse the evolution of radio emitting electrons. Moreover, I discuss the method used to retrieve the magnetic field present in the simulated volume. The results, which are reported in Chapter 4, show that turbulent re-acceleration can sustain high-energy electrons for a long time, approximately 5 Gyr, from their injection time. This result contradicts the classical understanding of CRe lifetime, which is estimated to be shorter. The turbulent re-acceleration results are able to reproduce the profiles observed by Cuciti et al. (2022) and therefore validate the adopted model. These results have been presented in a letter to Astronomy & Astrophysics (Beduzzi et al. (2023), arXiv:2306.03764).

Chapter 2

The physics of the intra-cluster medium and of cosmic rays

This chapter that will follow is focused on the key physical properties of the ICM. It will explore the fundamental laws governing plasma behavior, including both shock and turbulent re-acceleration mechanisms, as well as the various loss mechanisms experienced by CR.

2.1 Radio emission

It has been long debated whether the origin of RH was due to hadronic and turbulent re-acceleration. In the hadronic model, radio emitting electrons are produced by the hadronic interaction between CR protons and ICM protons (Blasi & Colafrancesco, 1999), while in the turbulent re-acceleration model electrons are accelerated by merging induced turbulence. Evidences against the hadronic model have been drawn from the integrated radio spectral (Brunetti et al., 2008) and the radial distribution of the radio emission in halos. The non detection of gamma-ray emission from the Coma cluster combined with statistical analysis of the non detection of gamma-ray emission from all clusters observed by the FERMI-LAT satellite, convincingly determined that RH cannot be of hadronic origin (see Brunetti & Jones, 2014, for a review). Turbulent re-acceleration of radio emitting electrons is now believed to be responsible for the generation of RH. More recently, turbulence has also been suggested to be the main process responsible for the generation of the new class of MH (Cuciti et al., 2022). In the upcoming chapter, I will delve into a detailed analysis of the efficiency of turbulent re-acceleration in driving the acceleration of relativistic electrons.

2.2 Intra-cluster medium microphysics

As mentioned in the previous chapter, the ICM is primarily composed of plasma that collapses during the formation of DM halos, and reaches a dynamical equilibrium within the cluster potential well. The advection of gas gives rise to different mechanism including shocks, turbulence and adiabatic transformations. These processes result in a wide range of gas temperatures, between $10^7 < T < 10^8$ K within R_{500} and set the electron number density between $10^{-4} < n_e < 10^{-3}$ cm^{-3}. Observations indicate that the magnetic field

in the ICM vary between $10^{-1} \lesssim B \lesssim 10\ \mu$G. All these quantities depend on the distance from the center, as demonstrate by both from X-ray and radio observations.

The mean free path of a charged particle in a fully ionised plasma, without a magnetic field and with a Maxwellian distribution of velocities, is completely determined by Coulomb collisions and it was determined by Spitzer (1956):

$$\ell_{\rm mfp} \simeq 15 \left(\frac{n_{\rm e}}{10^{-3}\ {\rm cm}^{-3}}\right)^{-1} \left(\frac{\rm kT}{8\ {\rm KeV}}\right)^{2} \left(\frac{40}{\ln\Lambda}\right) \quad {\rm kpc}\ , \tag{2.1}$$

where $\ln\Lambda$ is the Coulomb logarithm, that is the integral of $\int b^{-1} db$ where b is the impact parameter. If now we compare the $\ell_{\rm mfp}$ to the Larmor gyroradius-scale of thermal particles (Braginskii, 1965):

$$r_{\rm L} \simeq 3 \cdot 10^{-12} \left(\frac{kT}{10\ {\rm keV}}\right) \left(\frac{B}{\mu{\rm G}}\right)^{-1} \quad {\rm kpc}\ . \tag{2.2}$$

It can be easily seen that $\ell_{\rm mfp} \gg r_{\rm L}$, and in this regime the plasma can be considered weakly collisional and each instability in the medium can generate non-negligible and growing fluctuations in the plasma. Also, for this kind of medium, wave-particles interactions have more relevance than Colombian interaction between the particles itself.

2.3 Fermi processes and the origin of cosmic rays

In order to understand the fundamental processes responsible for CR acceleration in the ICM, it is essential to introduce the Fermi model of CR acceleration. This model establishes the basis for elucidating the energy distribution of CR and the acceleration processes generates by the interaction of relativistic particles with the ICM.

Fermi (1949) formulated acceleration models to explain the presence of CR particles reaching our planet, and plausibly accelerated by the interstellar medium. One of the concept of Fermi is the collision of charge particles with the "clouds", representing region in space with a specific magnetic field intensity. The collision between a cloud and a particle happens without direct contact and it can be considered elastic. It can demonstrate that the relative motion between the charged particle and the cloud can produce a variation in the kinetic energy of the former, as an effect of the acceleration by the "motional" electric field.

Considering the Lorentz force acting on a particle with a charge q and a velocity $\vec{v}$ that moves with opposite direction of a cloud with velocity $\vec{V}$ and magnetic field $\vec{B}$. The charged particle experiences an electric field $E \approx -\vec{V} \times \vec{B}$. Thus, the total force experienced by the charge is given by the Lorentz force:

$$\vec{F} = m\frac{d\vec{v}}{dt} = q(\vec{E} + \vec{v} \times \vec{B})\ . \tag{2.3}$$

By substituting the electric field and multiplying by the velocity of the particle, we obtain:

$$\begin{aligned} \vec{v} m\frac{d\vec{v}}{dt} &= q\vec{v} \cdot \left(-\vec{V} \times \vec{B} + \vec{v} \times \vec{B}\right)\ , \\ \frac{d\left(m\vec{v}^2/2\right)}{dt} &= q\left(-\vec{v} \cdot \vec{V} \times \vec{B} + \vec{v} \cdot \vec{v} \times \vec{B}\right)\ , \\ \frac{d\left(m\vec{v}^2/2\right)}{dt} &= -q\vec{v} \cdot \left(\vec{V} \times \vec{B}\right)\ . \end{aligned} \tag{2.4}$$

The last equation shows that the kinetic energy of the charge can only change due to the interaction with the magnetic field of the cloud while the particle is crossing this system in relative motion with it.

As described in the original paper by Fermi, the presence of uniform magnetic field causes the motion of a charged particle to be split into two components. One component, parallel to the magnetic field lines $\vec{B}$ only contributes at the linear motion and is denoted with $\vec{v}_{\parallel}$. The other component is directed perpendicularly to the field due to the Lorentz force and it is called $\vec{v}_{\perp}$. Thus, while crossing a magnetised "cloud", the particle moves in a spiral motion which the pitch angle of the spiral increases and decreases, respectively, with a field intensity increases or decreases following the relation:

$$\frac{\sin^2\theta}{|\vec{B}|} \approx \text{const} \ . \tag{2.5}$$

As the particle approaches a region of increasing local field intensity, θ must increase until $\sin\theta$ reaches its maximum value of one, at this point the particle is reflected back along the same line of force and spirals backwards. This mechanism, proposed by Fermi and known as first order Fermi acceleration (or Fermi I), is essentially responsible for the "mirror" reflection in particle-cloud collision. On the other hand, if particle is moving toward a region of decreasing field intensity, it will lose energy upon reflection.
These mechanism are capable to accelerate charged particles up to ultra-relativistic energies. In general, Fermi I processes are highly efficient, they can transfer a large amount of energy in a short period of time. By means of these two mechanisms, Fermi predicted that by continuously gaining a small but constant amount of energy through mirror reflection, particles could acquire the necessary energy to account for the observed distribution of CR during that epoch.

The exact amount of energy gained can be easily computed using the principles of elastic collisions in the context of special relativity. By considering a particle with velocity v colliding with a cloud of velocity V (both velocities are magnitudes of their respective velocity vectors) and a pitch angle θ, a straightforward calculation shows that:

$$\Delta E = E^* - E = E\left[2\,\frac{Vv\cos\theta}{c^2} + 2\left(\frac{V}{c}\right)^2\right] \ , \tag{2.6}$$

where E^* is the energy of the particle after the collision, $E = \gamma mc$ and c the speed of light. Now we can evaluate the mean value of the energy gain $\langle\Delta E\rangle$ for random particles, that can be observed, with few assumptions. Firstly, we can assume that there were not preferential direction along which particles can collide with the clouds, meaning a mean particles velocity $\langle v\rangle = 0$ (this was the first assumption made by Fermi that will reveal to be untrue, see Section 2.5). For $(V/c)^2 \cdot E$, this therm is always positive, so it follows that the particles always gain energy. However, the velocities of interstellar clouds in the Milky Way are very small compared to the light speed, and the number of collisions are not enough to allow such high energy, also because in the interstellar medium ionisation losses prevent particles acceleration. Indeed, the origin of the galactic CR has been later explained through Fermi I processes, triggered by the shocks launched by supernovae explosions.
This model can be used to built the energy distribution of the CR. Therefore, assuming that a CR gain energy from each collision, after k interactions its energy will be $E = \beta^k E_0$ with E_0 initial energy, where β is the amount of energy gained defined as the ratio between

ΔE and the initial energy E. Now we define the parameter P (≤ 1) such that $1-P$ is the probability that a particle gets accelerated again after a collision in the same region of space (otherwise, the particle with leave the acceleration region and it will not be further accelerated by this mechanism anymore). Also, we can define the number of particles with energy greater than the energy higher after k interactions, as $N(>E) = P^k N_0$ where N_0 is the amount of particles with energy greater than the initial energy. By studying the ratio between N/N_0 and E/E_0, we determine the energy distribution as a function of the energy:

$$\frac{N(E)}{N_0} = \left(\frac{E}{E_0}\right)^{\xi} , \tag{2.7}$$

where, ξ is defined as:

$$\frac{\ln N/N_0}{\ln E/E_0} = \frac{\ln P}{\ln \beta} = \text{const} = \xi , \tag{2.8}$$

and $\xi \leq 0$, since $P/\beta \leq 1$. Since particles that can reach energy E can be accelerated to higher energies, we can see that the previous equation is a cumulative function:

$$N(E)dE \propto E^{\,\xi-1} = E^{-p} . \tag{2.9}$$

Here we define:

$$p = 1 - \frac{\ln P}{\ln \beta} \geq 1 . \tag{2.10}$$

The value of p can be computed from the diffusive shock acceleration model (Section 2.4), and it determines the maximum energy E reached by particles.

The acceleration model proposed by Fermi has been reviewed and updated with to provide a more accurate description of the physical phenomena, taking also into account additional extragalactic processes. Initially, Fermi only considered the acceleration mechanism from the interaction of the Galactic clouds with CR. The final computation of the acceleration models for Fermi I and II are respectively reported in Sections 2.4 and 2.5.

Referring to Equation 2.6 we observe two terms, the first is related to the velocity of the particle, while the latter depends entirely on the cloud velocity. If the first term is dominant, we are observing Fermi I acceleration, while, if the second term dominates, Fermi II is the main mechanism. Fermi I can be caused by shocks in the medium, usually due to supernovae explosion or to shocks induced by merger between clusters of galaxies. Fermi II are otherwise attributed to turbulence in the medium, that is able to twist the magnetic field lines. In my Thesis, this second term is assumed to be the dominant one to produce the large-scale acceleration of electrons responsible for MH. Those two effects will be treated in the next two sections.

2.4 Diffusive shock acceleration

In the reference frame of the shock, the downstream velocity is always lower than the upstream velocity. Therefore, considering the magnetic field of the clouds, as defined in the Fermi picture, which are moving upstream, they will appear to move at a certain velocity $\Delta V = |u_{\text{up}} - u_{\text{down}}|$ (in the shock rest frame) relative to a charged particle that faces the shock. After the acceleration, the particle may gain enough energy to cross the shock again,experiencing the downstream velocity and undergoing the same Fermi processes with a $\Delta V = |u_{\text{up}} - u_{\text{down}}|$. If the particle gyroradius after the shock is large

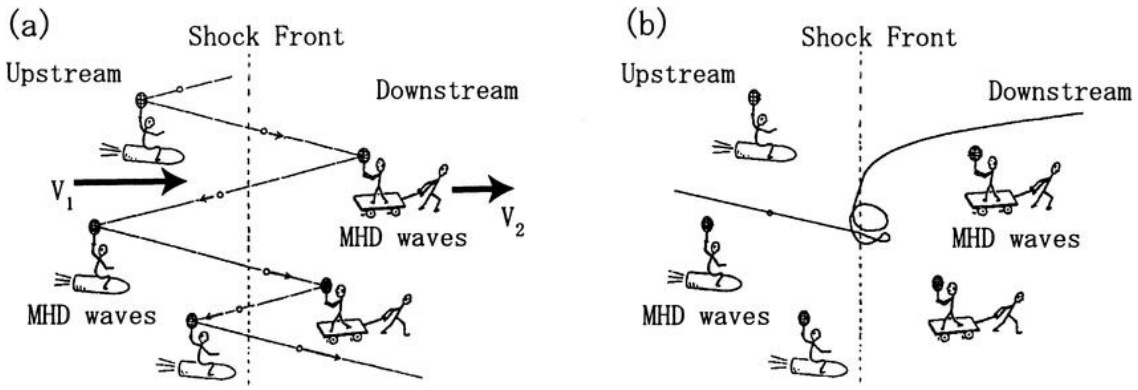

Figure 2.1: Cartoons of the diffusive shock acceleration mechanism (a). Plasma heating/acceleration that occurs in the shock transition/shock front region (b). From: Hoshino (2001).

enough, it can undergo the same process multiple times, making the Fermi I mechanism highly efficient in accelerating particles to very high energy. However, If the gyroradius remains too small, the particle only experiences a small increase of energy, thus, resembling more a heating process rather than an acceleration. This mechanism describe the diffusive shock acceleration. From the diffusive shock acceleration (DSA) picture we can extract the value of of the exponent p of Equation 2.10.
In the next lines will be provided a full derivation of the maths beyond the DSA picture. In this particular calculation, we will assume that only Mach numbers $M \gg 1$ and already relativistic particles are considered, implying $v \approx c$. At each shock, these particles will undergo a velocity jump denoted by $V = u_1 - u_2$, where u_1 represents the upstream velocity and u_2 represents the downstream velocity. Now let us assume that the number of particles within the solid angles θ and $\theta + d\theta$ is $\propto \sin\theta d\theta$, and that the rate at which particles cross the shock is $\propto c\cos\theta$. Given that the energy gain is described by Equation 2.6 where we know that in the case of Fermi I acceleration the first term of the equation is grater then the second term, the energy of each half crossing will be approximately:

$$\frac{\Delta E}{E} = \frac{1}{2}\frac{2vV}{c^2}\cos\theta \approx \frac{V}{c}\cos\theta \tag{2.11}$$

Then the medium value of the energy gain is given integrating over all the different angles, in this case the integration angle will be within $\theta \in [0, \pi/2]$ since we are considering only half crossing. It results:

$$\left\langle \frac{\Delta E}{E} \right\rangle = \frac{\int_0^{\pi/2} c\,\cos\theta \frac{V\cos\theta}{c}\sin\theta d\theta \int_0^{\pi/2} d\phi}{\int_0^{\pi/2} c\,\cos\theta\sin\theta d\theta \int_0^{\pi/2} d\phi} = \frac{2V}{3c}\ . \tag{2.12}$$

The energy gained by the particle after two jumps over the shock surface, one in the upstream direction and the other in the downstream direction, is:

$$\left\langle \frac{\Delta E}{E} \right\rangle = 2\frac{2V}{3c} = \frac{4(u_1 - u_2)}{3c} = \frac{E_{i+1} - E_i}{E_i}\ , \tag{2.13}$$

where E_i is the particles energy at t_i. Since we are in the strong shock case ($M \gg 10$), for which $u_2 = u_1/4$ and since $E_{i+1} = \beta E_i$:

$$\beta = 1 + \frac{4}{3}\frac{u_1 - u_2}{c} = 1 + \frac{u_1}{c}\ . \tag{2.14}$$

Now, we need to compute the value of the probability P for the particle to undergo further acceleration processes. We can then define the rate of particles per unit of time that begin an acceleration cycle as $R_{\rm in}$, and the rate of particles per unit of time that are advected over the shock surface afterwards as $R_{\rm out}$, both measured in units of time. The ratio between these two quantities will give us the probability that a particle will not be accelerated again, namely $1 - P = R_{\rm in}/R_{\rm out}$. The number of particles entering the shock region for an isotropic distribution is:

$$N_{in} = \frac{n}{4\pi}\int_{\Omega} d\Omega = \frac{n}{4\pi}\int_{0}^{\pi/2} \sin\theta d\theta \int_{2\pi} d\phi \ , \tag{2.15}$$

the rate $R_{\rm in}$ is then found by the product of the number of particles times their velocity across the shock ($c\cos\theta$):

$$R_{in} = \frac{nc}{4\pi}\int_{\Omega} \cos\theta d\Omega = \frac{nc}{4} \ , \tag{2.16}$$

while the rate of lost particles is $R_{\rm out} = nu_2$. Therefore:

$$1 - P = \frac{R_{\rm in}}{R_{\rm out}} = \frac{nu_2}{nc/4} = \frac{u_1}{c} \ll 1 \ , \tag{2.17}$$

so the actual value of P will be:

$$P = 1 - \frac{u_1}{c} \ . \tag{2.18}$$

Using the equation 2.10 and substituting β and P previously derived, after some maths we obtain:

$$N(E) \propto E^{-2} \ ; \ p = 2 \ . \tag{2.19}$$

With a similar derivation we can retrieve the dependence between p and the Mach number, for each kind of shocks:

$$p = 2\frac{M^2 + 1}{M^2 - 1} \ . \tag{2.20}$$

Here we can see that p tends to 2 when $M \to \infty$ otherwise the steepness increases at decreasing value of the Mach number.

Shocks from galaxy clusters mergers release a very large amount of energy $\sim 10^{64}$ erg. It can be observed that the clusters approach each other with relative supersonic velocity, this imply the formation of weak shock waves with $M \sim 2$ (Sarazin, 1999). These shocks increase in strength as they moves outside the cluster cores due to the decrease in temperature. Moreover, the so called external shocks, that result from the continuous accretion of matter at Mpc distance from the center of the cluster are even stronger than the previous ones ($M \gg 10$). In fact, they develop in colder region outside the cluster, that allow they to reach higher Mach number. The difference between those two shock waves resides in the amount of energy carried by the waves, since the least develop in lower density region, they dissipate less energy compered to weaker but most internal shocks (Figure 2.2).

2.5 Turbulence

The Fermi model of acceleration can explain the re-acceleration of radio emitting electrons in the ICM. Taking into account Equation 2.6, efficient acceleration of CR

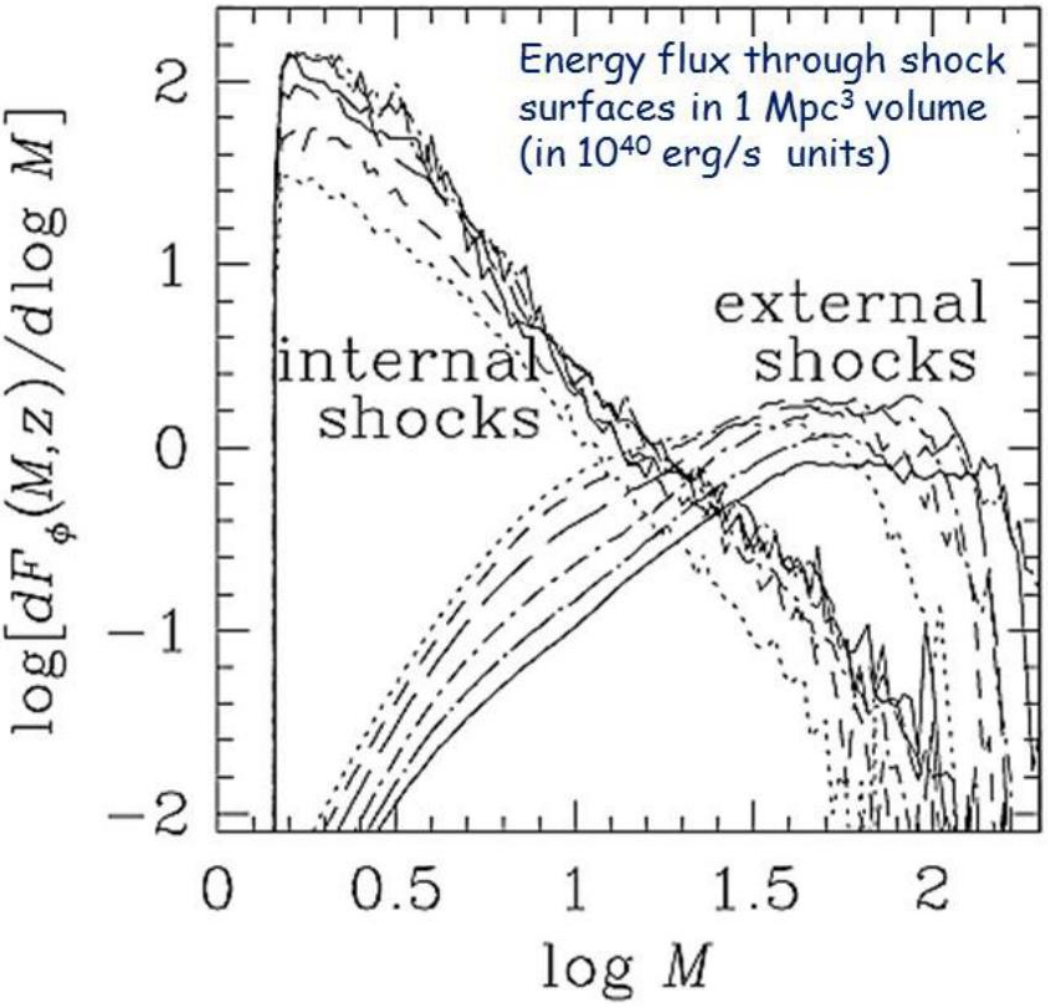

Figure 2.2: Energy flux distribution at the surface of the shocks as function of the mach number from numerical simulations. Credit: Ryu et al. (2003).

occurs when a particle encounters more clouds moving in the opposite direction ("head-on collisions") rather than those moving in its same direction ("rear-on collisions"). This phenomenon can be understood by considering a fixed mean free path λ for a particle in the galactic medium. The collisions happen with a characteristic frequency defined as $\nu = 1/\tau \sim \Delta v/\lambda$. When considering a particle colliding with a cloud moving in the same direction, the relative velocity is given by $\Delta v = |v + V|$, while for opposite directions $\Delta v = |v + V|$. As consequence, the frequency of collision at opposite velocity is higher than the former.
Considering now the random distribution of collision angles as $P(\theta)d\theta \propto \sin\theta d\theta$, and applying similar logic to Fermi I, we can integrate over all possible angles, that range from $\theta \in [0, \pi]$, and eventually find:

$$\langle \Delta E \rangle = \frac{8}{3}\frac{V^2}{c^2}\langle E \rangle \ . \tag{2.21}$$

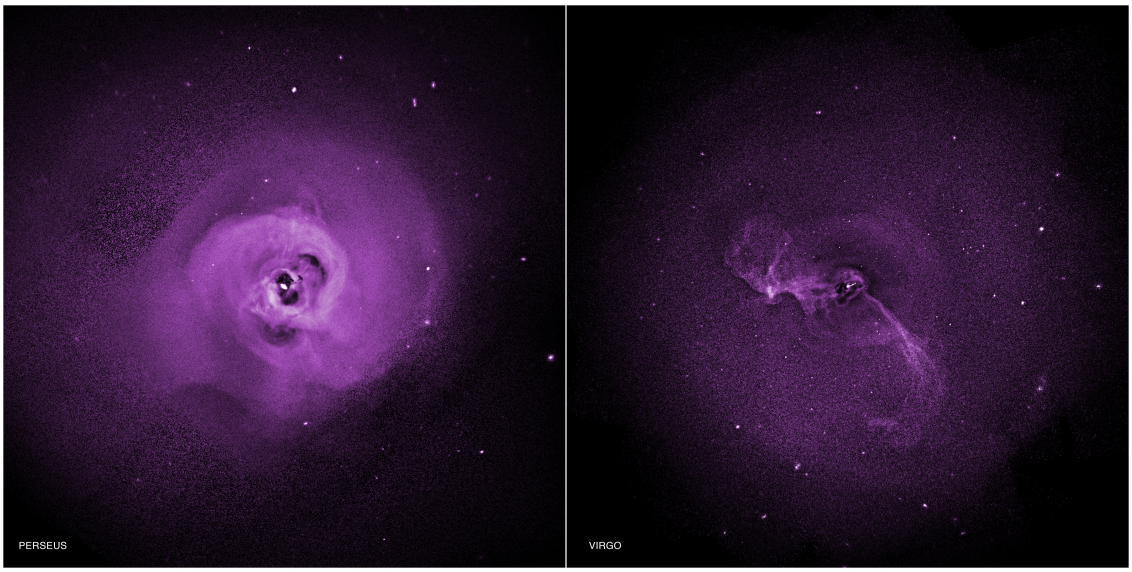

Figure 2.3: ICM X-ray image of the heating rate due to the dissipation of turbulence observed in the Perseus and Coma clusters from the Chandra observatory. Credit: NASA/CXC/Stanford/Zhuravleva et al. (2014).

This acceleration can leads to an exponential increase in energy, as already reported in Section 2.3.

In general, turbulence plays a fundamental role in the acceleration of CRe that produce the RHs. Galaxy clusters are dynamically active systems and their mergers are the main causes of turbulence. In fact, the perturbation of the medium due to this merger can generate stochastic motions in the ICM. Turbulence not only causes CRe acceleration but also facilitates gas heating through viscous dissipation in the ICM (Zhuravleva et al., 2014), as observed in the X-ray observations of the Perseus and Coma clusters shown in Figure 2.3. Moreover, the stretching and folding of magnetic field lines can lead to small scale dynamo amplification of magnetic fields by dissipating a small fraction of the turbulent energy.

To describe the fluid dynamics of the ICM, we can use the Navier-Stokes equations:

$$\frac{\partial \vec{v}}{\partial t} + \vec{v} \cdot \nabla \vec{v} = \frac{\nabla P}{\rho} + \nu \nabla^2 \vec{v}, \tag{2.22}$$

where $\vec{v}$ is the fluid velocity, P is the pressure, ρ is the density, and ν is the kinematic viscosity. The Reynolds number can be obtained from the ratio between the inertial term and viscous force expressed in Equation 2.22, namely:

$$R_e = \frac{\vec{v} \cdot \nabla \vec{v}}{\nu \nabla^2 \vec{v}}, \tag{2.23}$$

also, the inertial term correlates with the vorticity $\vec{\omega} = \nabla \times \vec{v}$:

$$\vec{v} \cdot \nabla \vec{v} = -\vec{v} \times \vec{\omega} + \frac{\nabla |\vec{v}|^2}{2}. \tag{2.24}$$

When the Reynolds number number is larger than a critical value, that is usually $> 10^2$, the velocity fluctuations cannot be dissipated by viscosity and generate a cascade of

vortical motions. This phenomenon is called "fully developed turbulence", where fluid perturbations are present at all scales, and an exact solution of the flow dynamics is not possible.
Over the years, different approaches have been developed to extract information from the physics of turbulent motion. One of the most significant developments in the study of turbulence was made by Richardson (1922). In his work, he described a turbulent flow as composed of different eddies of a given size ℓ and with a given velocity dispersion v_ℓ. Each eddy remains stable for a certain amount of time, which depends on its velocity fluctuation and size $\tau_\ell \sim \ell/v_\ell$. Eventually, each eddy breaks up into smaller eddies, which also last for a certain amount of time before breaking up further, and so on. This process continues until it reaches the smallest scales $\ell_{\rm visc}$ where the viscosity force can dissipate the kinetic energy into heat.
Two decades later, Kolmogorov (1941, hereafter K41) derived a scaling low, now known as "5/3 law", that allows to describe the statistics of the kinetic energy of the turbulent eddies across all the scales of the cascade. The main hypotheses in Kolmogorov theory, for stationary and incompressible turbulence, are: *local isotropy*: turbulent motions are isotropic and homogeneous within the inertial range; *first similarity hypothesis*: turbulent motions have a universal form that is uniquely determined by the viscosity ν and by the kinetic energy flux ϵ in unit of $\mathrm{m}^2/\mathrm{s}^3$; *second similarity hypothesis*: within the largest length scale of the perturbations and the smallest one, this range is called "inertial range", the statistics of the motions between the extremes of the length-scales have a universal form that is determined uniquely by ϵ, independent on ν. ϵ is then defined as:

$$\epsilon = \frac{v_\ell^2}{\tau_\ell} = \frac{v_\ell^3}{\ell}. \tag{2.25}$$

The maximum correlation scale of the flow is defined as ℓ_0 and the inertial range is defined within ℓ_0 and $\ell_{\rm visc}$ where also we found that ϵ =const. This means that velocity dispersion, time and length are all related by the Equation 2.25. Then this equation allows us to retrieve fundamental quantities of the turbulence within every spatial scale ℓ with velocity fluctuation v_ℓ, until the perturbation is fully developed and $\ell_{\rm visc} < \ell < \ell_0$.
By describing the velocity field in its Fourier series and by making the Fourier transform of Equation 2.22, Onsager (1949) was able to extract the fundamental result of the Kologorov model. Considering the kinetic energy flux transmitted from scale, to scale he determined the energy power-spectrum $E(k)$ ($k = 2\pi/\lambda$) in the Fourier space, which represents the amount of energy that contributes to the total variation of the mean modulus of the square velocity, namely $\langle \Delta v^2 \rangle /2$ for each spatial frequencies k. It can be expressed as:

$$\int_{k_{inj}}^{k_{visc}} E(k)dk = \frac{\langle \Delta v^2 \rangle}{2}. \tag{2.26}$$

According to the second similarity hypothesis $E(k)$ depends uniquely on a combination of ϵ and k. Dimensional analysis reveal that:

$$E(k) \propto \epsilon^{\frac{2}{3}} k^{-\frac{5}{3}}, \tag{2.27}$$

This behaviour "$-5/3$" has been observed at all the scales. The spectra of several clusters have also been suggested to be close to the K41 model, which, considering the condition of the ICM that is a compressible and non static medium, makes this model extremely versatile also in this context.

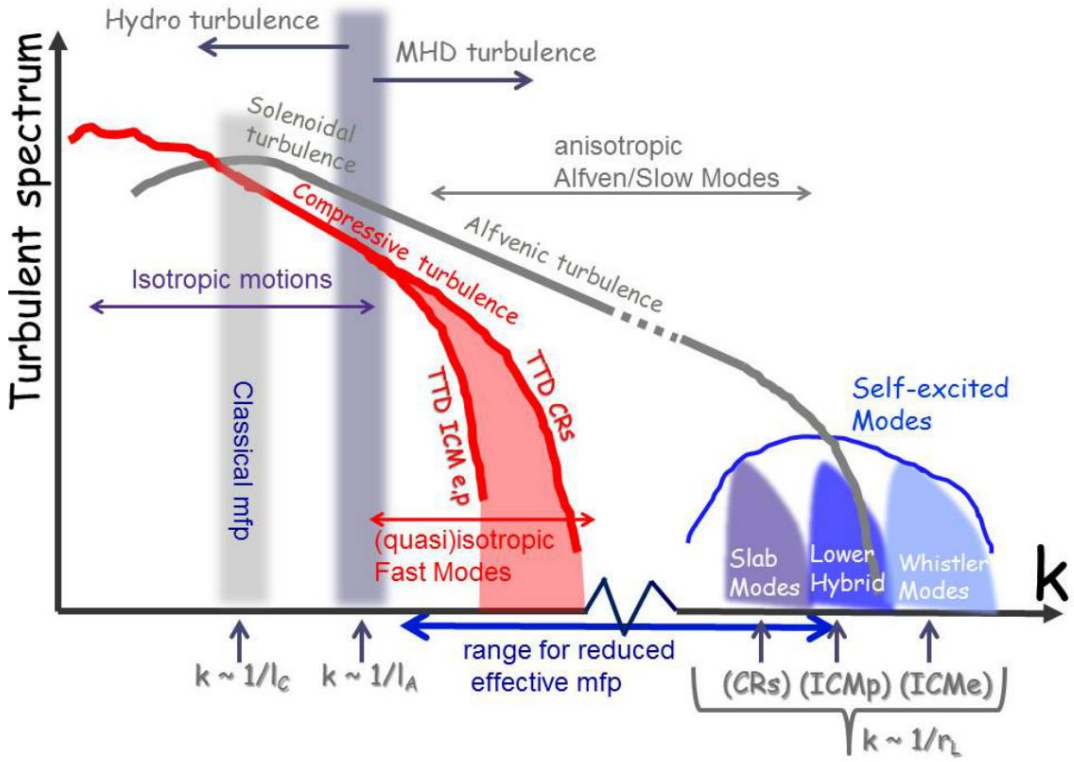

Figure 2.4: A schematic view of turbolence in the ICM. We can see the transition to MHD turbulence at $k \sim 1/\ell_{\rm A}$ while Coulomb ion length scale and the classical mean free path are plot at $k \sim 1/\ell_{\rm c}$. We can see that solenoidal turbulence develops an Alfvénic cascade at small scales while the fast and compressible modes get probably dissipated via transit time damping resonance with electrons and protons in the plasma. Some example of self-excited modes that are excited via CR or turbulent-induced instabilities, there are also shown: slab modes, lower hybrid waves, and whistler waves. Credit: Brunetti & Jones (2014).

Galaxy clusters are dynamic objects with various potential sources of turbulence, including the motion of galaxies within the cluster and cluster mergers. The latter, and in general all the motion on large scales, can rearrange the cluster structure. Turbulence is expected to form from core sloshing, shear instabilities and complex pattern of interacting shocks during mergers (Vazza et al., 2009; Ohno et al., 2002). The CR propagation in the ICM is strongly influenced by their interaction with the magnetic hydrodynamic (MHD) turbulence, specifically the Fermi II processes. MHD turbulence can be classified in three different modes (Goldreich & Sridhar, 1995): the slow incompressible and fast compressible MHD modes, and the Alvén mode. The slow and Alfvén modes can have low efficiency for the CR transport due to their anisotropic nature (Yan & Lazarian, 2002, 2004; Yan & Lazarian, 2008), in fact CR interact with multiple uncorrelated eddies during one gyro-orbit, essentially cancelling out gyroresonant contributions from each eddy (Chandran, 2000). While the compressible fast modes, whose velocities are independent of magnetic field direction are more isotropic (Cho & Lazarian, 2003). Therefore the CR transport depends on the MHD modes composition of turbulence. Large scale turbulent

motions are generated during cluster mergers, with typical scales of $\ell_0 \sim 100 - 400$ kpc and velocities of approximately $v_{\ell_0} \sim 300 - 700$ km/s (Brunetti & Lazarian, 2007). These motions are subsonic and have a Mach number of $M_s = v_{\ell_0}/c_s \approx 0.2 - 0.5$, where c_s is the speed of sound, but they are super-Alfvénic ($M_A = v_{\ell_0}/v_A \approx 5 - 10$). In this of environment the magnetic field lines are continuously stretched and tangled on scales larger than the Alfvén scale. Below this scale, turbulence is not able to twist magnetic field lines and it becomes MHD. This limit is found where $\ell_A \sim \ell_0 (v_{\ell_0}/v_A)^{\frac{2}{a-1}}$ where a is the slope of the velocity power-spectrum ($W(k) \propto k^{-a}$). With this condition the particles mean free path becomes $\sim \ell_A$ instead of the classical Coulomb ion mean free path $\approx 10 - 100$ kpc (Lazarian, 2006; Brunetti & Lazarian, 2007). These conditions lead to a Reynolds number $R_e \sim 1000$, that suggests that turbulence can be developed for all the inertial range starting from the largest scales (Figure 2.4). Also, at small scales, plasma kinetic instabilities generate waves at small resonant scales. The other types of waves that can be generated in the ICM are the slab/Alfvén modes that may be excited via streaming instability (Wentzel, 1974) or gyro-kinetic instability (Yan & Lazarian, 2011), or the whistler waves that may be excited via heat-flux driven instability (Pistinner et al., 1996), or lower hybrid electrostatic waves generated through the non-linear modulation of density in large amplitude Alfvén wave-pockets. All kind of waves (in frequency units) excited by turbulent motions are shown in Figure 2.4.
The turbulent modes in the ICM can exchange energy with the interaction with particles (Melrose, 1980; Schlickeiser, 2002). Acceleration of thermal particles to high energy is very inefficient (Chernyshov et al., 2012), so turbulent acceleration is supposed to re-accelerate already present CR rather than accelerate particles from the thermal pool.

2.6 Loss processes

Radiation emission by CR involves loss mechanisms that decelerate the motion of the particles. Energy losses through electromagnetic interactions result in the production of radiation, which is observable across various wavelengths of the electromagnetic spectrum. This section aims to provide an overview of the physical radiative processes involving relativistic particles. These mechanisms are characterised by different timescales that depend on the properties of the medium and the energy content of the CR. Figure 2.6 illustrates these different timescales under typical ICM conditions.

2.6.1 Hadronic processes

A brief discussion of the hadronic processes is needed in order to have a complete overview of the CR processes, also related to CR protons. In the typical conditions of the ICM (a central environment in my Thesis) CRe interact with the magnetic field of the medium and with the CMB photons, and loose most of their energy via radiative processes. CR protons typically undergo different loss processes. Relativistic protons can have highly energetic collisions either with low energy photons (from either the electron synchrotron radiation or an external photon field), as well with other thermal protons in the medium they are crossing. The result of the relativistic and low energy protons interaction is the creation of neutral and charged mesons, i.e. mainly pions that can decay into neutrinos, gamma-rays, electrons, and positrons. Finally, the last photo-hadronic process is the synchrotron radiation emission from a relativistic proton, but the magnetic

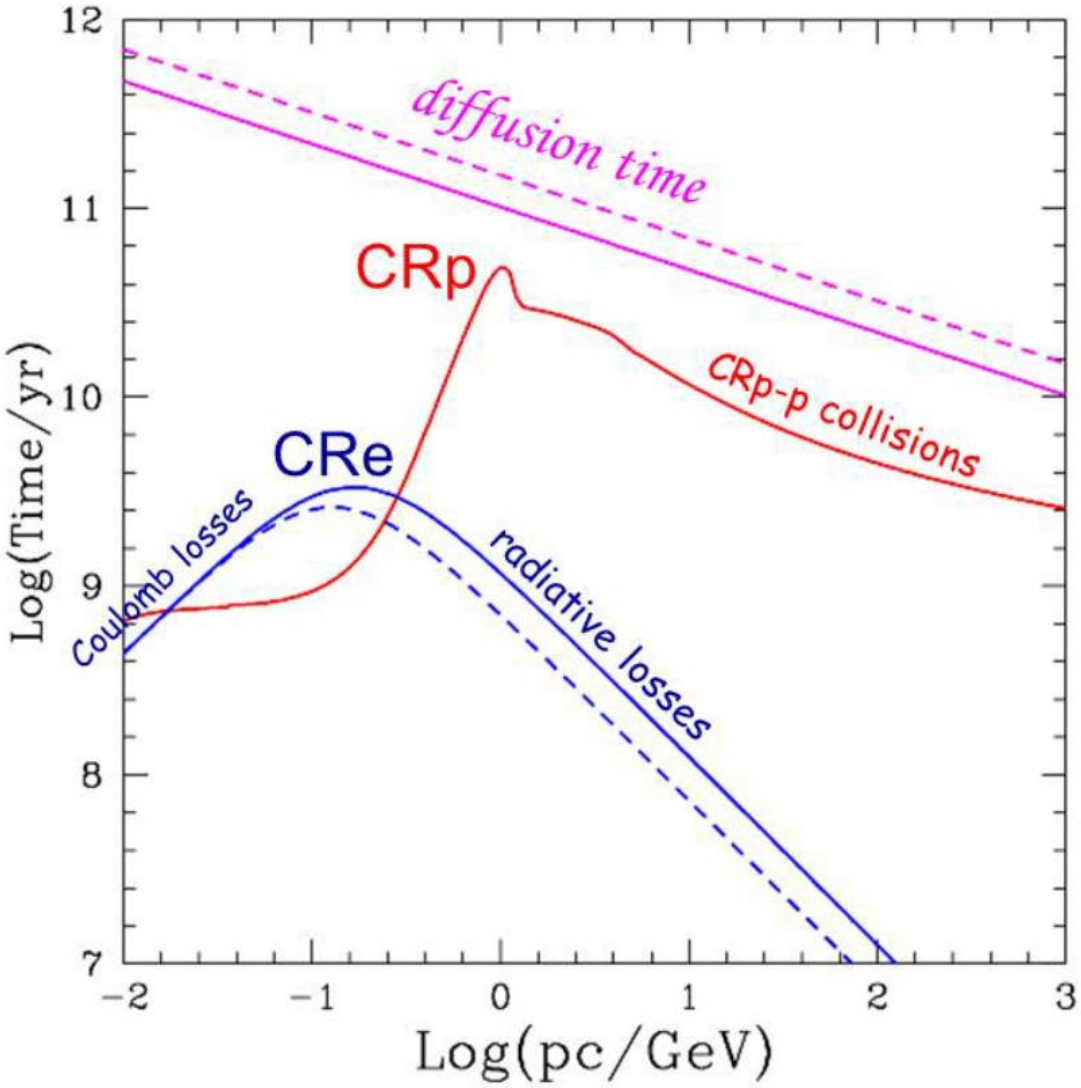

Figure 2.5: CR lifetime for protons (red) and electrons (blue) and the diffusion time on Mpc scales. At each energy level, the process with the smallest timescale is the one which dominates the evolution of particles with that energy. Credit: Blasi et al. (2007).

field needed to made the radiation visible in the lower frequency band is way to higher than the ICM one. This mechanism are negligible in our study since the lifetime of CR protons is close to, or larger than, the Hubble timescale (Figure 2.6). Since the main channel of energy losses in the cluster condition come from the p-p interaction, we can express its lifetime as (Brunetti & Jones, 2014):

$$\tau_{\rm pp}(p) \simeq \frac{1}{c\ n_{\rm th}\sigma_{\rm pp}}\ , \tag{2.28}$$

where $\sigma_{\rm pp}$ is the p-p cross-section and $n_{\rm th}$ is the number density of the thermal plasma protons.

Hereafter, I will the focus on the electrons radiative processes.

2.6.2 Synchrotron radiation

The emission of radio photons occurs when relativistic charged particles undergo acceleration in the presence of a magnetic field. Therefore, this mechanism represents the main character of this work and I provide a more detailed calculation of the mechanism. The radiation emitted from an electron that is accelerated due to a vector field variation of the magnetic field can be computed starting from the Maxwell equation and the Lienard-Wiechert potential for a charged particle in motion. Using the obtained electric field vector $\vec{E}$ and the magnetic field vector $\vec{B}$ we can find the emitted power as function of the solid angle starting from the Poynting vector:

$$\bar{S} = \frac{1}{\mu_0}\vec{E} \times \vec{B} \ , \tag{2.29}$$

where $\vec{E}$ represent the electric field vector, $\vec{B}$ the magnetic field vector. By using the Lienard-Wiechert potential, after some maths we can express the total power radiate from a charge under the solid angle $d\Omega$ with respect the position occupied by the charge, therefore integrating the irradiated power from $dW(\Omega) = \vec{S} \cdot d\Sigma\vec{u}_{\rm n}$ we found that the energy loss by the particle is:

$$\left(-\frac{dE}{dt}\right)_{\rm sync} = \frac{q^2}{6\pi\epsilon_0 c^3}\gamma^4\left(\gamma^2 a_{\parallel}^2 + a_{\perp}^2\right) \ , \tag{2.30}$$

where $a_{\parallel}$ and $a_{\perp}$ represent the acceleration which the electron undergoes when the magnetic field lines change while $\gamma^2 = 1/(1 - v^2/c^2)$ is the Lorentz factor, q is the charge, ϵ_0 the vacuum permittivity. The only force acting on the electron is the Lorentz force that can be expressed as:

$$\vec{F}_{\rm L} = \frac{d}{dt}\left(\gamma m\vec{v}\right) \equiv q\left(\vec{E} + \frac{1}{c}\vec{v} \times \vec{B}\right) \ , \tag{2.31}$$

$\vec{v}$ is the particle velocity. Since in the cluster medium the conductivity is very high, the electric field can be neglected and therefore:

$$\frac{d\vec{v}}{dt} = q\frac{\vec{v} \times \vec{B}}{\gamma mc} \equiv \omega_{\rm L}\left(\vec{v} \times \frac{\vec{B}}{B}\right) \ , \tag{2.32}$$

where ω_L is the Larmor frequency given by:

$$\omega_{\rm L} = 2\pi\nu = \frac{qB}{\gamma mc} = \frac{\Omega}{\gamma} \ , \tag{2.33}$$

where Ω is the non-relativistic gyrofrequency. We can define the Larmor radius is defined as the radius of the gyration:

$$\omega_{\rm L}\ r_{\rm L} = v_{\perp} = \beta\ c\ \sin\theta \ , \tag{2.34}$$

where $\beta = v/c$ is the relativistic beta factor while θ is the pitch angle between the the direction of the magnetic field and the particle velocity. The Larmor radius can be thus expressed as:

$$r_{\rm L} = \frac{\beta\gamma mc^2 \sin\theta}{qB} \ . \tag{2.35}$$

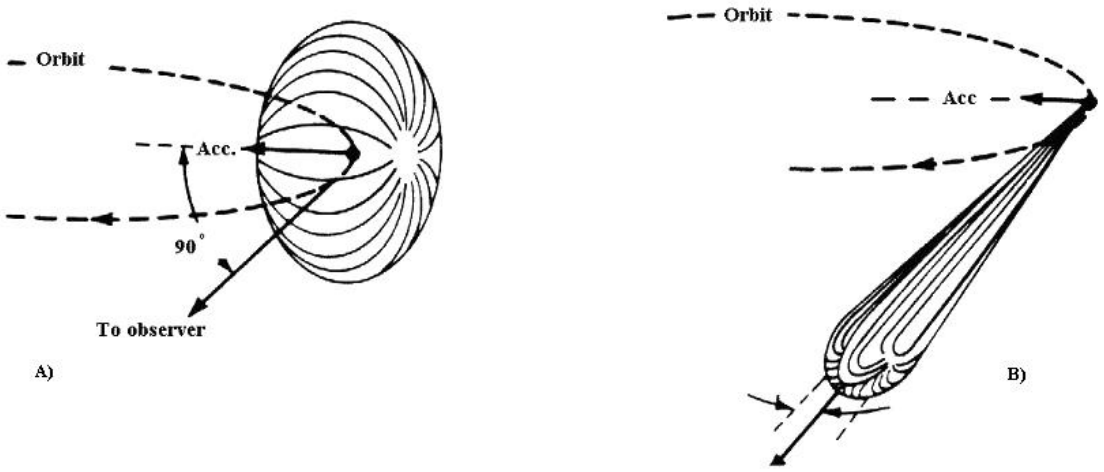

Figure 2.6: Scheme of the synchrotron radiation for a particle at low relativistic energy $\beta \sim 0$ (a) and at high relativistic energy $\beta \sim 1$ (B). It can be noticed that the solid angle of the radiation emitted decreases with the increasing speed. Credit: Wikipedia.

Now the perpendicular component of the acceleration acting on the particle can be computed from the Lorentz force as:

$$a_{\perp} = \frac{evB\sin\theta}{\gamma m_{\mathrm{e}}} \ , \tag{2.36}$$

so, since we neglect the electric field, the parallel component of the acceleration is zero and thus we can substitute the acceleration therm with Equation 2.36:

$$\left(-\frac{dE}{dt}\right)_{\mathrm{sync}} = \frac{\gamma^2 q^4 B^2}{6\pi\epsilon_0 c m_{\mathrm{e}}}\beta^2 \sin^2\theta \ , \tag{2.37}$$

considering the Thomson cross-section σ_{t} and $U_B = B^2/2\mu_0$ the energy density of the magnetic field. Averaging over all the angles $\langle\sin\theta\rangle = 1/2$ and considering ultra-relativistic particles ($\beta \sim 1$) we finally obtain:

$$\left(-\frac{dE}{dt}\right)_{\mathrm{sync}} = \frac{4}{3}\sigma_{\mathrm{t}} c U_{\mathrm{B}} \gamma^2 \ . \tag{2.38}$$

The energy lost by the electron is then $\propto B^2E^2$. From the power emitted by the particle, we can then compute the time that the particle need to lose all the energy:

$$\tau = \frac{E}{(dE/dt)_{\mathrm{sync}}} = \frac{\gamma m c^2}{4/3\sigma_{\mathrm{t}} c U_{\mathrm{B}} \gamma^2} \propto \frac{1}{\gamma B^2} \ . \tag{2.39}$$

2.6.3 Inverse Compton scattering

Already mentioned before, IC scattering that involves high energy electrons and CMB photons constitutes the main channel of energy loss for CRe. This effect is visible in the microwaves as a decrease in intensity, or a spectrum shift, of the CMB photons. This interaction is thought to produce an hard tail in the X-ray distribution.

The process is like the Compton scattering but in this cases is the photon that gains energy while electron is decelerated. The average energy gained from a single photon after a collision is $\sim \gamma^2 E$, where E is the initial electron energy, while the maximum energy that the photon can gain is $\approx \gamma m_e c^2$. Now, considering a relativistic electron swimming into a sea of photons, it will loose an amount of power that will depend on the scattering cross-section, namely the Thomson cross section σ_t, the electrons speed, the number density of photons with their energy distribution and the energy that each photon can gain after the scatter process with the electron. Then the loss, in the observer reference frame, will be:

$$P_{\rm IC} = \frac{4}{3}\sigma_t U_{\rm rad} c\beta^2\gamma^2 \propto U_{\rm rad} E^2 \ . \tag{2.40}$$

If we consider a high energy electron $\beta \sim 1$, it results as the synchrotron loss therm with the only difference of the radiation energy density $U_{\rm rad}$ instead of the magnetic field energy density U_B.

2.6.4 Brehmstrahlung

The brehmsstrahlung, or free-free emission is the radiation emitted by an electron transiting between unbound states in the field of a nucleus. The computation of relativistic and non relativistic brehmsstrahlung was carried out by Bethe & Heitler (1934) while the first astrophysical applications have been conduced by Koch & Motz (1959).
The calculation for the relativistic and non relativistic effects begins in the same way by the relativistic transformation of an inverse square law Coulomb field, namely we compute the electrostatic accelerations of the electron in its rest frame parallel and perpendicular to its direction of motion. Then, we obtain the Fourier transform of the acceleration components, the perpendicular and parallel ones, that will describe the radiation spectrum of the electron. It results that the main contribution to the emission of radiation comes from the momentum impulse perpendicular to the line of flight of the particle.
The result for the non relativistic brehmsstrahlung, in case of relativistic electrons, gives:

$$\left(-\frac{dE}{dt}\right)_{\rm brehm} = \frac{Z^2 e^6 N v}{24\pi^3 \epsilon_0^3 m_e c^3 \hbar} ln\left(\frac{b_{\rm min}}{b_{\rm max}}\right) \propto \frac{Z^2 N v}{m_e} \ , \tag{2.41}$$

where the ratio $b_{\rm min}/b_{\rm max} = ln(\Lambda)$ represents the Gaunt factor with b_{min} and b_{max} the maximum and minimum impact parameters, Z is the atomic number, and N is the density of nuclei. So, the energy loss depends mainly on the electron speed. For what concerns the thermal protons, their emission is negligible.
On the other hand, relativistic brehmsstrahlung losses come from the full derivation of Bethe & Heitler (1934), whose results is:

$$\left(-\frac{dE}{dt}\right)_{\rm brehm} = \frac{Z(Z+1.3) e^6 N}{16\pi^3 \epsilon_0^3 m_e^2 c^4 \hbar} E \left[ln\left(\frac{183}{Z^{1/3}}\right) + \frac{1}{8}\right] \propto \frac{Z^2 N E}{m_e^2} \ , \tag{2.42}$$

where now the energy loss depends on the initial energy of the electron, not its square, and also the protons emission is not negligible anymore.($\propto \gamma$).

2.6.5 Adiabatic losses

Electrons confined in an expanding volume are subject to adiabatic losses as they do work in order to reduce they internal energy, so each expansion or compression of the gas

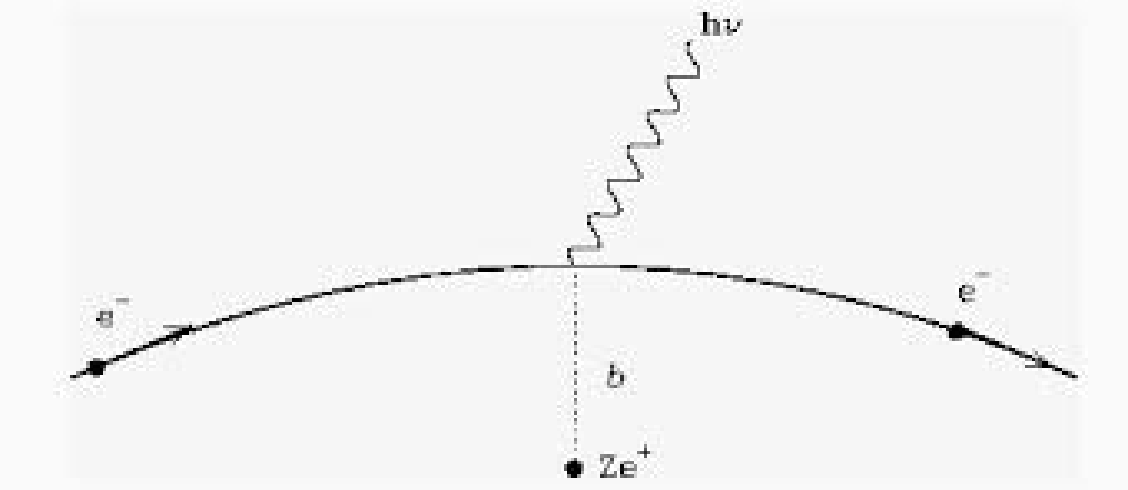

Figure 2.7: Brehmsstrahlung scheme that shows the trajectory of the electron and its emission. Credit: D. Dellacasa.

volume in which they are found will reduce or increase their energy following

$$dU = -pdV \ , \tag{2.43}$$

where p is the pressure of the gas, U its internal energy, and V its volume. For a perfect monoatomic gas we have:

$$U = \frac{3}{2}nkTV \text{ and } p = nkT \ , \tag{2.44}$$

with n the number density of the gas and T its temperature. Given an average energy of $\frac{3}{2}kT$, it is:

$$dU = nVdE = -\frac{2}{3}nEdV \ . \tag{2.45}$$

We can redefine $nV = N$, hence:

$$\frac{dE}{dt} = -\frac{2nE}{N}\frac{dV}{dt} \ . \tag{2.46}$$

Since dV/dt is the expansion rate of the volume V, if it expands at velocity $\vec{v}(r)$, then we can express the change of volume as a differential expansion of each pairs of faces of the cube

$$dV/dt = (v_{x+dx} - v_x)dydz + (v_{y+dy} - v_y)dxdz + (v_{z+dz} - v_z)dxdy \ . \tag{2.47}$$

After a Taylor expansion it results $dV/dt = 2/3(\nabla \cdot \vec{v})E$, the term can enter Equation 2.46 and therefore:

$$\frac{dE}{dt} = -\frac{2}{3}(\nabla \cdot \vec{v})E \ . \tag{2.48}$$

This is the general expression for the energy loss rate due to adiabatic losses of a non relativistic particle in an expanding flow.

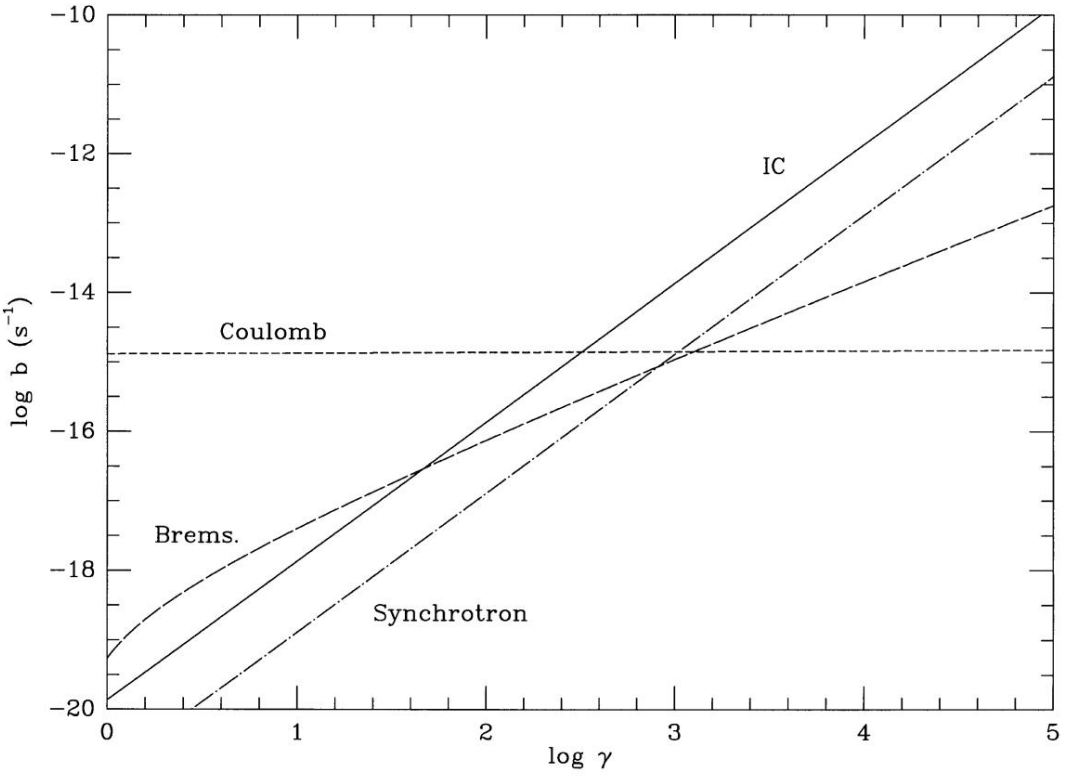

Figure 2.8: Values of the losses function $b(\gamma)$ for IC, Coulomb losses, synchrotron losses, and bremsstrahlung losses as functions of the Lorentz factor. The values assume $n_e = 10^{-3}\text{cm}^{-1}, B = 1\mu$ G, and $z = 0$. Credit: Sarazin (1999).

2.6.6 Diffusion loss equation

Because of random scattering due to irregularities in the magnetic field, either associated with turbulence or shocks or the different kind of motion that can vary the field in the environment, high energy particles diffuse from their sources through the medium. Therefore, this motion can be characterised by a diffusive coefficient D. As the particles diffuse, they can be subject to different kinds energy gains and losses such as those reported in the previous sections. It comes natural to try to describe the energy distribution for particles that undergo such processes, this can be done through the diffusion loss equation (Ginzburg & Syrovatskii, 1964) which is:

$$\frac{dE(E)}{dt} = \frac{d}{dE}\left[b(E)N(E)\right]Q(E,t) + D\nabla^2 N(E)\ , \tag{2.49}$$

that gives the time evolution of the energy spectrum of the particles. The term $b(E) = -dE/dt$ expresses the gains and losses of all the processes and $Q(E,t)$ is the particle injection rate per unit of volume.
Of particular interest, the $b(E)$ term can be described as the sum of the different contributions for gains and losses retrieved in the previous sections (see Figure 2.8 for a comparison between the different energy contribution at different energy values).

Chapter 3

Numerical results

In this chapter I will briefly introduce *ENZO* (an adaptive mesh refinement code for astrophysics used for the simulation, Bryan et al., 2014), Crater (a Lagrangian tracer code used to traces the gas dynamics and its properties, Wittor et al., 2016) and the scripts that I implemented to describe the evolution of radio emitting electrons. Moreover, due to the highly demanding computational cost needed to compute an accurate value of the magnetic field, I will be provide a complete explanation of the approach, tested by Brunetti & Vazza (2020), used to overcome the issue. In the second part I will provide a wide analysis of the tracer's physical evolution, closely connected with the case of the MHs.
Since my goal is to understand if the turbulent processes are capable of producing synchrotron radiation, the study of the Fermi I processes will be neglected for simplicity. A more comprehensive study of the spectrum, that involve numerical solution of the Fokker-Planck equation, is deferred to future works.

The results have been submitted as letter to Astronomy & Astrophysics (Beduzzi et al., 2023, , arXiv:2306.03764).

3.1 *ENZO* cosmological cosmological magnetohydrodynamics code

We simulated the evolution of a cluster of galaxy with *ENZO*, a highly parallel cosmological magnetohydrodynamic (MHD) code (Bryan et al., 2014). *ENZO* makes use of the Eulerian equation of ideal MHD, including gravity and taking into account the cosmological expansion, as follows:

$$\frac{\partial \rho}{\partial t} + \frac{1}{a}\nabla(\rho\vec{v}) = 0 \tag{3.1}$$

$$\frac{\partial \rho\vec{v}}{\partial t} + \frac{1}{a}\nabla\left(\rho v^2 + \vec{I}p^* - \frac{B^2}{a}\right) = -\frac{\dot{a}}{a}\rho\vec{V} - 1/a\rho\nabla\phi \ , \tag{3.2}$$

$$\frac{\partial E}{\partial t} + \frac{1}{a}\nabla\left[(E+p^*)\vec{v} - \frac{1}{a}\vec{B}(\vec{B}\vec{v})\right] = -\frac{\dot{a}}{a}\left(2E - \frac{B^2}{2a}\right) - \frac{\rho}{a}\vec{v}\nabla\phi - \Lambda + \Gamma + \frac{1}{a^2}\nabla\vec{F}_{\rm cond} \ , \tag{3.3}$$

$$\frac{\partial \vec{B}}{\partial t} - \frac{1}{a}\nabla\times(\vec{v}\times\vec{B}) = 0 \ , \tag{3.4}$$

where E is the comoving total fluid energy density, ρ is the comoving gas density, $\vec{B}$ the comoving magnetic field, and $\vec{v}$ the peculiar velocity. The term a is the cosmological expansion parameter and $\vec{I}$ is the identity matrix, while Λ and Γ are respectively the radiative cooling and heating functions. The $\vec{F}_{\text{cond}}$ term represents the thermal heat conduction (neglected in this work), p^* is the total comoving isotropic pressure, and finally ϕ is the gravitational potential.
The comoving total fluid energy density E is given by:

$$E = e + \frac{\rho v^2}{2} + \frac{B^2}{2a}, \tag{3.5}$$

with e being the comoving thermal energy density. In a MHD simulation p^* is defined as:

$$p^* = p + \frac{B^2}{2a}, \tag{3.6}$$

where p is the thermal pressure.The potential ϕ is expressed as:

$$\nabla^2\phi = \frac{4\pi G}{a}(\rho_{\text{total}} - \rho_0), \tag{3.7}$$

where $\rho_{\text{total}} = \rho_{\text{gas}} + \rho_{\text{DM}} + \rho_{\text{stars}}$ and ρ_0 is the mean density. The evolution of $a(t)$ is governed by the second Friedmann equation for the expansion of an isotropic and homogeneous Universe:

$$\frac{\ddot{a}}{a} = -\frac{4\pi G}{3a^3}\left(\rho_0 + \frac{3p_0}{c^2}\right) + \Lambda_c\frac{c^2}{3}\ . \tag{3.8}$$

In this equation ρ_0 represents the mean comoving mass density, including both baryonic and DM, p_0 is the comoving background pressure contribution, and Λ_{c} is the cosmological constant.
The dynamics of DM N-body particles are computed separately using Newton's law in comoving coordinates. The equation of motion are described by:

$$\frac{d\vec{x}}{dt} = \frac{1}{a}\vec{v} \tag{3.9}$$

$$\frac{d\vec{v}}{dt} = -\frac{\dot{a}}{a}\vec{v} - \frac{1}{a}\nabla\phi. \tag{3.10}$$

One of the main feature of *ENZO* is the adaptive mesh refinement (AMR), which allows for an increase in the number of cells whenever the evolution of the system requires more resolution. The simulation volume is divided in rectangular grids (also called root grid from which we can create subgrids), which become parent grids and generate child grids, where higher resolution is needed. The ratio between the parent and child cells was chosen to be an integer, usually 2 or 4. For what concerns the timestep, given a grid hierarchy (coarse, parent and child grids) at a given time t, the solutions are advanced with a W-cycle in a multigrid solver. The simulation computes the maximum timestep allowed by the coarser grids that will be advanced of the given timestep. Then, it moves to the lower level advancing all the grids, until they reach the coarser ones. In case there are more levels the procedure is repeated until all grids reach the same epoch.
In order to solve Equation 3.7, *ENZO* uses a fast Fourier technique (Hockney & Eastwood, 1988) on each grid at each timestep. Density is computed by taking into account collisioness matter, such as DM particles and stars. The N-body dynamics of the collisionless particles, which mass is fixed once initialised, is computed with a leapfrog scheme. Each particle will be associated with the highest refined level of a root grid, then particles are moved between grids as the hierarchy is rebuilt.

3.2 Lagrangian tracers

For this thesis project I analyse a cosmological, AMR *ENZO* simulation of a cluster of galaxies, using self gravity for ordinary and DM, radiative equilibrium cooling, and no other galaxy formation-related physics (e.g. star formation or feedback from supernovae). Magnetic fields are evolved assuming ideal MHD using the the hyperbolic cleaning method (see Domínguez-Fernández et al., 2019, for previous tests and results with a similar numerical setup). We started from simple uniform magnetic field seed of $B_0 = 0.4$ nG (comoving) in each direction at $z = 40$. In detail, the simulated cluster has a total (ordinary+dark) matter mass of $M_{100} = 3.8 \cdot 10^{14} \mathrm{M}_{\odot}$ and a virial radius of $R_{100} = 1.52$ Mpc at $z = 0$. It is the most massive object forming in a total volume of $(100\ \mathrm{Mpc}/h)^3$, sampled with a uniform root grid of 128^3 cells and DM particles (with an mass resolution of $m_{\mathrm{DM0}} = 3 \cdot 10^{10}\ \mathrm{M}_{\odot}$), and further refined with 4 additional levels of $\times 2$ refinement in spatial resolution each (and $\times 2^3$ refinement in mass resolution of the D; component, at each refinement step) with nested regions of decreasing size. The inner $(15.6\ \mathrm{Mpc})^3$ volume, where the cluster forms, is resolved with a maximum DM mass resolution of $m_{\mathrm{DM}} = 7.3 \cdot 10^6\ \mathrm{M}_{\odot}$ (i.e. $m_{\mathrm{DM0}}/8^4$), and with a uniform spatial resolution of 70 kpc/-cell. We also allowed for 2 extra levels of adaptive mesh refinement within this innermost region, to best model turbulence, by refining on local gas or DM overdensities, up to a final maximum resolution of $\approx 12.2 \sim \mathrm{kpc}/h = 18.0 \sim$ kpc (comoving). This resulted in central magnetic field values of $\sim 0.5 \sim \mu$G in the cluster center, which signals a too low amplification efficiency for the small-scale dynamo captured at this finite spatial resolution (e.g. Beresnyak & Miniati, 2016). In any case, we used for all our calculations a rescaled magnetic field intensity, to take into account the unresolved small-scale amplification, following Brunetti & Vazza (2020) (see also Secion 3.4).

The spatial evolution of the CRe potentially accelerated in this system was modelled in post-processing with a Lagrangian approach, i.e. by doing a Lagrangian sampling of the flow of matter across the Eulerian simulation and evolving the properties of the populations of CRe potentially associated with it. We did this using Crater a Lagrangian code used in Wittor et al. (2016). There were injected $\sim 10^5$ tracers at redshift $z = 1.94$ and their evolution was stopped at $z = 0.02$.

The Crater code generates a set of Lagrangian tracer particles and it advects them using the 3-dimensional velocity of the simulation, interpolated to their evolving 3-dimensional location. Moreover, an additional stochastic velocity term is introduced in order to better take into account the small effect of turbulent diffusion on the particle trajectories, as motivated in previous works Wittor et al. (2016). This last term takes into account the velocity of all the neighbouring cells, as well as the position-cell himself. So the small correction is computed as it follows:

$$\delta\vec{v}_{i,j,k} = \vec{v}_{i,j,k} - \frac{\sum_{i=0}^{2}\sum_{j=0}^{2}\sum_{k=0}^{2}\vec{v}_{i-1,j-1,k-1}}{27}. \tag{3.11}$$

The final velocity term assigned to each tracer is then given by:

$$\vec{v} = \vec{\tilde{v}} + \delta\vec{v}\ . \tag{3.12}$$

The compressive and solenoidal components of the velocity field are also computed, based on the value of divergence and the curl, because only the solenoidal velocity component of turbulence is used to estimate the Fermi II re-acceleration on electrons.

The solenoidal velocity component is:

$$v_{\rm sol} = \frac{1}{2}\sqrt{(dv_z - dv_y)^2 + (dv_x - dv_z)^2 + (dv_y - dv_x)^2}\ , \tag{3.13}$$

while the advective, or compression, term is computed as:

$$v_{\rm comp} = \frac{1}{2}\left(dv_x + dv_y + dv_z\right)\ . \tag{3.14}$$

Once that the fixed gas mass sampled by the tracer distribution is set ($\sim 10^8$ $M_\odot$), the number of tracers per cell is generated according to:

$$n_{\rm tracers} = \frac{m_{\rm cell}}{m_{\rm tracers}}\ , \tag{3.15}$$

where $m_{\rm cell}$ is the gas comoving mass. The tracer mass is entirely arbitrarily, but in general it has to be set small enough to properly resolve the formation of gas substructures in the simulation, as well as to correctly follow the low density accretion of matters at the cluster periphery. Moreover, after the beginning of the simulation, additional tracers with the same mass resolution are injected along the boundaries of the simulation, whenever new gas matter is accreted into the box, according to the prior equation.

All the particle snapshot data provided by the code were transferred on a `csv` file, making it more straightforward to be analysed with Python. After extracting all the data, I coded numerical functions for data analysis with plots, timescale functions, and electrons energy evolution. The timescale functions were based on Brunetti & Jones (2014), except for the turbulent re-acceleration timescale, which was taken from Brunetti & Vazza (2020). This newer and likely more realistic recipe is specifically tailored for the case under analysis, focusing on the Fermi II turbulent re-acceleration of electrons. In particular, this mechanism was shown to be a promising candidate to explain the production of diffuse radio emission at the periphery of clusters of galaxies (e.g Brunetti & Vazza, 2020; Bonafede et al., 2021; Botteon et al., 2022).

3.3 Loss and acceleration terms for cosmic ray electrons

Every generated Lagrangian tracer is treated as a whole family of CRe moving together with the gas matter, along the same trajectory generated by our tracer analysis. This is justified because: a) Larmor the gyroradius $r_{\rm g}$ of CRe in the range of energy of interest here ($\gamma = 10^2 - 10^5$), for typical $B \sim 0.1 - 10$ μG of the intracluster medium, is extremely small compared to the spatial resolution probed by the simulation, i.e. $r_{\rm g} \sim 10^{-9} - 10^{-5}$ pc $\ll 16$ kpc, hence we can safely assume that any CRe in the system will be advected with the thermal gas, while being attached to its tangled magnetic field and b) the effect of CRe diffusion of these electrons is characterized by timescales much longer than the evolutionary times of the simulation. The CR diffusion due to the turbulent motions not resolved by the simulation can be roughly quantified as $l_{\rm D} \sim 2\sqrt{D_{\rm turb,small} \cdot t}$, where the small-scale turbulent diffusion coefficient is $D_{\rm turb,small} \sim (V_{\rm turb,small}\Delta x)/3$ with Δx and $V_{\rm turb,small}$ being, respectively, the effective numerical resolution at the tracer location and turbulent velocity fluctuation within that scale. The typical rms turbulent velocity on these scales, based on the Kolmogorov model of turbulence and on the turbulence measured in the simulation, typically is $V_{\rm turb,small} \leq 5$ km s^{-1} for $\Delta x \leq 8 - 16$kpc, which

gives $l_{\rm D} \leq 0.01$ kpc over our typical timestep $\delta t \approx 32$ Myr, or ~ 2 kpc for the entire simulated evolution, i.e. a smaller diffusion scale than the scale of our simulated cells.

After the trajectories of tracers have been simulated and recorded, I computed the time scales for loss and gain processes which CRe should undergo, based on the evolution of the physical fields recorded by the tracers.

The electrons interaction with the gas, magnetic field, and ion can leads to energy loss. Those are well explained in Brunetti & Jones (2014). The amount of energy lost and processes involved strongly depend on the kinetic energy of the electrons. From now on, I will refer to the energy content of the CRe by using the Lorentz factor γ as representation of the energy content of the electrons, $E \approx \gamma mc^2$ (in relativistic approximation). The energetic loss at low γ are strongly dominated by the interactions of the electrons with the nuclei, that is, the bremsstrahlung and ionisation mechanisms are the ones that prevail. The energy variation for Coulomb losses is expressed through:

$$\left(\frac{dp}{dt}\right)_{\rm c} = -3.3 \cdot 10^{-29} n_{\rm th} \left[1 + \frac{ln(\gamma/n_{\rm th})}{75}\right] \tag{3.16}$$

where $n_{\rm th}$ is the thermal proton density in the medium in cm^{-3} and γ is the Lorentz factor. The other fundamental processes in a plasma are synchrotron and IC, whose energy loss therm can be expressed as:

$$\left(\frac{dp}{dt}\right)_{\rm rad} = -4.8 \cdot 10^{-4} p^2 \left[\left(\frac{B_{\mu\rm G}}{3.2}\right)^2 + (1+z)^4\right] \tag{3.17}$$

where, z is the redshift, $B_{\mu\rm G}$ is the ICM magnetic field in μG and where we assumed isotropic distribution of momenta with respect to the magnetic field. The term between the square brackets represents the magnetic field strength of the ICM, while the second is the equivalent magnetic field strength that an electron would experience by interacting with the background of CMB photons during an IC scattering process. It can also be expressed as $B_{\rm IC} = 3.2(1+z)^2$ μG. The inverse of the ratio between the loss in momenta and the momenta itself can give us a timescale needed for the CRe to completely exhaust its energy by means of that mechanism, $\tau \sim p/(dp/dt)$. We can finally sum up both the contributions and multiply the inverse for the momenta of the CRe:

$$\begin{aligned}\tau_{\rm e} \sim -4 \cdot \Bigg\{ & \frac{1}{3}\left(\frac{\gamma}{300}\right)\left[\left(\frac{B_{\mu\rm G}}{3.2}\right)^2 + (1+z)^4\right] + \\ & \left(\frac{n_{\rm th}/10^{-3}}{\gamma/300}\right)\left[1.2 + \frac{1}{75} ln\left(\frac{\gamma/300}{n_{\rm th}/10^{-3}}\right)\right]\Bigg\}^{-1} \ {\rm Gyr} \ .\end{aligned} \tag{3.18}$$

One other process that affect the electrons energy is the gas adiabatic compression, or expansion, that can add or subtract energy to the particles. The resulting "advection" timescale is:

$$\tau_{\rm adv} = \frac{0.951}{\nabla \cdot \vec{v}/10^{16}} \ {\rm Gyr} \ . \tag{3.19}$$

The last effect to take into account for the energy contribution is the turbulent re-acceleration. This is due to Fermi II effect that can make the CRe gain energy each time they interact with a turbulent eddy. In fact, solenoidal turbulence can re-accelerate particles via stochastic interaction with diffusing magnetic field lines in super-Alfvénic

turbulence, as outlined by Brunetti & Lazarian (2016a). The re-acceleration timescale depends on the diffusion coefficient and not on the particle momentum $\tau_{\rm acc} = P^2/D_{\rm pp}$. As shown in Vazza et al. (2021), the timescale value can be expressed as:

$$\tau_{\rm acc} = 1.25 \cdot 10^2 \frac{L/0.5\ B_{\mu\rm G}}{\sqrt{n_{\rm th}/10^{-3}}(\delta V/10^7)^3} \quad \text{Gyr} \tag{3.20}$$

Where $n_{\rm th}$ is the proton thermal density, $B_{\mu\rm G}$ is the magnetic field magnitude expressed in μG, L is the length scale of the perturbation and δV is the turbulent velocity. To retrieve this last quantity is essential to understand the key role of the Kolmogorov theory. We know that the turbulence over a certain length-scale and time-scale, conserve its energy. So it is possible, knowing those two values, to compute the turbulent velocity, $v_{\rm L}$. The time-scale $\tau_{\rm L}$ value, or eddy turnover time, can be obtained from the solenoidal component of the gas velocity, also called vorticity $1/\tau_{\rm L} \sim |\omega_{\rm L}| = |\nabla \times \vec{v}|$. Since the length-scale over which the vorticity is compute is exactly $L = 54\ kpc$ (three times the cell size), the eddy velocity result $\delta V_{\rm L} \sim L/\tau_{\rm L} \sim L \cdot |\omega_{\rm L}|$.

Once the timescales are compared, it is possible to predict the spectral evolution of the tracers using the Fokker-Planck equation, and obtaining the electron spectra at any given time. I did not solve the equation numerically since it is computationally very expensive, as it would require attaching additional $\sim 10^2$ energy bins energy to each tracer, which would make the simulation too demanding for the given computational resources.

In a complementary approach, I sampled the time evolution of a few reference initial values of CR energies, by numerically integrating:

$$\gamma_{t_i} = \int_{t_{i-1}}^{t_i} \dot{\gamma}\ dt$$
$$\gamma_{t_i} \approx \gamma_{i-1} + \dot{\gamma} \cdot (t_i - t_{i-1}) \tag{3.21}$$

in which the time derivatives of the γ energy are evolved as in Vazza et al. (2021):

$$\dot{\gamma} \approx \left|\frac{\gamma}{\tau_{\rm rad}}\right| + \left|\frac{\gamma}{\tau_{\rm c}}\right| + \frac{\gamma}{\tau_{\rm adv}} - \left|\frac{\gamma}{\tau_{\rm acc}}\right| \ . \tag{3.22}$$

This way, I can accurately study the minimum γ reached by CRe during their evolution and accretion onto the forming cluster of galaxies, and assess which are the plausible chances for a given mechanism to fill the intra-cluster medium with a reservoir of CRe up to a given energy. On the other hand, this approach is not suitable to accurately predict the energy spectrum of the full evolving population of CRe, as this would require to evolve the entire wide range of energy bins (in which case a more expensive direct Fokker-Planck method would be optimal).

Before beginning the analysis, it is necessary to convert redshift to lookback time. This was achieved by assuming a flat ΛCDM model with $H_0 = 67.8$ km s^{-1} Mpc^{-1} and $\Omega_M = 0.308$, and by using the `FlatLambdaCDM` package[1] from the `Astropy` library[2]. However, since I started the analysis at $z = 1.94$, i.e. soon before the sequence of mergers that formed the bulk of the cluster mass, in the remainder of the thesis I will start computing ages starting from the epoch of $t = 3.4$ Gyr, corresponding to $z = 1.94$.

[1] https://docs.astropy.org/en/stable/api/astropy.cosmology.FlatLambdaCDM.html
[2] https://docs.astropy.org/en/stable/index.html

3.4 Magnetic field

The magnetic field plays a crucial role in the context of this thesis. Its presence is responsible for the synchrotron radio emission, and any miscalculations or incorrect hypotheses regarding the magnetic field could significantly impact the outcomes of this work. A comprehensive review of magnetic fields in plasma, specifically in the context of galaxy clusters, has been provided by Donnert et al. (2018).

The plasma is often subject to turbulent motions that are able to stretch, twist, and fold the magnetic field lines. This results in an increase of the magnetic energy content, which leads to an amplification of the field. This phenomenon, also known as small-scale dynamo, occurs at the Alfvén scale. The amplification has a physical limit that depends on the efficiency of the eddies to bend the magnetic field lines, which can be viewed as the efficiency in energy transmission.

To observe direct dynamo amplification in simulations, it is necessary to resolve the Alfvén scale $\ell_{\rm A}$, beyond which the magnetic field reacts to the increase in field energy density. However, this task is particularly challenging in galaxy cluster simulations, where the smallest resolution is often coarser than the local Alfvén scale. Vazza et al. (2017) presented initial insights into the relationship between simulation resolution and field amplification. They reported different simulations with varying cell-scales, and the magnetic field intensities obtained at the end of the simulations are shown in Figure 3.1. It is evident, from that figure, that the smoothness of the field at low spatial resolution cannot reproduce the realistic values of the field magnitude. Furthermore, Figure 3.2 illustrates that only when the resolution is around ~ 4 kpc, the mean value of $\ell_{\rm A}$ is well sampled. This imposes a constrain on simulations, often requiring alternative methods to address the magnetic field amplification due to the impossibility of increasing the resolution. Alternatively, the amplified field value can be estimated a posteriori by assuming that a portion of the turbulent energy is converted into magnetic field amplification, as explained earlier. Therefore, by knowing the efficiency of the transmission mechanisms and the turbulent velocity of the eddies (which provides the energy content, see Equation 2.26), an upper limit of the magnetic field strength can be constrained. Once the kinetic energy flux across the turbulent cascade $\epsilon_{\rm s}$ is known for each cell, the magnetic field amplification can be reconstructed using the equation provided by Beresnyak & Miniati (2016):

$$B_{\rm turb} = \left(8\pi \int_{t_{i-1}}^{t_i} C_E \epsilon_{\rm s} \, dt \right)^{1/2} , \tag{3.23}$$

where the difference between t_i and t_{i-1} corresponds to a simulation timestep, and C_E is the efficiency of energy dissipation between turbulent energy and magnetic field energy. $C_{\rm E}$ is a quantity computed in the simulation, and its expected value is around $0.03-0.04$ as reported in recent works by Vazza et al. (2017) and Brunetti & Vazza (2020). Compressive flow is taken into account for the total amount of energy. Therefore, I estimated in post-processing the maximum value of magnetic field amplification. This approximation, introduced by Beresnyak (2012), provides us an upper limit to the magnetic field strength, which translates in a lower limit for the energy content of the CRe, since the Fermi II model affirms that they depend on the inverse value of B. The value of the amplified magnetic field is provided by Brunetti & Vazza (2020):

$$B_{\rm turb} \sim \frac{1}{2} \eta_B \rho_{\rm ICM} \delta V^2 , \tag{3.24}$$

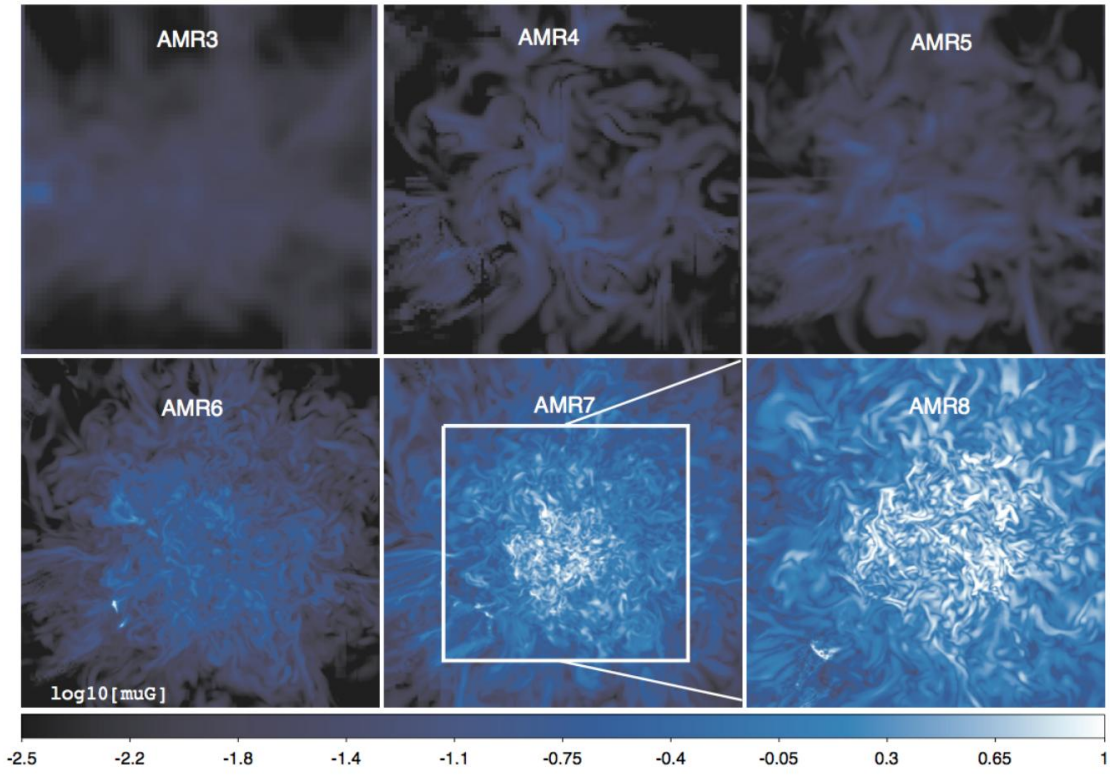

Figure 3.1: The different AMR, represent six different simulations with the same initial conditions. The best resolutions $\Delta x_{\max}$ achieved during the simulation in the innermost region are: 126.4, 63.2, 31.6, 15.8, 7.9, and 3.95 kpc, respectively, and the initial magnetic field strength is about $B_0 = 0.1$ nG. Credit: Vazza et al. (2017).

where $\eta_B = C_E$, $\rho_{\rm ICM}$ is the density of the ICM, and δV^2 is the square of the eddy velocity dispersion. This value represents the B value that I will use for calculating the acceleration and loss timescales of relativistic electrons. Despite that, it is possible that due to low turbulence, the magnetic field computed in the simulation results higher than the amplified one. Therefore, I will chose the greater between the two values at each timestep.

3.5 Break frequency

Although in this procedure I cannot predict the exact synchrotron emission provided by the Fokker-Planck equations, I was able to obtain a realistic estimate for the frequency of synchrotron emission by combining the magnetic field and energy values. The numerical calculation of the Fokker-Planck equation is computationally too demanding, therefore, the method that I will introduce in this section represents the most accurate alternative.

In the turbulent re-acceleration scenario, there is a critical Lorentz factor $\gamma_{\rm c}$ at which the total cooling timescale $\tau_{\rm cool}$ becomes comparable to the acceleration timescale $\tau_{\rm acc}$. Correspondingly, the emission radio spectrum will steepen at a frequency $\nu_{\rm c} = \xi\nu_{\rm b}$, where $\nu_{\rm b}$ is the break frequency and $\xi \sim 6 - 8$ (Figure 3.3). The former can be estimated from the maximum value of the Lorentz factor of the electrons associated with each tracer, its

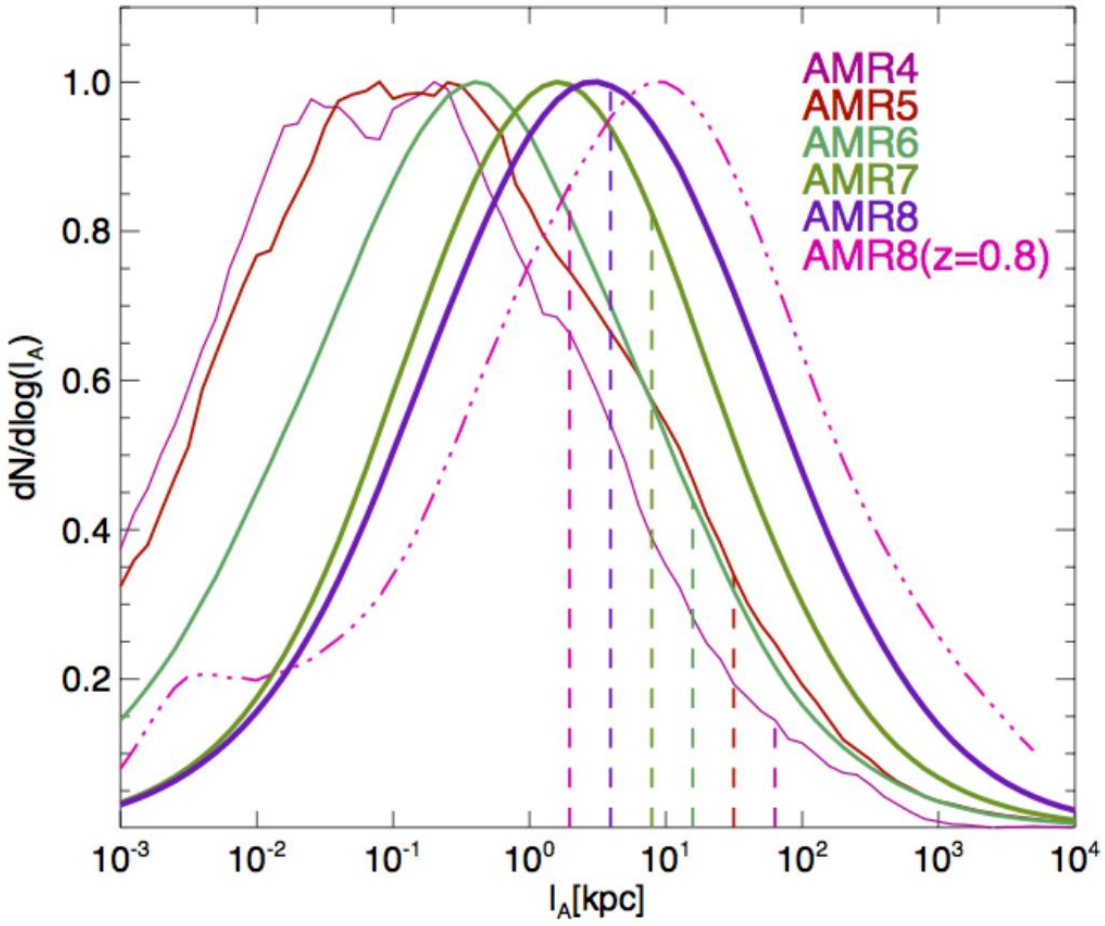

Figure 3.2: Each curve gives the scale distribution of the Alfvén scale, $\ell_{\rm A}$, measured in the simulated ICM, while the vertical lines represent the lower limit at which the $\ell_{\rm A}$ can be resolved. The values are taken at $z = 0$ for each simulation. Credit: Vazza et al. (2017).

value is (Cassano et al., 2010):

$$\nu_{\rm b} \approx 4.6 \langle\gamma\rangle^2 \cdot \frac{\langle B \rangle}{\mu{\rm G}} \ \ {\rm Hz} \ . \tag{3.25}$$

This allows us to translate the $\gamma(t)$ measured onboard of our tracers as a function of time into an estimate of the maximum observable synchrotron emission frequency.

3.6 Single tracer analysis

First, I shall use the propagation history of a single Lagrangian tracer to introduce the analysis routines applied to the entire population of Lagrangian tracers. This allowed me to test the relation between loss and gain terms against the gradual or sudden changes of physical parameters, experienced by the single tracer along its accretion sequence onto the main cluster. The choice of the tracer has been done by selecting the particle that

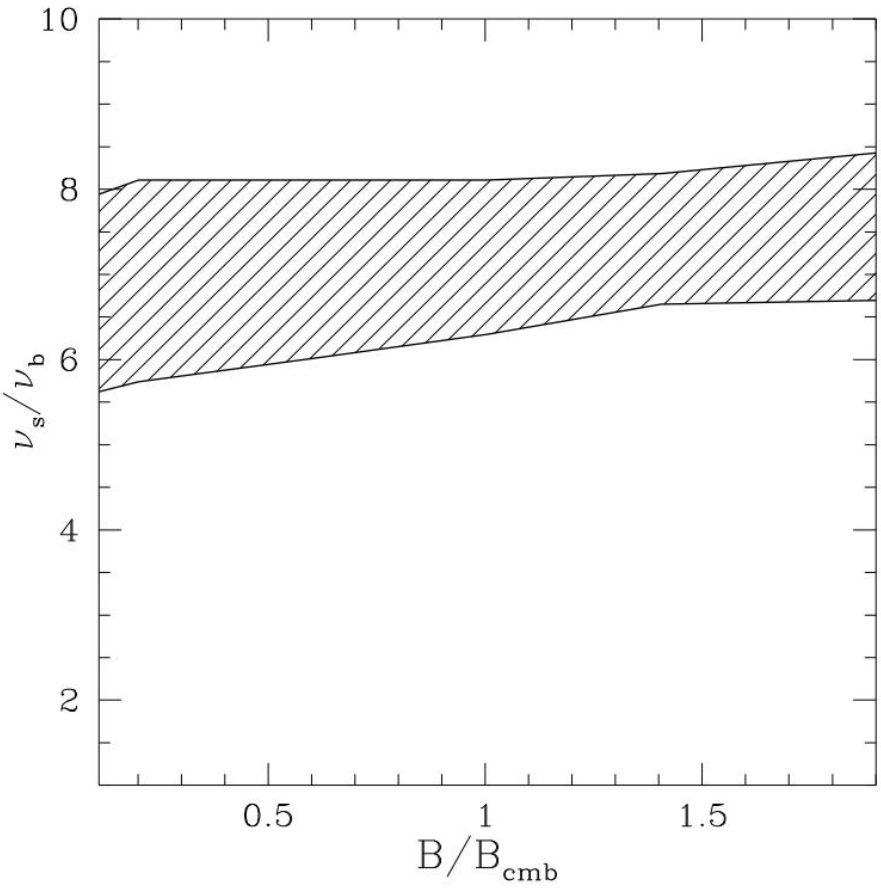

Figure 3.3: Relation between ν_b and ν_s versus B field from a sample of simulations. Credit: Cassano et al. (2010).

was found in the hottest region at redshift zero. This will help me to constrain the typical conditions of the region that passes through the major mergers of the simulation. We can expect that the maximum temperature can be related to the innermost region of the final cluster, where the gas accreted in the initial phases of the simulation from the most massive object is located. Having a tracer ending up in the centre of cluster, and having undergone surely through the most violent accretions of matter in the past, will help us understand if, at least in this case, the observed gas dynamics can be potentially compatible with the formation scenarios of halos and mega-halos.

The main mergers involving the tracer happen at ages $\sim$ {4.5, 7.9, 8.8, 9.6, 11.1, 12.4} Gyr. We can seen in Figure 3.4, that during the early phase of the simulation the tracer is found in a very massive filament (the initial tracers distribution follow the gas mass one). The tracer evolves through a large number of accretion events (seen through the multiple sudden increases in the gas density and gas temperature in Figure 3.5). As seen in Figure 3.4 the cluster, which the particle belongs to, corresponds to the region of space with higher gas density. The tracer records the values of every field at each numerical timestep of the simulation, as shown in Figure 3.5. All fields are in physical units, and not comoving, as all the equations of Section 3.3 require. The tracer trajectory follows the one of the massive filament in the field, which gets accreted onto the massive cluster

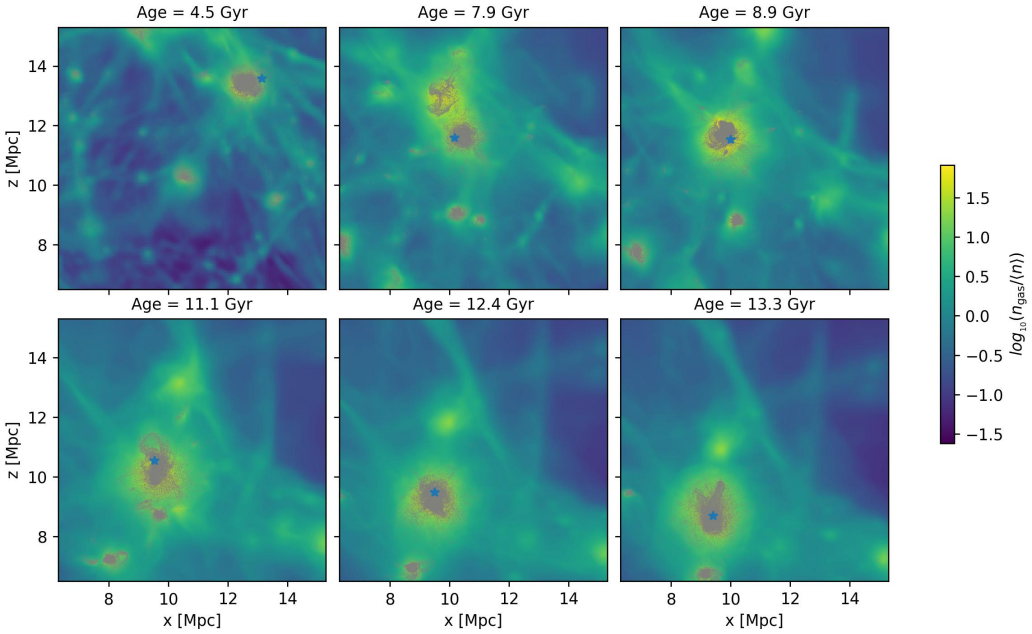

Figure 3.4: Position of the tracer in the cluster at different epochs. The tracer is represented by the blue star. Each cell scales 18 kpc. The length along the x axis is 7.38 Mpc while is 6.48 Mpc in z direction.

at the center of the simulated volume. The magnetic field produced in the simulation is of the order of 10^{-1} μG, and it never exceeds 0.5 μG. It can be noticed that it presents different peaks along the time sequence, these correspond at the times of merges that cluster, to which the tracer belongs, experiences. We can see the sharp jumps of the fields related to merger events, i.e. in temperature, vorticity ($\nabla \times \vec{v}$), or density. It can also be noticed that, the density and the temperature increase during the final phases of the evolution due to the transit of the particle around to the very center of the cluster, which keeps increasing its mass by accreting new infalling satellites. The Lagrangian history of this tracer highlights all the main phases of the formation of a typical cluster of galaxies. Before moving to the timescales evaluation phase it is crucial to study the amplification of the magnetic field due to the solenoidal turbulence in the ICM, via small-scale dynamo explained in Section 3.4. As Figure 3.6 shows, the field amplification is not negligible. Moreover, while at almost every epochs the estimate of the amplified magnetic field is larger then the one computed in the simulation, the latter can be larger following violent episodes of gas compression and turbulence dissipation, followed by the cluster dynamical relaxation. Therefore, for every timestep, the maximum of the two magnetic field estimates is considered both for loss and re-acceleration timescales.

It is useful, in order to understand the behaviour of the simulated family of electrons, to visualise the timescales of the Coulomb and radiative losses at different energy levels. This has been done for $\gamma = \{10^2,\ 10^3,\ 10^4\}$ (Figure 3.7). Those timescales are comparable in the case of $\gamma = 10^2$, after ~ 8 Gyr with the Coulomb losses that became completely dominant after ~ 10 Gyr. Already at $\gamma = 10^3$, the radiative losses have shorter timescales and the bremsstrahlung losses become comparable only at the end of the evolution, when the timescales decreases to the same order of magnitude. For what concerns the loss at

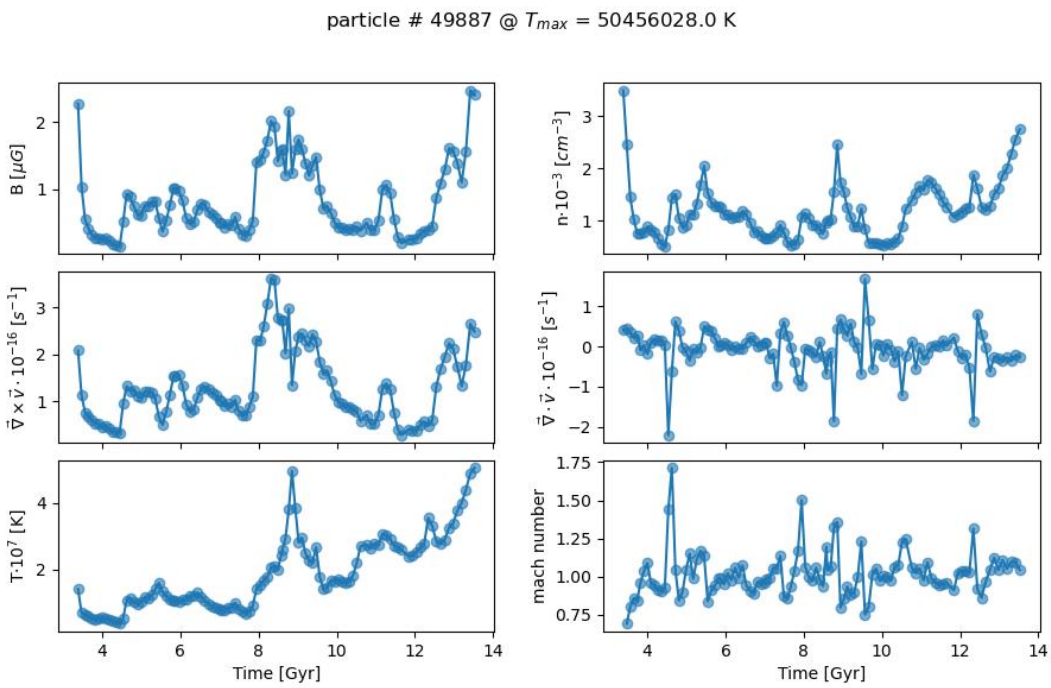

Figure 3.5: Representation of the fields with respect to the age of the Universe. All the quantities are represented with their physical and not comoving values.

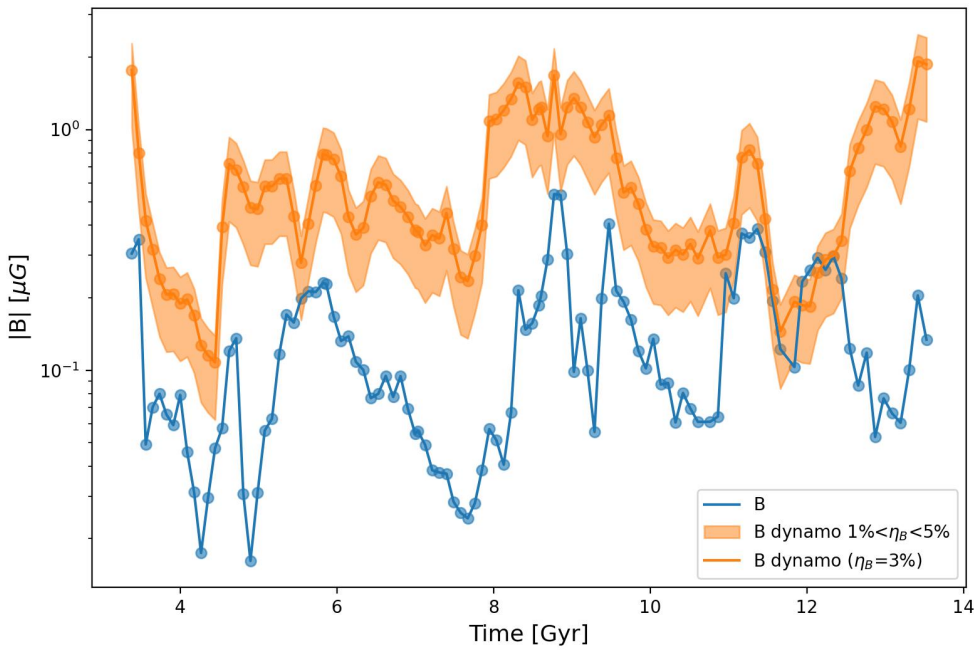

Figure 3.6: Time evolution of the magnetic fields recorded by the tracer. The orange line refer to the magnetic field produced by the small-scale dynamo with an efficiency factor of $C_E = 3\%$ while the blue one is computed by the MHD simulation.

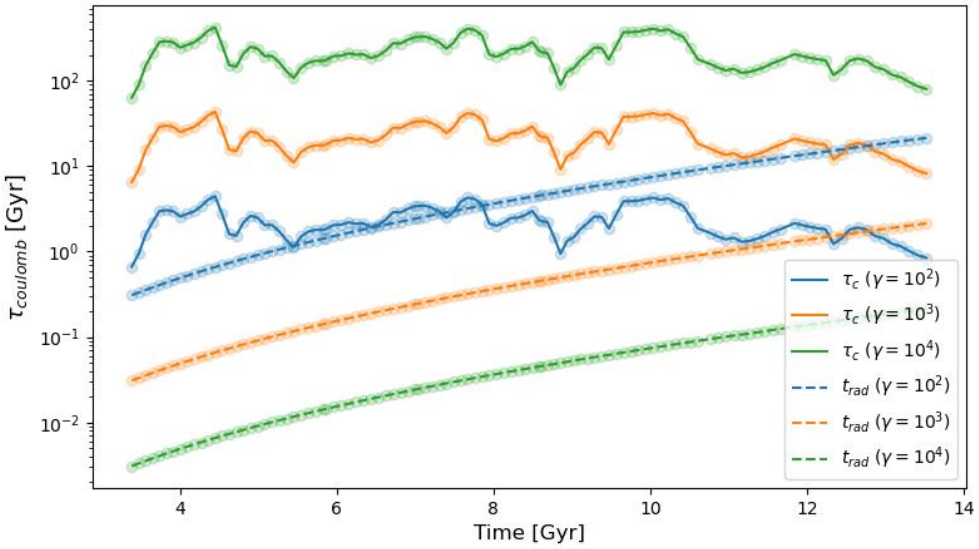

Figure 3.7: Timescales of the Coulomb losses and radiative (synchrotron and IC) losses. It is interesting to notice that τ_c can be lower than τ_{rad} at $\gamma = 10^2$ after 8 Gyr. This is due to an increasing density field in the final phase of the simulation.

$\gamma = 10^4$, there are no comparison between the two timescales and energy losses for IC and synchrotron became dominant It can also be seen that the behaviour of τ_c is almost always due to the contribution of the IC processes, and the losses from synchrotron emission are subdominant.
The comparison of timescales, reported in Section 3.3, gives us an idea of the evolution of relativistic electrons sampled by tracers at different ages. In Figure 3.8 all the losses experienced by the particle are displayed together. The loss timescale which comprises synchrotron, IC, bremsstrahlung, and Coulomb processes, has been defined as τ_e (Equation 3.18), turbulent re-acceleration timescale is defined as τ_{acc} (Equation 3.20), while the advection timescale is reported as τ_{adv} (Equation 3.19, but only positive, namely compressive, contribution are reported in Figure 3.8). The figure shows that the radiative processes are the most efficient mechanism at $\gamma = 10^4$ while at lower energy ($\gamma = 10^2$) Coulombian losses are instead predominant at all times. The turbulent re-acceleration timescale, τ_{acc}, decreases during the merger phases, due to the increase of the turbulent velocity, and in particular of the solenoidal one. The last accretion of the cluster at ~ 12.4 Gyr is highlighted by the sudden decrease of τ_{acc} that became lower than τ_e for $\gamma = 10^4$ due to the increase the vorticity and the decrease of the magnetic field. With regard to τ_{adv}, its timescale is always larger than the other, so we can neglect its contribution compared to the effect of re-acceleration. Finally, as can be noticed from the plot the tracer can spend a long time losing energy before being re-accelerated. If the electrons energy reaches $\gamma \sim 10$, the CRe looses all its energy via Coulomb collisions.
The global picture that we can extract from the plot is that it is possible to have time re-acceleration timescales shorter than energy loss ones, at least for a typical Lagrangian tracer accreted into the innermost region of this simulated cluster. The re-acceleration efficiency can push relativistic electrons to higher energies allowing them to be radio-

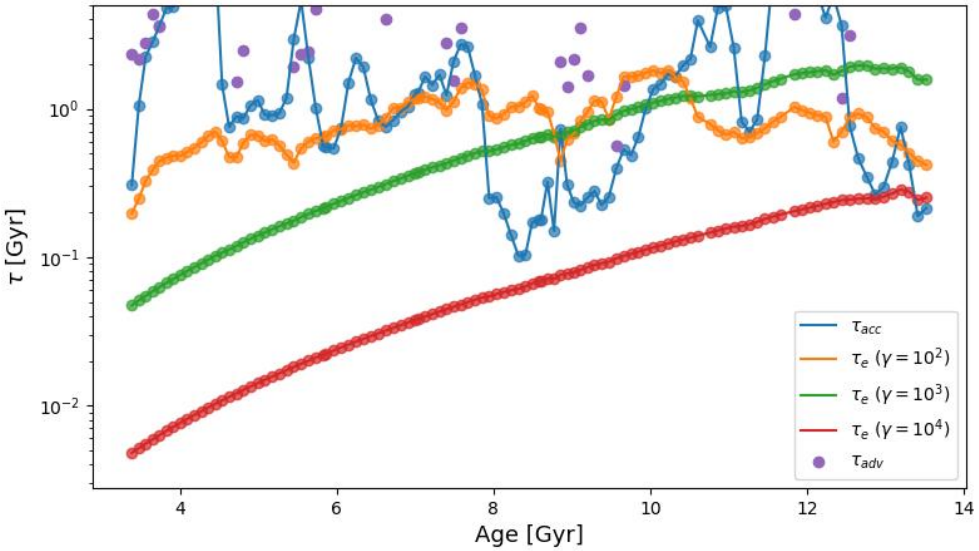

Figure 3.8: Timescales of the losses and re-acceleration processes. It can be seen that $\tau_{\rm acc}$ became relevant after ~ 8 Gyr and can sustain the re-acceleration up to $\gamma > 10^3$ in different moments of the evolution. It is also interesting to notice that at ~ 10 Gyr the radiative losses become so relevant that τ_c for $\gamma = 10^2$ is more efficient than the one for $\gamma = 10^3$, that are dominated by radiative processes.

emitting. It is also evident that re-acceleration processes required, as expected, significant matter accretion events capable of sustaining a high level of gas vorticity across the cluster volume. This scenario is in agreement with the classical picture of the RHs formation in galaxy clusters.

The energy evolution of the electron is shown in Figure 3.9, where I assumed that all cosmic electrons were first injected at $t = 8$ Gyr (close in time with the formation of the cluster) though minor satellites accretions. We can see that the particle gains energy since its injection, due to the increase in vorticity that results into Fermi II re-acceleration. As expected, the acceleration of the particle correlates with the most important merger events along the time sequence. Moreover, the overall trend of the energy corresponds to that of the vorticity, which proves to be capable of keeping our relativistic electron energetic for a sufficiently long time. It is also interesting to notice that there are peaks corresponding to those of temperature and density, which is also an indication that the particle is passing through regions that are being accreted with matter from the infalling satellites, which we know are often leading to supersonic or transonic motions, and hence shock waves. In summary, my Lagrangian evolution of a single gas tracer, ending up in the cluster region where RHs should form appears to be indeed, in our analysis, compatible with the re-acceleration of a significant amount of high energy electrons, potentially radio emitting at LOFAR frequencies.

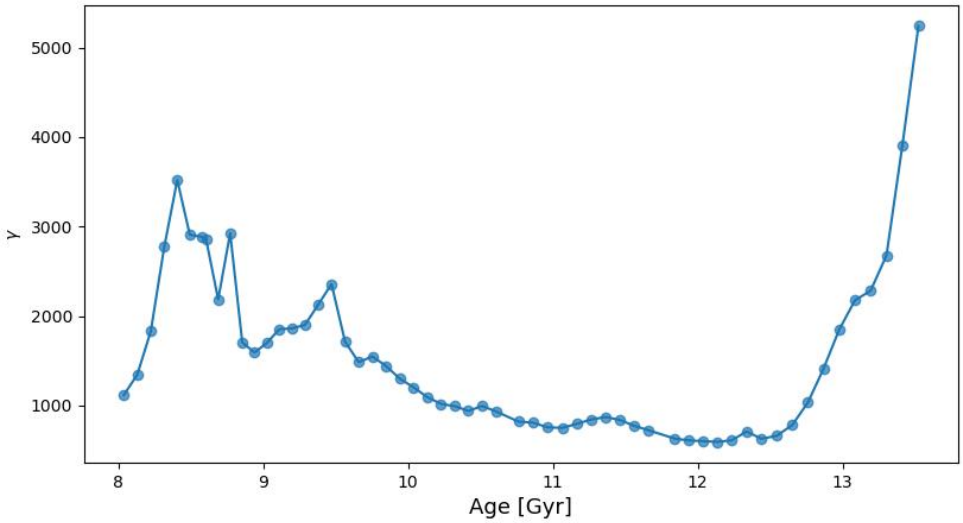

Figure 3.9: Energy evolution of the CRe in time with vorticity, number density, and temperature evolution. present in the tracer can be re-accelerated to energies higher than the injection energy. These energies are in agreement with those observed, validating the model used.

3.7 Analysis of different families of tracers

The following sections will be devoted to the analysis of the evolution of the different tracers families which form the cluster of galaxies at $z = 0$. Therefore, we need to identify suitable populations of tracers. I selected two different components: the RH, where we expect to find X-ray and radio emissions in a region between the center and $0.4R_{500}$; the MH component, with the diffuse radio emission that can fill all the region between the RH and R_{500}. I made the choice following the results obtained in Cuciti et al. (2022) where it was found an MHs extension between $0.4R_{500}$ and R_{500}. Once found the particles of interest the analysis will develop as for the single tracer, but in this case only the median values of the distribution will be shown.

3.7.1 Tracers filling the entire cluster

In the initial phase of the simulation, the particles are disposed in filaments as can be noticed in Figure 3.4. A large fraction of the gas remains spread until ~ 8 Gyr, when the cluster begins to form trough satellites mergers, the collision then stops at ~ 12 Gyr. The last merger, at ~ 12 Gyr, pulls a large fraction of gas away from the center of the cluster, forming a lobe that extends until the virial radius. During the last Gyr of evolution, the cluster experiences a phase without collision. The peculiarity of the case is that with no mergers turbulence will not develop and, since the MHs were only observed in clusters with evidences of at least a major merger, the analysis will tell us what we can expect even in more relaxed situation.
Since the goal of this thesis is study the evolution of the cluster, I will consider only the phases after 8 Gyr. The same logic will be applied also for the CRe injection because, as

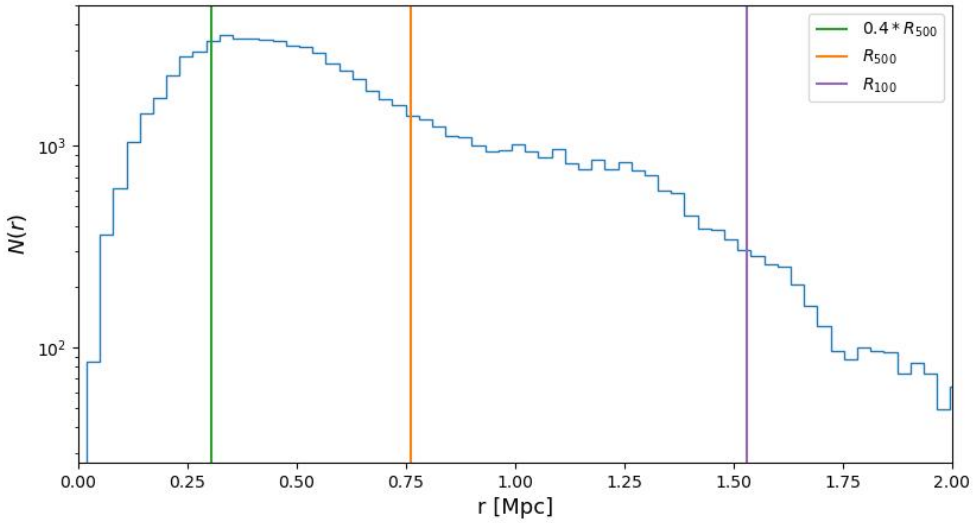

Figure 3.10: Radial distribution of tracers at 13.5 Gyr. The vertical lines represent the different values of virial radii. Between the center and green lines, we find the RH of the cluster. Between the green and the orange lines, we found the MH region, while within the purple line we have the whole virialised system.

we will see, the tracers injected before give only a little contribution on the total content of energy of the whole electrons population. The selection of the particles was based on the spatial distribution of the tracers at the end of the simulation.

In order to retrieve the position of the center of gas mass, I selected the median position out of all the tracers, then the radial distances from the median position were derived, and I selected all those that were found within a radius of less than 2 Mpc. The center of mass is finally found by computing the mean value of the position. Since all the tracers have the same mass, the mean value is exactly the value of the physical center of mass.
The first component, the RH, is within $0.4R_{500} = 0.30$ Mpc. The second region, the MH region, is the one found between $0.4R_{500} = 0.30$ Mpc and $R_{500} = 0.76$ Mpc. The last part can be of particular interest since we can see if the electron in the outskirt can be conserved without thermlise or if they lost all the energy and became undetectable.

3.7.2 Tracers filling the classical radio halo

The family of tracers, that will form the inner part of the cluster, is initially homogeneously distributed into filaments filling the vast majority of the simulated volume. These tracers experience accretion phases consistent with those reported in the single tracer analysis, involving the same number of mergers (the pre-merger phases are represented in Figure 3.20). The plots in Figure 3.11 show that after an initial phase in which the tracers underwent minor accretion processes, the vast majority of those particles cluster to form the major halo at ∼8 Gyr. At this epoch, the median Mach number shows a very strong increase, and the same happens for the adiabatic compression value, followed by an increase in all the other fields. In the phase between 8 Gyr and 11 Gyr, the vast

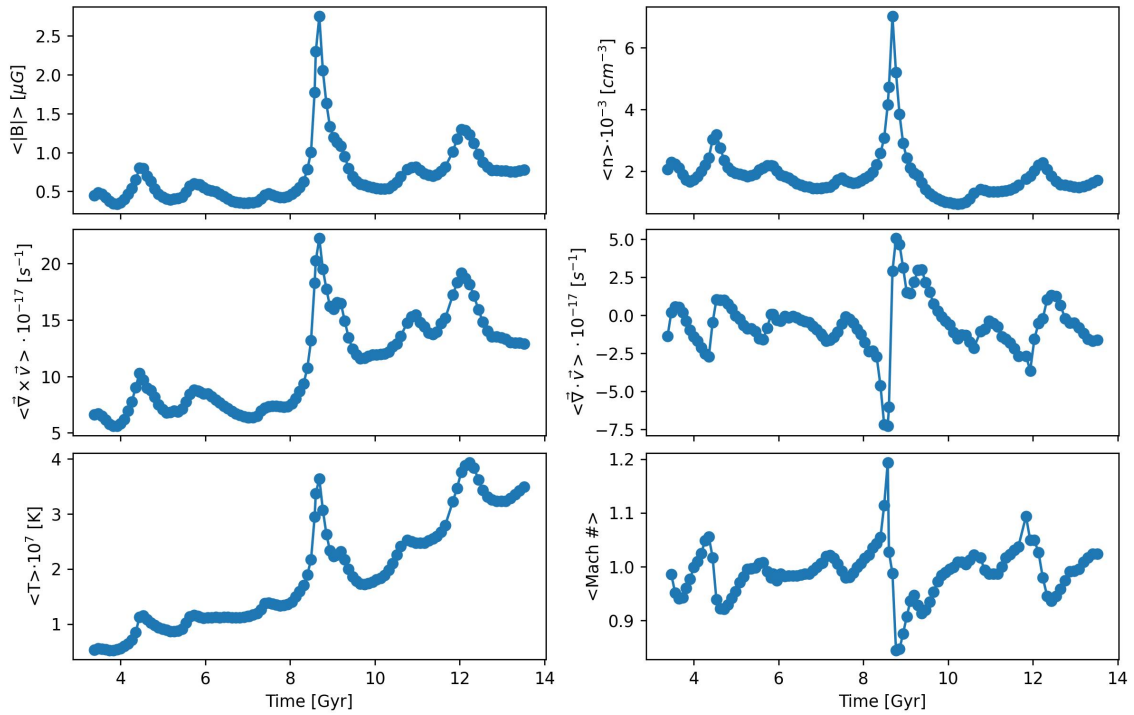

Figure 3.11: Time evolution of the median values of the fields for the RH tracers.

majority of tracers fill the cluster and the satellites. During this epoch, the cluster is dynamically active and, it can be seen from the median value of the divergence, the compression remains dominant due to the entrance of some small satellites. Then, at 11 Gyr, a massive satellite collides with the cluster and, a fraction of the tracers, that are in the satellite, falls in the center of the cluster while a smaller portion is dispersed in the outer regions. The satellite can be seen in Figure 3.20, at 8.9 Gyr in position (x, z) ∼(10,9) Mpc, and it reaches the center of the cluster at 11.8 Gyr. This event increases all the median values of the parameters since a fraction of the tracers, that fills the satellite, falls in the cluster center after the collision between the two. The median field values of temperature, vorticity, and magnetic field rise for half a Gyr, and then it begins a relaxation phase where the cluster does not undergo further mergers. This is highlighted by the decrease of both the magnetic field and vorticity. Moreover, the temperature shows an increase because eventually, a large fraction of the tracers locate in the very center.

Figure 3.12 shows the median timescales of the tracers at different ages. The first parts of the evolution, until ∼ 8 Gyr, are dominated by radiative losses. Then, after the merger phase, $\tau_{\rm acc}$ becomes comparable to the other timescales due to the strong increase in vorticity injected from all filaments. Additionally, the timescale for energy losses at low energy, $\gamma_{\rm inj} = 10^2$, becomes comparable to the timescale for energy loss at $\gamma_{\rm inj} = 10^3$. As expected, the Coulomb processes remain the most relevant at low energy, while at higher energy values, IC processes continue to be predominant over synchrotron emissions. The advection timescale experiences a strong decrease due to compression of the ICM after 8 Gyr, but it never reaches the other median timescales. After the merger, $\tau_{\rm acc}$ becomes comparable to low-energy losses, and after 10 Gyr, it becomes low enough to support high-energy re-acceleration. It is also interesting to notice that low-energy electrons experience very fast energy losses. As expected, matter accretion plays a fundamental role in the

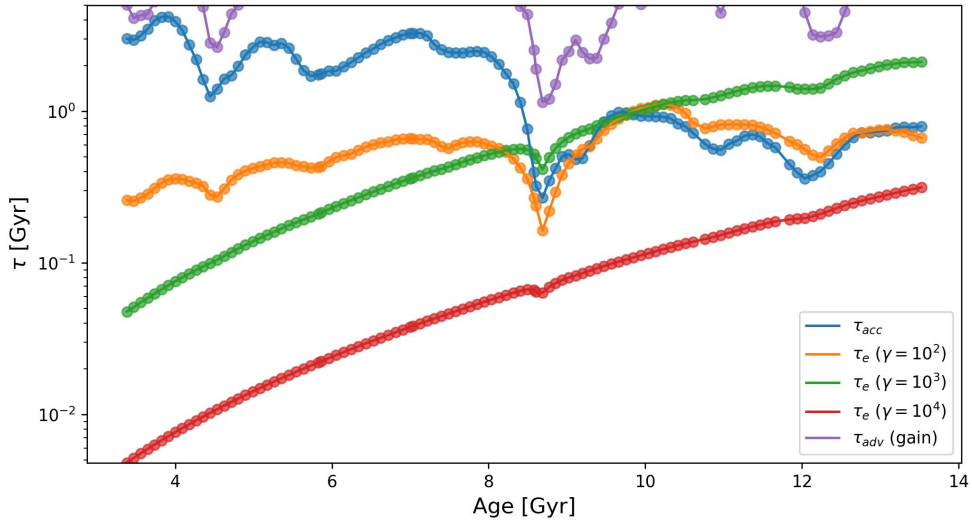

Figure 3.12: Time evolution of median timescales for the tracers found within less than 0.30 Mpc from the center of the cluster in the last frame.

re-acceleration of electrons. It is also important to remember that the vast majority of the tracers enter the cluster after 10 Gyr, and hence the median timescale for re-acceleration drops very quickly.

Figure 3.13 shows the median value of the Lorentz factor for electrons injected at different epochs with $\gamma_{\rm inj} = 1000$. Even if the electrons are all injected with the same energy, depending on their early evolution their final median energy can differ significantly, i.e. by a factor ~ 2. On one hand, the re-acceleration effects induced by the latest mergers are in all cases increasing the median energy of the population. However, the time that the CRe spend in low vorticity regions affect the initial energy they can reach before the latest re-acceleration stage begins. Therefore, relativistic electrons injected at earlier stages, prior to cluster formation, will lose more energy than those injected during later phases, which may gain energy through the accretion of cluster satellites. In anycase, it is important to notice that even in the case of very early injections and more severel losses, our simulated electron population can basically keep the same median energy for more than 7 Gyrs, which is not expected in a simple scenario in which electrons are just subject to cooling and collisional losses in the absence of major mergers.

The cumulative distribution of the CRe energy, which takes into account every gas cell, provides a valuable analysis tool (Figure 3.14). The acceleration processes, for example, are highlighted by a decrease in the exponential factor of the cumulative function, while losses increase the exponential. This increase in the exponential factor (the exponential factor is negative following Equation 2.9) corresponds to a decrease in the maximum energy of high-energy particles, shifting the curve towards lower values. The cumulative distribution is related to the gas dynamical history, therefore, it is important to note that a significant portion of the electrons being considered is distributed within satellites in the earlier epochs. These satellites begin to cluster into major structures until approximately 12 Gyr, when the cluster recorded its last merger. This is also reflected in the time evolution of the distribution, which moves towards higher energy values with age until

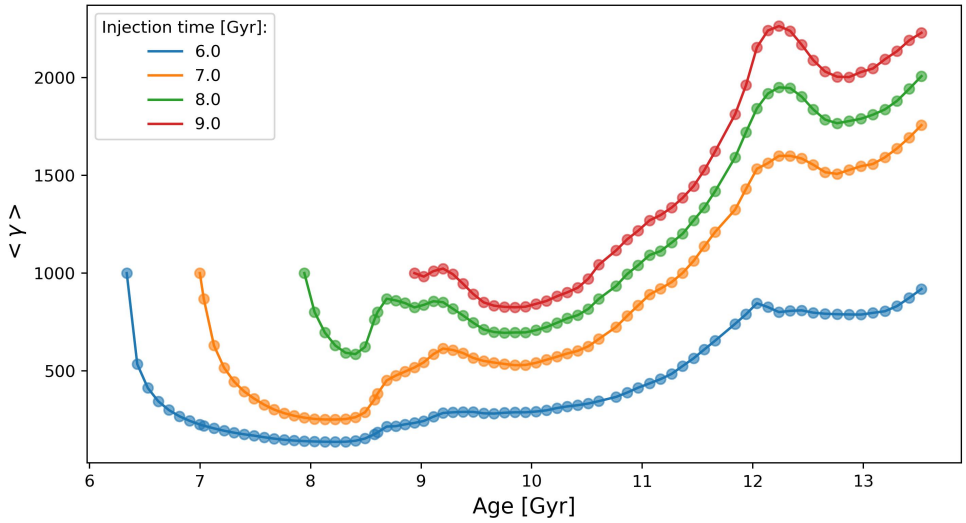

Figure 3.13: Time evolution of median Lorentz factor for the tracers found within the RH in the last frame of the simulation. The electrons were injected at different ages but all with initial $\gamma = 1000$.

the mergers stop and the CRe cool down.
Examining Figure 3.14, the first distribution at 9.6 Gyr exhibits a very low number of CRe at high energy, attributed to a low number of re-accelerated particles and radiative losses. Furthermore, the increase in vorticity at ~ 9 Gyr only involves a few of the tracers that will eventually form the final RH. The increase in the number of electrons at high energy observed from 9.6 to 11.1 Gyr is due to a mixing of tracers that were scattered after the mergers and experienced a strong decrease in density and magnetic field, while vorticity shows a slow increase. The tail of the curve at 11.1 Gyr displays a different behaviour at high energy, attributed to Fermi II processes, as minor satellites in the cluster contribute to turbulence. The re-accelerated particles often originate from the satellites, while the ones already present in the cluster are re-energised by very strong turbulence in the center. This is consistent with the advancement of the "knee" of the distribution. This knee, in this context, represents the location where a sharp drop in the distribution can be seen, and it roughly indicates where the bulk of the electron distribution is.

At approximately 11.6 Gyr, a fraction of the tracers present in a satellite that is falling onto the cluster begins to mix with the cluster gas, which is already turbulent due to the previous merger. This results in the re-acceleration of CRe, both from the cluster and the infalling satellite. As before, the particles experience a significant increase in density, vorticity, and magnetic field. The turbulence generated from the merger re-accelerates a large fraction of electrons, including those from the satellites and the cluster itself, which initially were found at lower energy. This increase in particle fraction is visible in the tail of the distribution. At age 12.4 Gyr, after the satellite merged with the cluster, a small percentage of CRe are found at very high energy. At $\gamma > 10^4$ the power law exponent decreases due to synchrotron and IC losses, which are more efficient than the re-acceleration processes. The last distribution represent the system after the final merger, where the tracers are located in the innermost part of the cluster, where the RH

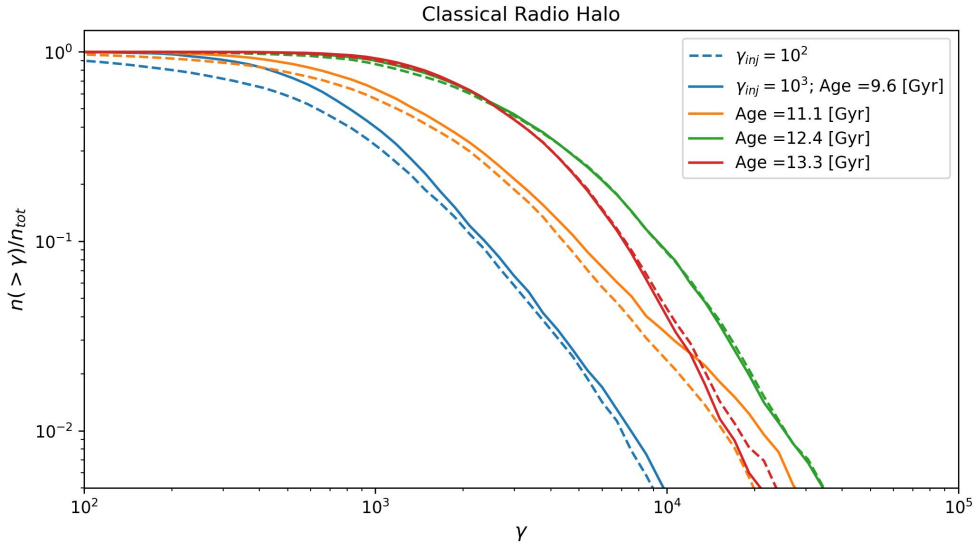

Figure 3.14: RH cumulative distributions of CRe as function of Lorentz factor γ. The values are normalised with respect the total number of points that give us the total fraction of CRe with energy higher than the selected value. The electrons used in those distributions are injected at $\gamma = 10^2$ (dashed lines), and $\gamma = 10^3$ (solid lines). The values are normalised with respect the total number of points that give us the total fraction of CRe with energy higher than the selected value. Five different ages are shown.

are observed. Despite the steep curve, $\sim 20\%$ of the electrons are found at energy higher than $\gamma > 5000$, and can produce synchrotron emission. We can see the last two curves as the evolution of the inner part of the cluster, since at 12.4 Gyr the vast majority of the tracers already occupy the region within half of the virial radius (Figure 3.15). The differences between the last two curves are mostly due to the radiative processes since the vorticity decreases faster than the magnetic field and the density that instead remains steady in the last phases. The RH region is then expected to emit the most energetic part of the radiation during the last two Gyr. The turbulence plays a critical role through this phases, sustaining the energy of the CRe.

3.7.3 Tracers filling the mega halo region

In this paragraph I analyse the Lagrangian history of the tracers that in the last frame are found between $0.30 < r < 0.76$ Mpc, with respect to the center of the cluster, which represents my best guess of a typical MH region. Their evolution is very similar to the one studied earlier. The tracers are initially arranged in filaments which, after a series of mergers, form the main cluster at ~ 8 Gyr. Even after $\sim$10 Gyr, a significant portion of the tracers remain in satellites, similar to those that will occupy the central region. The cluster increases its mass through accretion of satellites, which results in the scatter of a large portion of the particles that were already present in the central region. Finally, the merger at ~ 11 Gyr causes a large portion of the tracers, contained in the satellites, to be dispersed into the outer regions at high velocities and to increase the turbulence of the medium.

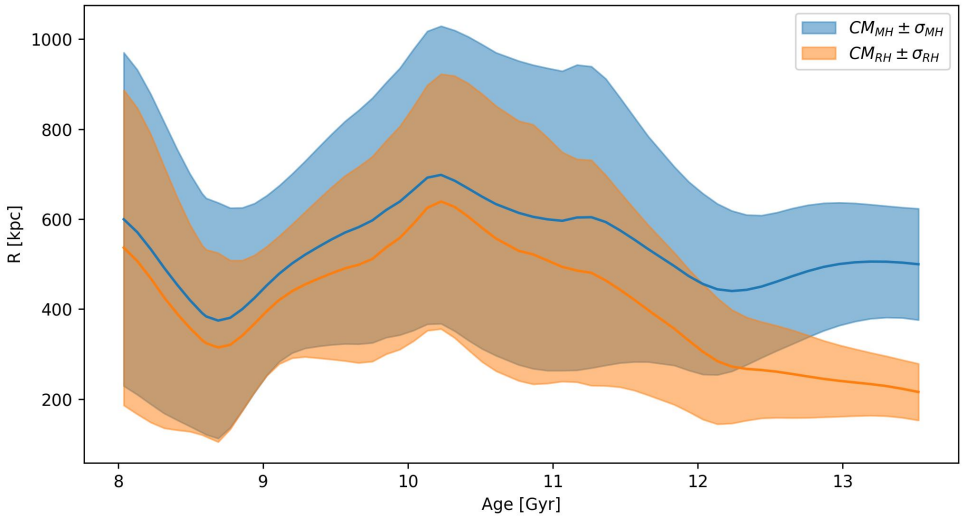

Figure 3.15: Spatial position of the center of mass of the two families of tracers with respect the center of mass of the cluster. The shadow regions represent the tracers dispertion.

In this section, I will mainly focus on the evolution after ~ 8 Gyr, which is the initial phase of cluster formation. The field evolution closely resembles that of classical MHs, due to similar locations that the two families of tracers share during their evolution. However, as reported earlier, the major differences appear only during the final stages of the evolution, were the vorticity recorded by MH tracers decreases faster, with respect to the central region. Similar behaviour can be observed in the density and the magnetic field profiles. This discrepancies arises from the fact that the vast majority of those tracers are found in the center before being dispersed. Moreover, the particles that are accreted from the satellites share the same evolution. It is expected that the electrons will be efficiently re-accelerated after the cluster formation, and we can also expect lower Coulomb losses due to the slightly lower density. Fermi II processes remain very efficient in this region, and the combination of these factors creates a condition that is suitable for the formation of a reservoir of high energy electrons in the MH region.

As Figure 3.17 shows, at ~ 8 Gyr the re-acceleration timescale is low enough to allow high energy electrons to reach $\gamma \sim 10^3$. Additionally, it can be observed that during the final stages, the timescales are longer than the central region. Fermi II processes due to the strong turbulent component remain efficient, as previously mentioned. The accretion of a certain number of tracers, with the merger at ~ 12 Gyr, determines the increase in the vorticity content and in density. This implies a significant re-acceleration, but on the other hand, it determines a fast energy loss of the particles at very low energy. The advection timescale is always higher than the other timescales, so I assume that this effect can be neglected.

As in the case of RH, even if CRe are injected at different epochs, their final energy is very similar, owing to the fact that most of the re-acceleration happens in the last 2 Gyr. Only electrons injected before 7 Gyr behave differently, due to significant losses by low energy CRe, which thermalise with the medium. In fact, those electrons are found

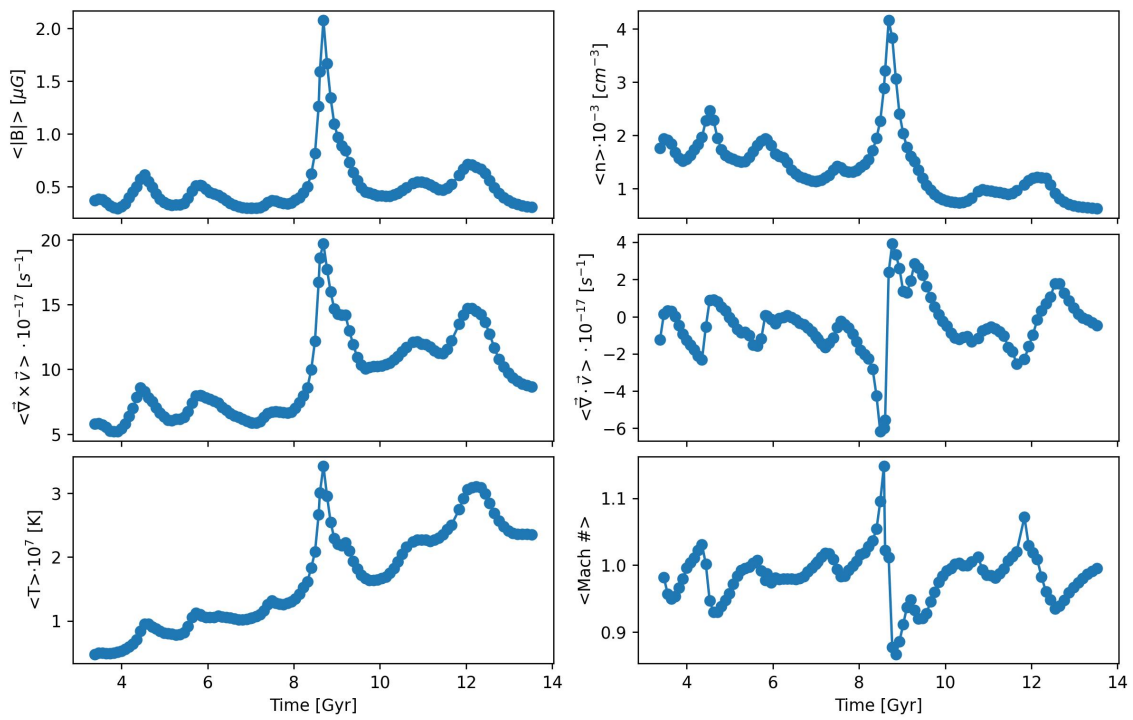

Figure 3.16: Time evolution of the median values of the fields for MH tracers.

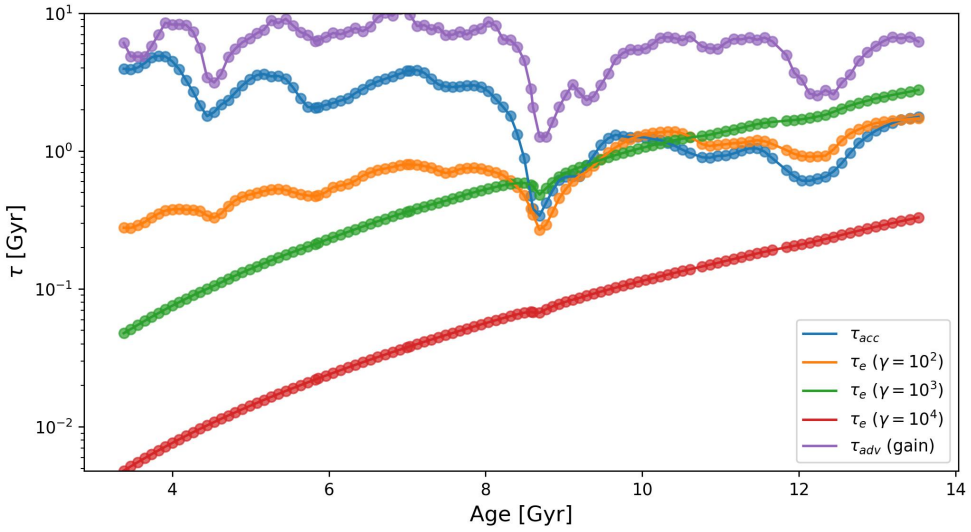

Figure 3.17: Time evolution of median timescales for the tracers found between 0.30 and 0.76 Mpc from the center of the cluster in the last frame, this is the MH region.

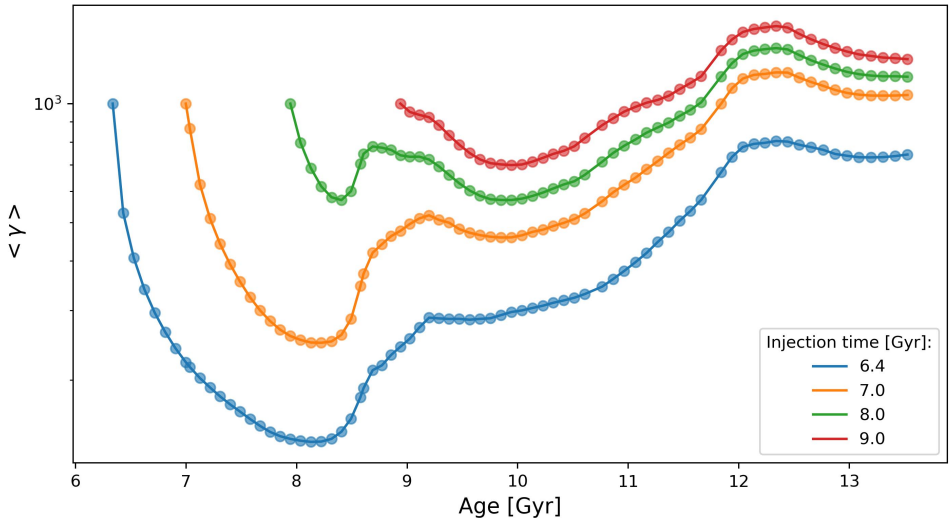

Figure 3.18: Time evolution of median Lorentz factor for the tracers found within the MH in the last frame of the simulation. The electrons were injected at different ages but all with initial $\gamma = 1000$.

in satellites that do not experience many gravitational interactions until they merge with the cluster. CRe present in these regions undergo substantial energy loss before being re-accelerated by Fermi II processes induced by mergers. For these reasons, CRe will be considered to have been injected at 8 Gyr.

The cumulative distribution for MH CRe shows steeper distributions at high energies, as evidenced by the knee of the distribution located at lower values of γ. At 9 Gyr, the fraction of high energy CRe is low and most part of the CRe has not been re-accelerated yet. This is attributed to a large fraction of the electrons distributed in the satellites that have not merged yet. Their entry into the cluster increases vorticity and promotes Fermi II processes, resulting in a 3% increase in the electron fraction at energies higher than 5000 in a span of 1.5 Gyr. At 11.1 Gyr, the slope of the distribution remains unchanged, but the distribution shifts towards higher energies due to the accretion of small satellites. By 11.6 Gyr the behaviour of the CRe changes, the re-acceleration timescale decreases, while the number of high energy electrons increases, indicating highly efficient Fermi II process. This period precedes the merger of the last satellite at 12 Gyr, during which a part of the tracers has already experienced an increase in vorticity as they are widely distributed. This final merger generates turbulence, which reaches its maximum at 12.3 Gyr, when the fraction of electrons with $\gamma > 5000$ doubles its value in a time of less 1 Gyr passing from $\sim 7\%$ to 15%. The whole process leads to an increase of the tail distribution at very high energy, that in time evolves making the distribution knee increasing with time. The curve steepness at 12.4 Gyr, and it spreads across a wider energy range compared to the case of RH. In this period the prevailing loss time-scale is the radiative one, as can be seen in Figure 3.17, the shape of the curve also shows the dominance of the IC process, highlighted by the $(1+z)^4$ behaviour. Thermal processes are very efficient for $\gamma \leq 100$, whereas radiative processes prevail at the higher end of the spectrum. Finally, after a quiescence phase where some tracers slowly fall back toward the classical RH, no further

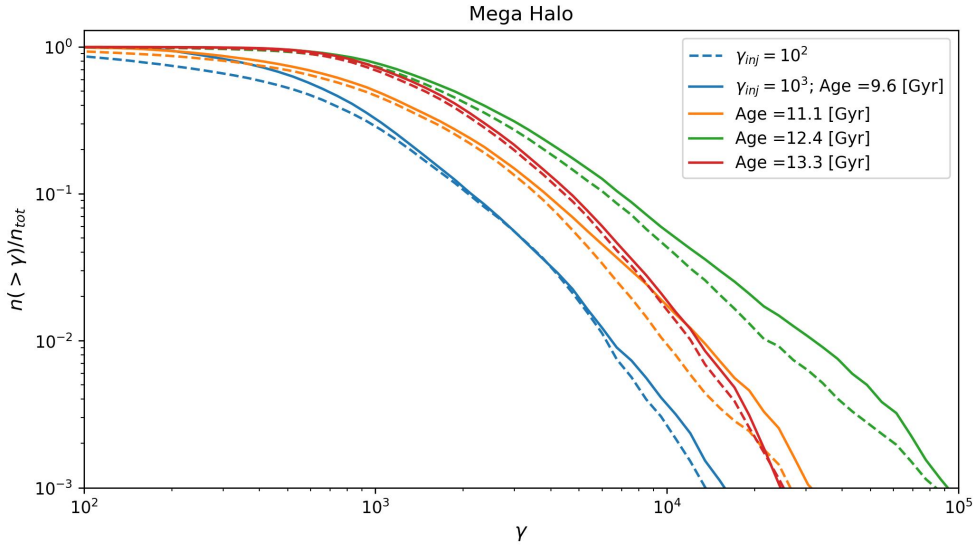

Figure 3.19: MH cumulative distributions of CRe as function of Lorentz factor γ. The values are normalised with respect the total number of CRe that give us the total fraction of CRe with energy higher than the selected value. Five different ages are shown. The electrons used in those distributions are injected at $\gamma = 10^2$ (dashed lines) and $\gamma = 10^3$ (solid lines).

re-acceleration process is active at 13.3 Gyr, resulting in the disappearance of the highly energetic part of the distribution. The fraction of tracers with $\gamma > 5000$ is only $\sim 5\%$, a third of the fraction at 12.4 Gyr.

3.7.4 Comparison between the classical and mega radio halo

MH and CRH tracers share for a long part of their life the same region of space and they separate only in the final phases (Figure 3.20). Although their distributions may appear similar, but the conditions in the innermost part of the cluster are significantly different from the neighborhood region, which explains the differences observed in time evolution of the fields recorded by tracers shown before. Figure 3.21 shows a strong deviation of vorticity, a gap of $\Delta\omega \sim 4 \cdot 10^{-17} \mathrm{s}^{-1}$, whereas the other fields do not vary of more than a unit.
The evolution phases are quite similar, with the CRe experiencing the same merger events. A large portion of the MH tracers pass through the center of the cluster before settling in the external halo.

By taking advantage of Equation 3.25, we can obtain the cumulative distribution of the steepening frequency of the CRe. The cumulative distribution of ν_s of the MH region is shown in Figure 3.22. The fraction of detectable electrons, within the LOFAR frequencies, range, varies between 24 and 79% in the lower part of the bandwidth, while it ranges from 13% to 60% in the upper part, for the considered epochs. This indicates that a substantial number of electrons could potentially be detected, as we can expect for mega RHs. The gap between the distributions at different γ_{inj} tends to decrease with time, as a combined effect of the re-acceleration and the radiative losses, described earlier. In fact, an upper

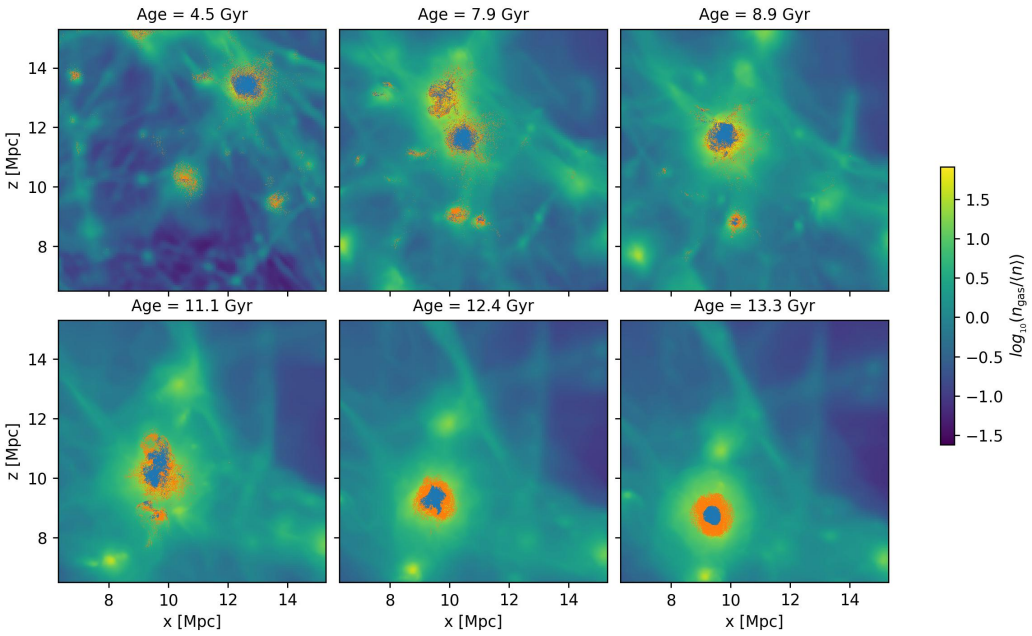

Figure 3.20: Position of the MH and RH tracers in the cluster at approximately the epochs of the main mergers. The blue tracers are in blue, while MH tracers are in orange. The cell resolution is 18 kpc. The length along the x axis is 7.38 Mpc while is 6.48 Mpc in z direction.

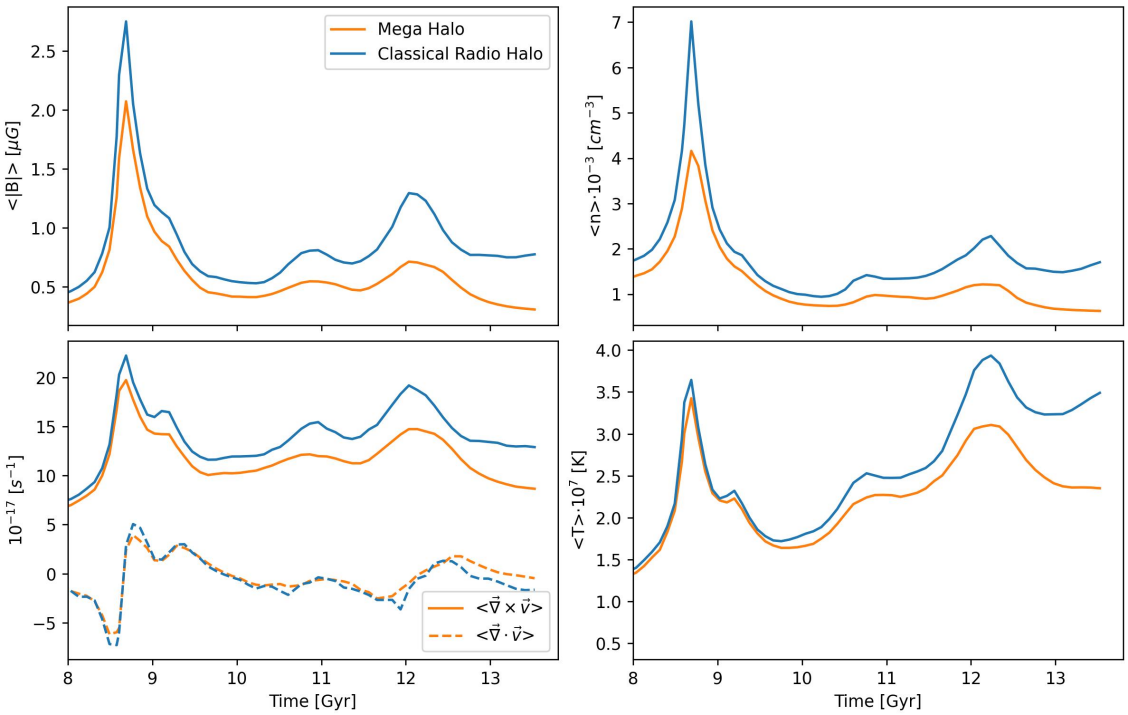

Figure 3.21: Comparison between MH and RH mean fields vs. time. Those plots highlight the small differences in physical condition recorded by the tracers.

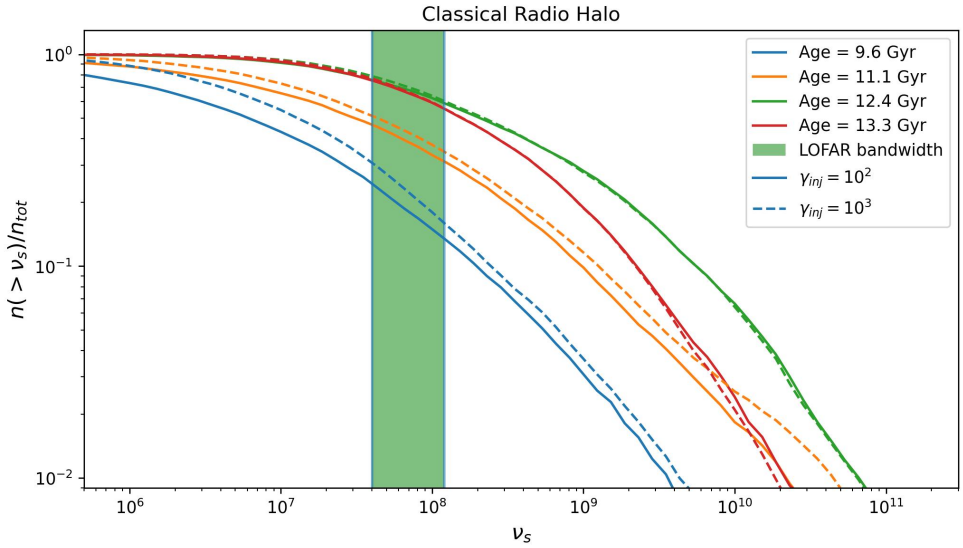

Figure 3.22: RH ν_s cumulative distributions of CRe. The values are normalised with respect to the total number of points, which gives us the total fraction of CRe with a frequency higher than the selected value. Four different ages and with two different $\gamma_{\rm inj}$ per epoch are shown.

limit for the energy is observed plotted against the curl of the velocity (Figure 3.23). This effect is due to electrons re-acceleration that increases the CRe energy to $\gamma \sim 10^5$. At this energy, radiative losses become significant and their timescales fall below a few Myr, imposing a maximum energy reachable for the electrons. When a substantial number of electrons undergo re-accelerated due to a merger, if the increase of energy is higher than the energy that the electron can lose via radiative processes, the initial amount of energy is not relevant anymore. The maximum γ is determined only by the synchrotron or the IC losses. It is evident that, after the merger phases, the information of the initial $\gamma_{\rm inj}$ is lost. This is important, as it demonstrates that the predictions for MH in this region are fairly independent of the specific assumptions for the initial value of $\gamma_{\rm inj}$. Regarding the frequencies analysis, the CRe reach their maximum energy during the last merger showing, as expected, the critical role played by the Fermi II mechanism. The fraction of electrons with high energy remains substantial in the last Gyr.

The cumulative distributions of $\nu_{\rm s}$ for MH electrons (Figure 3.24) show that for frequencies $\nu_{\rm s} > 40$ MHz (detectable by LOFAR), the differences between different $\gamma_{\rm inj}$ are negligible at each time, i.e. the variations are always less than $\sim 4\%$ and the deviation are stronger for very high frequencies. The fraction of CRe within the LOFAR bandwidth ranges between 20 and 57%, in the lower energy part of the band, while in the upper part, the fraction varies between 11 and 40%. On the other hand, if we are considering the break frequency $\nu_{\rm b}$, the portion of electrons varies from 13% to 28% in the lower frequency range and from 6% to 23% in the upper range. This fraction should correspond to the point of the radio spectrum where the emitting frequency reaches its maximum. While this does not represent the actual spectrum, this approach can still provide an idea of the detectability of the emission from our CRe. In this case as well, we observe that the last merger increases the total energy of the CRe. However, this time the energy loss

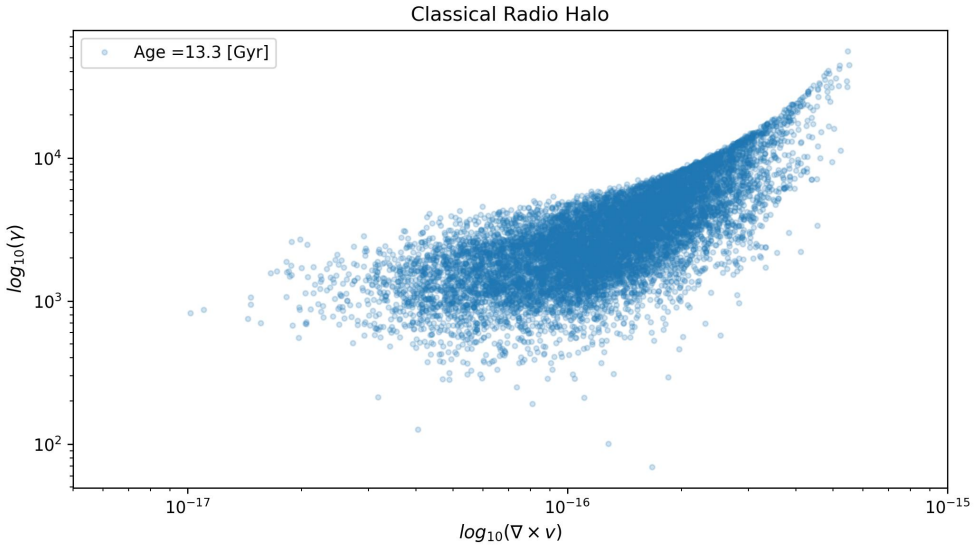

Figure 3.23: CRH distribution of electrons in the γ vorticity plane. It is visible the upper limit that the energy can reach for a given value of vorticity.

is stronger, meaning that the radiative processes are more effective also at lower energy, and that the re-acceleration less efficient in the outer region. Nevertheless, it is still able to produce a relevant amount of high energy electrons in the outskirt. As displayed in Figure **??**, the knee of the distribution is still located at the same frequency in the two final epochs, but its drop is stronger than in the RH. It can be seen that the information of $\gamma_{\rm inj}$ is lost after the merger, meaning a weaker re-acceleration and a dominance of radiative losses.

The percentage of electrons with $\nu_{\rm s}$ larger than the upper limit of the LOFAR band is shown in Figure 3.25. In the initial phases after the cluster formation, the number of high energy CRe observed is very low, also in the inner part of the cluster. In the subsequent epoch, the tracers are distributed through the volume, and only those in the center experience strong vorticity. The peripheral region, as reported earlier, is crowded with tracers that are falling back toward the center, after being dispersed by the first mergers. The electrons thus experience an increase of turbulence resulting from the merger shock, which raises the energy content of the electrons. At 12.4 Gyr, immediately after the merger, the turbulence re-accelerates the CRe that now reach the maximum emissivity, or making a larger portion of them radio visible. The fraction varies from 11 and 48% respectively at $0.4R_{500}$ and R_{500}. In the very center, particles reach the highest content of energy, 95% of them emitting at energies higher than the LOFAR band. The behaviour changes in the last Gyr, where the very center shows a strong decrease while the rest of the cluster follows a radial behaviour similar to that observed by Cuciti et al. (2022). This suggests that a non negligible fraction of electrons, after being re-accelerated from turbulence, can produce the diffuse radiation that extends over the RH region, exhibiting a similar profile to the one detected by LOFAR.

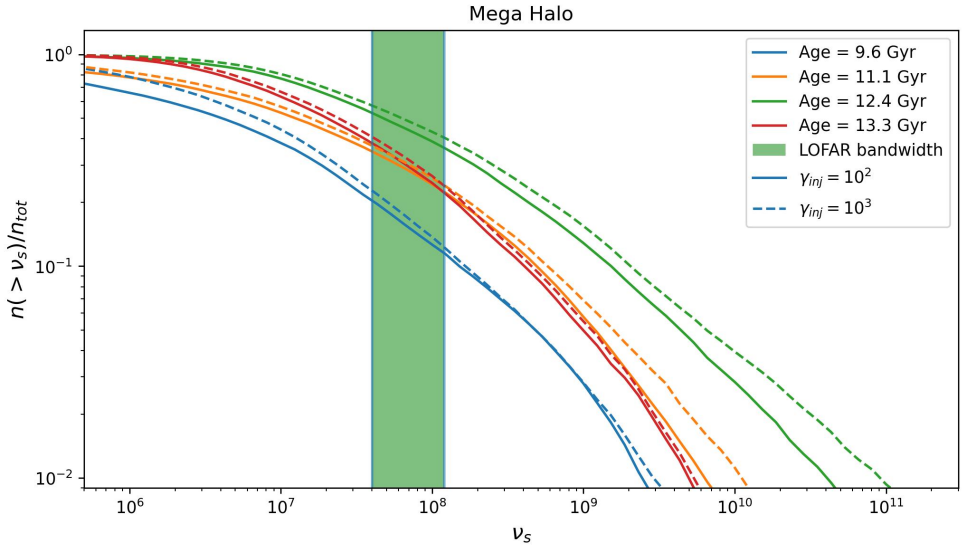

Figure 3.24: MH ν_s cumulative distributions of CRe. The values are normalised with respect to the total number of points that give us the total fraction of CRe with a frequency higher than the selected value. The values of $\gamma_{\rm inj}$ and time are the same of Figure 3.22.

3.8 Discussion

The main motivation of my thesis work is the recent observational discovery of MH in clusters of galaxies (Cuciti et al., 2022), whose origin is unknown.
We produced a new cosmological simulation of the evolution of cluster of galaxies to test if the turbulence generated in its outskirts is able to maintain energetic enough ($\sim$ GeV) electrons in a fraction of the volume. We simulated the formation of one cluster of galaxies with the cosmological code *ENZO* and used Lagrangian tracer particles to follow the energy evolution of families of electrons under the effect of radiative and Coulomb losses, adiabatic changes, and under the effect of turbulent re-acceleration in the "adiabatic stochastic acceleration" scenario (Brunetti & Lazarian, 2016b).
With this methodology, I show for the first time that formation of MHs, despite their unprecedent size, can be understood within the framework of the turbulent re-acceleration model already used to interpret the RH phenomenology (e.g. Brunetti & Jones, 2014): regardless of the initial energy of cosmic ray electrons, the integrated effect of turbulent re-acceleration by cluster-wide turbulent motions is enough to always make a large portion (up to $\sim$ 57 %) of electrons in the MH region radio emitting at and above LOFAR frequencies (50-140 MHz).
The Lagrangian analysis of the MH region suggests a few crucial and underlooked aspects of electron acceleration in these peripheral regions. First, our tracer analysis allowed us to show that most of the matter found in the MH comes from the disruption and mixing of gas matter initially located in clumps, which has been accreted some Gyr before the final merger by the main cluster, and it does not instead come from smooth gas accretions (Figure 3.20).
Connected to this, the dynamical histories of the particles in the CRH or in the MH are very similar, except in the last 1 Gyr after the latest major merger (Figure 3.21). Thus,

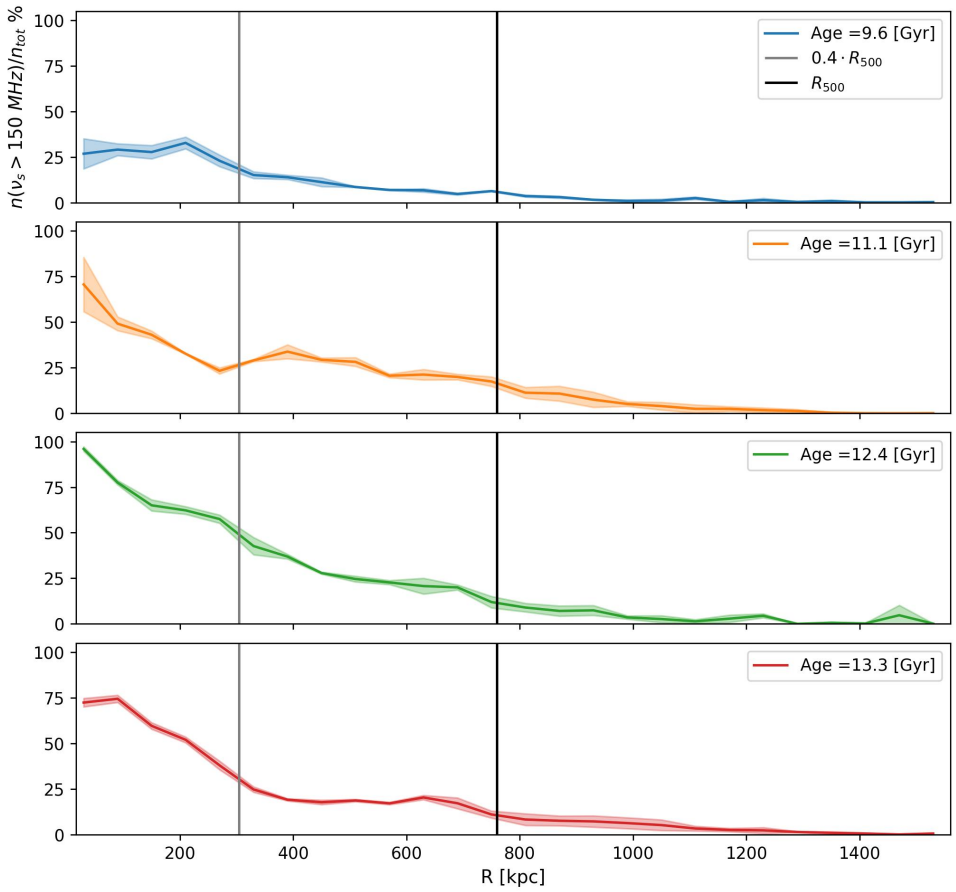

Figure 3.25: Percentages of electrons with ν_s higher than the LOFAR higher band. The curves represent the average value computed out of different $\gamma_{inj} = [10^2, 3{\cdot}10^2, 5{\cdot}10^2, 10^3, 3{\cdot}10^3, 5 \cdot 10^3]$ for CRe injected at 8 Gyrs. The values are represented with their standard deviations.

a large fraction of the baryons has already crossed the innermost cluster regions at least once, and the relativistic electrons in the MH have been processed at least once by the merger.
Finally, these results call for a substantial update of the theoretical picture of the lifetime of relativistic electrons in the ICM. In fact, such complex turbulent dynamics generates multiple episodes of re-acceleration, which overall make the effective lifetime of electrons longer than previously thought (Figures 3.17). This implies that the pool of "fossil" electrons in the ICM may be significantly more energetic than what expected so far.
In this work, we did not simulate in detail the possible injection process of the relativistic electrons later used for the production of radio emission, as in other works (e.g. Vazza et al., 2021, 2023). However, the fact that the bulk of the gas content of MH comes from the accretion of already formed halos at $z = 2$, as shown by my analysis, makes it

extremely likely that each of these halos has a significant content of relativistic electrons, following from the activity of star formation and active galactic nuclei, which are both peaking around this epoch. In this sense, our initial energy of $\gamma_{\rm inj} = 10^2$ has to be regarded as a very conservative limit of the actual energy of the relativistic electrons carried by the accreted halos.

Chapter 4

Summary and conclusions

In this thesis, I have explored the mechanisms which may be responsible for the production of the newly discovered class of MHs, reported by the recent work by Cuciti et al. (2022).
I have analysed the general properties of galaxy clusters and their main features at all the wavelengths (from X-ray properties to the synchrotron radio emission) from the inner to outer regions. I have also reviewed all possible mechanisms of acceleration and re-acceleration from the Fermi model, as well as all radiative processes affecting the energy of cosmic rays in the ICM.
Then, I have introduced the analysis of the cosmological MHD simulation produced with *ENZO* (Bryan et al., 2014), specifically for this project, supplemented with a Lagrangian tracer particles (Wittor et al., 2016) to follow the gas advection during its evolution. This allowed me to follow the evolution of CRe under the effect of radiative and Coulomb losses, adiabatic compression or expansion, and turbulent re-acceleration by turbulent motions, as modeled in the adiabatic stochastic acceleration scenario from Brunetti & Lazarian (2016a). I have presented the analysis of the evolution of single tracers, to sample the typical evolution of the gas that ends up in the central region of the main cluster. This analysis shows that turbulence is able to keep relativistic electrons accelerated to high energy, also highlighting the correlation with the merger events that enhance the vorticity of the gas in the ICM.
Then, I have focused on the evolution of the full population of CRe advected with all large scale accretions that eventually formed the total mass of the cluster. In particular, I have studied in parallel the evolution of the CRe found in the typical region forming the RH (i.e. within $0.4R_{500}$), and of those who fill the region of the MH (i.e. within a radius from $0.4R_{500}$ to R_{500}). I have computed the spectral evolution of relativistic electrons with different initial energies, in order to have a wider picture of their possible energy evolution and then I evaluated the synchrotron emission frequency, following Cassano et al. (2010), to estimate the fraction of CRe capable of emitting in LOFAR radio frequency ($50 - 140$ MHz). The most important result of this thesis, is that I found that, regardless of the initial energy of CRe, the integrated effect of turbulent re-acceleration by cluster-wide turbulent motions is enough to always make a large portion (up to ~ 57 %) of the cluster outer regions emitting at LOFAR frequencies, and therefore produce MHs. The Lagrangian analysis of the MH region suggests a few crucial and underlooked aspects of electron acceleration in these peripheral regions. First, our tracer analysis has allowed us to show that most of the matter found in the MH comes from the disruption and mixing

of gas matter initially located in clumps, which has been accreted a few billions of years before the final merger by the main cluster. This material is not coming from smooth gas accretions, and it is not being re-accelerated by ICM turbulence for the first time (unlike what was originally proposed by the scenario outlined in the discovery paper by Cuciti et al. 2022). Moreover, the dynamical evolution of the tracers ending up in the radio and MH regions are overall very similar, as they also share a large part of their evolution in the same region of the space, and undergo through the same merger events. Only in the last Gyr of evolution their dynamical history gets different, as they are spatially advected in distinct radial sections of the cluster.
These results call for a substantial update of the theoretical picture of the lifetime of relativistic electrons in the ICM. In fact, such complex turbulent dynamics generates multiple episodes of re-acceleration, which overall make the effective lifetime of electrons longer than previously thought. This implies that the pool of "fossil" electrons in the ICM may be significantly more energetic than what expected so far. The above results have been included in a paper I have submitted to Astronomy & Astrophysics Letters (Beduzzi et al., 2023, arXiv:2306.03764) and it is likely the first of a series of numerical and theoretical works in which we are going to extend the first key results of my thesis, and simulate the energy evolution of radio emitting electrons with more detail, and for a larger number of simulated clusters of galaxies, to match the variety of existing and incoming radio observations of this new and spectacular class of objects.

Bibliography

Abell G. O., 1958, ApJS, 3, 211

Abell G. O., Corwin H. G. J., Olowin R. P., 1989, ApJS, 70, 1

Ade P. A. R., et al., 2016, ApJ, 594, A27

Allen S. W., Evrard A. E., Mantz A. B., 2011, ARA&A, 49, 409

Ballarati B., Feretti L., Ficarra A., Giovannini G., Nanni M., Olori M. C., Gavazzi G., 1981, A&A, 100, 323

Beduzzi L., Vazza F., Brunetti G., Cuciti V., Wittor D., Corsini E. M., 2023, A&A, submitted (`arXiv:2306.03764`)

Bennett C. L., et al., 1996, A&A, 464, L1

Beresnyak A., 2012, MNRAS, 108, 035002

Beresnyak A., Miniati F., 2016, ApJ, 817, 127

Bethe H., Heitler W., 1934, Proc. R. Soc. London. Series A, 146, 83

Blasi P., Colafrancesco S., 1999, Astrop. Phys., 12, 169

Blasi P., Gabici S., Brunetti G., 2007, Int. J. Mod. Phys. A, 22, 681

Bonafede A., Intema H. T., Brüggen M., Girardi M., Nonino M., Kantharia N., van Weeren R. J., Röttgering H. J. A., 2014, ApJ, 785, 1

Bonafede A., et al., 2021, ApJ, 907, 32

Borgani S., Kravtsov A., 2011, Ad. Sci. Let., 4, 204

Botteon A., et al., 2022, Sci. Ad., 8, 7623

Braginskii S. I., 1965, Rev. P. Phys., 1, 205

Brunetti G., Jones T. W., 2014, Int. J. Mod. Phys. D, 23, 1430007

Brunetti G., Lazarian A., 2007, MNRAS, 378, 245

Brunetti G., Lazarian A., 2016a, MNRAS, 458, 2584

Brunetti G., Lazarian A., 2016b, MNRAS, 458, 2584

Brunetti G., Vazza F., 2020, Phys. Rev. Let., 124, 051101

Brunetti G., et al., 2008, Nature, 455, 944

Bryan G. L., et al., 2014, ApJS, 211, 19

Carlstrom J. E., Holder G. P., Reese E. D., 2002, ARA&A, 40, 643

Cassano R., Brunetti G., Röttgering H. J. A., Brüggen M., 2010, ApJ, 509, A68

Cavaliere A. G., Gursky H., Tucker W. H., 1971, Nature, 231, 437

Chandran B. D. G., 2000, Phys. Rev. Let., 85, 4656

Chernyshov D. O., Dogiel V. A., Ko C. M., 2012, ApJ, 759, 113

Cho J., Lazarian A., 2003, MNRAS, 345, 325

Cuciti V., Brunetti G., van Weeren R., Bonafede A., Dallacasa D., Cassano R., Venturi T., Kale R., 2018, ApJ, 609, A61

Cuciti V., et al., 2021, ApJ, 647, A50

Cuciti V., et al., 2022, Nature, 609, 911

Di Gennaro G., et al., 2018, ApJ, 865, 24

Domínguez-Fernández P., Vazza F., Brüggen M., Brunetti G., 2019, MNRAS, 486, 623

Donnert J., Vazza F., Brüggen M., ZuHone J., 2018, Space Sci. Rev., 214, 122

Eddington A. S., 1919, Observatory, 42, 119

Fahlman G., Kaiser N., Squires G., Woods D., 1994, ApJ, 437, 56

Felten J. E., Gould R. J., Stein W. A., Woolf N. J., 1966, ApJ, 146, 955

Fermi E., 1949, Phys. Rev., 75, 1169

Forman W., Kellogg E., Gursky H., Tananbaum H., Giacconi R., 1972, ApJ, 178, 309

Ginzburg V., Syrovatskii S., 1964, Sov. Astr., 8, 342

Giovannini G., Feretti L., 2000, New Ast., 5, 335

Goldreich P., Sridhar S., 1995, ApJ, 438, 763

Gott J. Richard I., Gunn J. E., 1971, A&A, 169, L13

Gott J. R. I., Rees M. J., 1975, A&A, 45, 365

Hockney R. W., Eastwood J. W., 1988, Computer Simulation using Particles. CRC Press, Boca Raton

Hoshino M., 2001, Prog. Theor. Phys. Sup., 143, 149

Hudson D. S., Mittal R., Reiprich T. H., Nulsen P. E. J., Andernach H., Sarazin C. L., 2010, A&A, 513, A37

Jaffe W. J., Rudnick L., 1979, ApJ, 233, 453

Kaiser N., Squires G., 1993, ApJ, 404, 441

Kaiser N., Squires G., Broadhurst T., 1995, ApJ, 449, 460

Kellogg E., Gursky H., Tananbaum H., Giacconi R., Pounds K., 1972, A&A, 174, L65

Kneib J.-P., Natarajan P., 2011, A&AR, 19, 47

Koch H., Motz J., 1959, Rev. Mod. Phys., 31, 920

Kolmogorov A., 1941, Akademiia Nauk, 30, 301

Kravtsov A. V., Borgani S., 2012, ARA&A, 50, 353

Large M. I., Mathewson D. S., Haslam C. G. T., 1959, Nature, 183, 1663

Lazarian A., 2006, A&A, 645, L25

Leccardi A., Molendi S., 2008, A&A, 486, 359

Lotz J. M., et al., 2017, ApJ, 837, 97

McNamara B. R., O'Connell R. W., 1989, AJ, 98, 2018

Medezinski E., Umetsu K., Okabe N., Nonino M., Molnar S., Massey R., Dupke R., Merten J., 2016, ApJ, 817, 24

Meekins J. F., Fritz G., Chubb T. A., Friedman H., 1971, Nature, 231, 107

Melrose D. B., 1980, Plasma Astrophysics. Gordon and Breach, New York

Merten J., et al., 2011, MNRAS, 417, 333

Molendi S., Pizzolato F., 2001, ApJ, 560, 194

O'Connell R. W., McNamara B. R., 1989, AJ, 98, 180

Ohno H., Takizawa M., Shibata S., 2002, ApJ, 577, 658

Onsager L., 1949, Nuovo Cimento, 6, 279

Pearce C. J. J., et al., 2017, ApJ, 845, 81

Peebles P. J. E., 1970, AJ, 75, 13

Pistinner S., Levinson A., Eichler D., 1996, ApJ, 467, 162

Planck Collaboration et al., 2011, A&A, 536, A1

Pratt G. W., Böhringer H., Croston J. H., Arnaud M., Borgani S., Finoguenov A., Temple R. F., 2007, A&A, 461, 71

Pratt G. W., Croston J. H., Arnaud M., Böhringer H., 2009, A&A, 498, 361

Press W. H., Schechter P., 1974, ApJ, 187, 425

Richardson L. F., 1922, Weather Prediction by Numerical Process. Cambridge University Press, Cambridge

Ryu D., Kang H., Hallman E., Jones T., 2003, ApJ, 593, 599

Sarazin C. L., 1999, ApJ, 520, 529

Schlickeiser R., 2002, Cosmic Ray Astrophysics. Springer Berlin, Heidelberg

Schneider P., Ehlers J., Falco E. E., 1992, Gravitational Lenses. Springer Berlin, Heidelberg

Shimwell T. W., et al., 2019, ApJ, 622, A1

Shimwell T. W., et al., 2022, ApJ, 659, A1

Smith S., 1936, ApJ, 83, 23

Spitzer L., 1956, Physics of Fully Ionized Gases. Interscience Publishers, New York

Sunyaev R. A., Zeldovich Y. B., 1970, Ap&SS, 7, 3

Sunyaev R. A., Zeldovich Y. B., 1972a, Com. Astrop. Sp. Phys., 4, 173

Sunyaev R. A., Zeldovich Y. B., 1972b, A&A, 20, 189

Sunyaev R. A., Zeldovich Y. B., 1980, MNRAS, 190, 413

V. K. A., Vikhlinin A., Nagai D., 2006, ApJ, 650, 128

Vazza F., Brunetti G., Kritsuk A., Wagner R., Gheller C., Norman M., 2009, ApJ, 504, 33

Vazza F., Brüggen M., van Weeren R., Bonafede A., Dolag K., Brunetti G., 2012, MNRAS, 421, 1868

Vazza F., Brunetti G., Brüggen M., Bonafede A., 2017, MNRAS, 474, 1672

Vazza F., Wittor, D. Brunetti, G. Brüggen, M. 2021, ApJ, 653, A23

Vazza F., Wittor D., Di Federico L., Brüggen M., Brienza M., Brunetti G., Brighenti F., Pasini T., 2023, A&A, 669, A50

Vikhlinin A., Kravtsov A., Forman W., Jones C., Markevitch M., Murray S. S., Van Speybroeck L., 2006, ApJ, 640, 691

Voit G. M., 2005, Rev. Mod. Phys., 77, 207

Wentzel D. G., 1974, ARA&A, 12, 71

Werner N., Durret F., Ohashi T., Schindler S., Wiersma R. P. C., 2008, Space Sci. Rev., 134, 337

Weymann R., 1965, Phys. Fluids, 8, 2112

Weymann R., 1966, ApJ, 145, 560

White S. D. M., 1976, MNRAS, 177, 717

White S. D. M., Rees M. J., 1978, MNRAS, 183, 341

Willson M. A. G., 1970, MNRAS, 151, 1

Wittor D., Vazza F., Brüggen M., 2016, Galaxies, 4, 2075

Yan H., Lazarian A., 2002, Phys. Rev. Let., 89

Yan H., Lazarian A., 2004, ApJ, 614, 757

Yan H., Lazarian A., 2008, ApJ, 673, 942

Yan H., Lazarian A., 2011, ApJ, 731, 35

Zhuravleva I., et al., 2014, Nature, 515, 85

Zwicky F., 1933, Helv. Phys. Acta, 6, 110

van Albada G. B., 1960, Bull. Astr. Inst. Nether., 15, 165

van Albada G. B., 1961, AJ, 66, 590

van Haarlem M. P., et al., 2013, A&A, 556, A2

van Weeren R. J., de Gasperin F., Akamatsu H., Brüggen M., Feretti L., Kang H., Stroe A., Zandanel F., 2019, Space Sci. Rev., 215, 16